HYDRAULIC FRACTURE HEIGHT GROWTH IN LAMINATED SHALE FORMATIONS

A Dissertation

by

JIAWEI LI

Submitted to the Graduate and Professional School of
Texas A&M University
in partial fulfillment of the requirements for the degree of

DOCTOR OF PHILOSOPHY

Chair of Committee,	Kan Wu
Committee Members,	Nobuo Morita
	Eduardo Gildin
	Benchun Duan
Head of Department,	Jeff Spath

August 2022

Major Subject: Petroleum Engineering

ABSTRACT

In unconventional shale formations where the horizontal bedding planes and laminations prevalently exist, the height propagation of a vertical hydraulic fracture is not only affected by the conventional factors such as the treating pressure, in-situ stress, fracture toughness, Young's modulus, Poisson ratio, fracturing fluid density and viscosity, but can also be strongly affected by the horizontal bedding interfaces. Quantifying the hydraulic fracture propagation path and fracture geometries becomes much challenging with the existence of close-spacing bedding interfaces in the laminated formations.

In this work, a comprehensive and non-intrusive hydraulic fracture height growth model is developed considering the combined effect of the formation rock properties and the horizontal weak interfaces. The impact of the rock properties on the fracture height containment is computed by the theory of the linear elastic fracture mechanics, where an equilibrium height status is obtained simultaneously at both upper and lower fracture tips. Meanwhile, the shear slippage of the weak bedding layers is modeled by an efficient 2D higher order displacement discontinuity method based on the joint element (JE-HDDM), and the effectiveness on the hydraulic fracture height is quantified by correcting the stress intensity factors at the hydraulic fracture tips.

Numerical studies based on the Permian Basin Wolfcamp formation using our model demonstrates that the shear slippage of the beddings can significantly slow down the hydraulic fracture height growth and that the shear fracture toughness of the bedding layers and the spacing between the laminations have considerable impact on the effectiveness of the shear slippage on the fracture height growth.

The non-intrusive hydraulic fracture height model is incorporated into an in-house cell based P3D hydraulic fracture simulator, which uses plane strain deformation in each vertical cross-section coupled with a 2D fluid flow. The numerical results show that the weak interfaces have considerable impact on the fracture height, lateral length, and width distribution. With the existence of the weak interfaces, the hydraulic fracture height is reduced, which results in a longer fracture lateral length, together with a reduction of the overall width values. Sensitivity analysis shows that the spacing between the weak interfaces and interfacial shear toughness have significant impact on the fracture geometry and width values. In multi-fracture propagation case, the impact of the weak interfaces on the outer fractures results in a reduction in average height and overall width distribution and an increase of the lateral length. For inner fractures, the impact of weak interfaces varies by the cluster spacing.

The proposed workflow effectively captures the mechanism of the horizontal weak interfaces on the hydraulic fracture height growth and the lateral propagation. The numerical studies provide more understanding on the fracture propagation in the laminated shale reservoirs. The new P3D hydraulic fracture simulator can be used as an effective tool for fracturing job design in shale formations.

DEDICATION

To my beloved parents, Qiang Li and Liyun Wang

ACKNOWLEDGEMENTS

I would like to thank all the individuals who helped and encouraged me to make this dissertation work possible. First and foremost, I would like to express my deepest gratitude to my advisor, Dr. Kan Wu, for her visionary guidance and consistent support throughout my graduate study at Texas A&M University. Her insightful ideas and ingenious perspectives guided me to the right track of research. She is always patient when discussing research problems. I learned a lot from her generous, enthusiastic, and open-minded personality. Under her supervision, I have improved myself not only professionally, but also personally. I am honored to have been in such a friendly and cooperative research group.

I would also like to thank my committee members, Dr. Nobuo Morita, Dr. Eduardo Gildin, Dr. George Moridis and Dr. Benchun Duan, for their time and mentorship, and for their insightful suggestions and comments on my research.

I also feel grateful to all my friends and colleagues for making my time at Texas A&M University a great experience.

Thanks also go to the faculty and staff in the Department of Petroleum Engineering for their technical and administrative support.

Finally, I would like to express my appreciation to my parents for their continuous love, encouragement and support. Their encouragement constantly motivated me in my life and work. I also want to thank my uncle, for his continuous help and support in my life.

CONTRIBUTORS AND FUNDING SOURCES

Contributors

This work was supervised by a dissertation committee consisting of Professor Kan Wu (advisor), Professor Nobuo Morita, Professor Eduardo Gildin and Professor George Moridis of the Department of Petroleum Engineering and Professor Benchun Duan of the Department of Geology and Geophysics.

The data analyzed for Chapters 4 and 5 was provided by Crisman Institute for Petroleum Research.

All other work conducted for the dissertation was completed by the student independently.

Funding Sources

Graduate study was supported by Crisman Institute for Petroleum Research from the Department of Petroleum Engineering.

NOMENCLATURE

A	Plane-strain elastic influencing coefficients between the fracture segments i and j, dimensionless
a_i	Half-lengths of the DDM elements, m
c	Hydraulic fracture half height in Liu and Valko's model, m
C_{ij}	Coefficients for quadratic displacement discontinuity interpolation, dimensionless
D_i	Displacement discontinuities of the fracture segments, m
D_n	Normal displacement discontinuities of the fracture segments, m
D_n^1	Change in width of the fracture tip element, m
D_s	Shear displacement discontinuities of the fracture segments, m
dl	Length of the tip element, m
d_s	Distance from the horizontal interfacial shear slippage tip to the hydraulic fracture, m
E	Young's modulus of the rock, Pa
E'	Plane-strain elastic modulus of the rock, Pa
$E_{ijk}(\omega,\xi)$	Influences of a concentrated force at point ω on displacements at point ξ, dimensionless
$f(x,y)$	Solution functions to the Kelvin's problem, dimensionless
F	Body force, Pa

$g(x,y)$	Solution functions to the Kelvin's problem, dimensionless
$G(x,y)$	Solution function for constant DDM, dimensionless
G^{ij}	3D correction factor for S3D DDM, dimensionless
G	Shear modulus, Pa
h_i	Distance from the i th layer, m
h_f	Hydraulic fracture half height, m
h_f^{str}	Effective straightened hydraulic fracture half height, m
h_{perf}	Perforation depth measured from the fracture lower tip, m
Int^0	Constant integral kernel for HDDM, dimensionless
Int^1	Linear integral kernel for HDDM, dimensionless
Int^2	Quadratic integral kernel for HDDM, dimensionless
Int^c	Integral kernel for tip treatment of HDDM, dimensionless
JRC	Joint roughness coefficient, dimensionless
K_{IC}	First mode fracture toughness, $\mathrm{Pa}\cdot\sqrt{\mathrm{m}}$
$K_{Id}(K_{I-})$	First model stress intensity factor at the bottom tip, $\mathrm{Pa}\cdot\sqrt{\mathrm{m}}$
$K_{Iu}(K_{I+})$	First model stress intensity factor at the upper tip, $\mathrm{Pa}\cdot\sqrt{\mathrm{m}}$
K_n	Normal rigidity of the joint element, Pa
K_s	Shear rigidity of the joint element, Pa
K^{eff}	Effective stress intensity factor, $\mathrm{Pa}\cdot\sqrt{\mathrm{m}}$
L	Fracture half height in Simonson's model, m

L_f	Fluid front location, m
L_s	Shear slip front location, m
L_{str}	Effective half length for straightened fracture, m
$N_j(\xi)$	Quadratic shape functions for higher order interpolation, dimensionless
p_{net}	Net pressure within the fracture segment, Pa
p_{perf}	Fluid pressure at the perforation depth, m
q	Volume rates of the fluid flow per unit length, m^2
r	Half length of the tip element length, m
σ_a	Stress at upper tip in Simonson's model, Pa
σ_b	Stress at bottom tip in Simonson's model, Pa
σ_i	Minimum in-situ stress for ith layer, Pa
$\sigma_{jk}(\omega)$	Stress components at a point ω, Pa
σ_n	Normal stresses on the fracture segments, Pa
$(\sigma_n)^{ind}$	Induced normal stresses on the fracture segments, Pa
σ_s	Shear stresses on the fracture segments, Pa
$(\sigma_s)^{ind}$	Induced shear stresses on the fracture segments, Pa
$\sigma_{s,yield}$	Yield shear stresses of the horizontal weak interface, Pa
σ_v	Vertical in-situ stress, Pa
$T(x,y)$	Normal traction on the fracture surface, Pa

$\Delta u_i(\xi)$	Displacement components at a point ω, m
u_n	Normal displacement, m
u_s	Shear displacement, m
v	Poisson’s ratio, dimensionless
w	Fracture width, m
w_0	Initial fracture aperture without shear slippage, m
w_f	Effective hydraulic aperture, m
w_n	Fracture aperture without shear slippage, m
w_s	Shear slip induced dilation, m
w_{res}	The residual aperture, m
w_{str}	Effective width for straightened fracture, m
Ω	Fracture surface, m^2
ρ	Fluid density, kg/m^3
μ	Fluid viscosity, Pa·s
τ_m	Critical shear stress, Pa
χ	Friction coefficient, dimensionless

TABLE OF CONTENTS

Page

LIST OF FIGURES

LIST OF TABLES

Page

1. INTRODUCTION

1.1. Background and Motivation

The hydraulic fracturing technology is firstly introduced by Clark in 1949 when he provided detailed explanation of the procedure and the requirements of hydraulic fracturing. Oil and gas production in the United States has significantly increased since the advancement in the technique of hydraulic fracturing in unconventional shale reservoirs. Multi-stage hydraulic fracturing in a horizontal well (Figure 1.1) has made possible the flourishing hydrocarbon production from unconventional shale reservoirs. In the hydraulic fracturing design and operation, the height growth of a hydraulic fracture is of great importance. Since the fracture-height growth can be either positive in allowing the fracture to vertically connect the isolated sweet layers to produce through the fracture into the well, or be negative in wasting the energy and effort in non-pay layers, even penetrating into water or gas zones, which severely reduces the oil production rate.

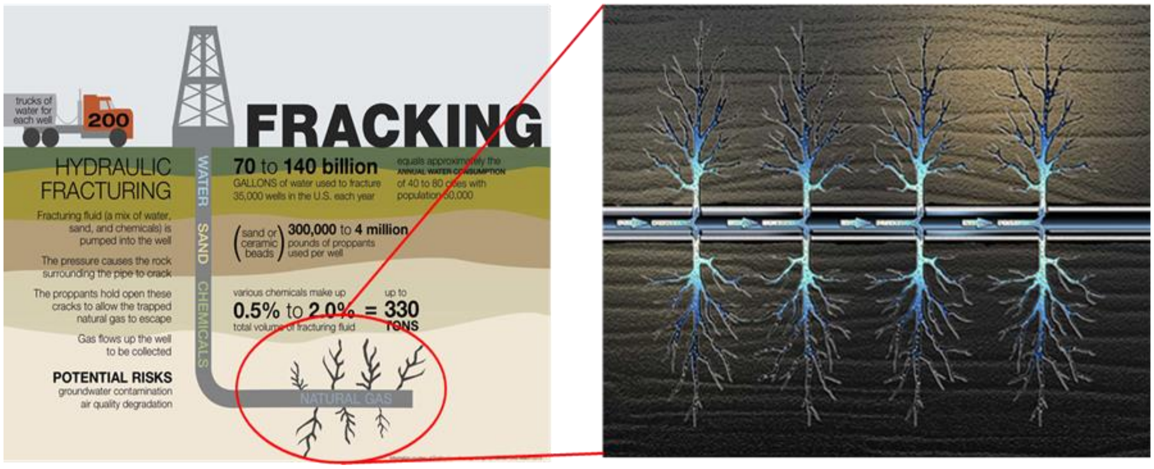

Figure 1.1 Multi-stage hydraulic fracturing in a horizontal well and complex fracture networks (from Schlumberger).

Many techniques have been developed and applied to characterize and monitor the hydraulic fracture height such as the microseismic imaging (Fisher and Warpinski, 2012; Warpinski, 2013; Maxwell, 2014), laboratory experiments (Jeffrey and Bunder, 2009; Xing et al., 2016; Hu and Ghassemi, 2021), low-frequency distributed acoustic sensing (Jin and Roy, 2017; Liu et al., 2021), high-frequency distributed acoustic sensing, distributed temperature sensing (Sierra et al., 2008), and numerical modeling (Simonson et al., 1978; Zhang and Ghassemi, 2011; Weng et al., 2018; Li et al., 2020; Mehrabi et al., 2021). Numerical modeling and simulation are based on the fracture mechanics theory and provide the engineers with an efficient way to monitor the hydraulic fracture propagation and with the guidance of hydraulic fracturing job designs.

Over the last a few decades, based on field observations, laboratory experiments, and numerical studies, several factors have been identified to have significant impact on the hydraulic fracture height growth, such as the minimum in-situ stress contrast between different formation layers, fracture toughness, weak bedding planes/interfaces, mechanical properties, proppant distribution, and fluid leak-off (Daneshy 1978; Warpinski 1991; Gu and Siebrits 2008; Jeffrey and Bunger 2009; Liu and Valko, 2017; Zhao and Gray, 2021). For conventional formations, over the decades of research and development of hydraulic fracturing technology, it has been well-established that the difference of minimum in-situ stress between different formations plays the major role in containing the fracture height (Warpinski et al. 1982; Mendelsohn 1984; Valko´ and Economides 1993; Fisher and Warpinski 2012; Hurt and Germanovich 2012;).

In unconventional shale reservoirs, the formation layers are always accompanied by the weak bedding interfaces such as the bedding layers, laminations, and ash beds. For example, as shown in Figure 1.2, the Montney shale, Eagle Ford shale, Vaca Muerta shale, and Marcellus shale have been observed with the consequences of rock layering and the interfaces between the rock layers. In recent years, it has been evidenced by field microseismicity observations and laboratory experiments that the hydraulic fracture height growth can be significantly affected by the bedding planes and the weak interfaces in the unconventional shale formations (Anderson 1981; Burghardt et al. 2015; Kear et al. 2017; Zeroug et al. 2018; Gamero Diaz et al. 2018). The way the hydraulic fracture height growth being influenced by the bedding layers can be summarized as crossing, slowing down, deflecting, and terminating. According to the experimental results (Teufel and Clark 1984; Bunger et al. 2016), the hydraulic fracture is more likely to cross the bedding interfaces in the higher effective normal stress case while more likely to terminate upon the interfaces in the lower effective normal stress case. In laminated formations with low in-situ stress contrast, the bedding-layer slippage induced by hydraulic fractures could be a dominant factor influencing the hydraulic fracture height.

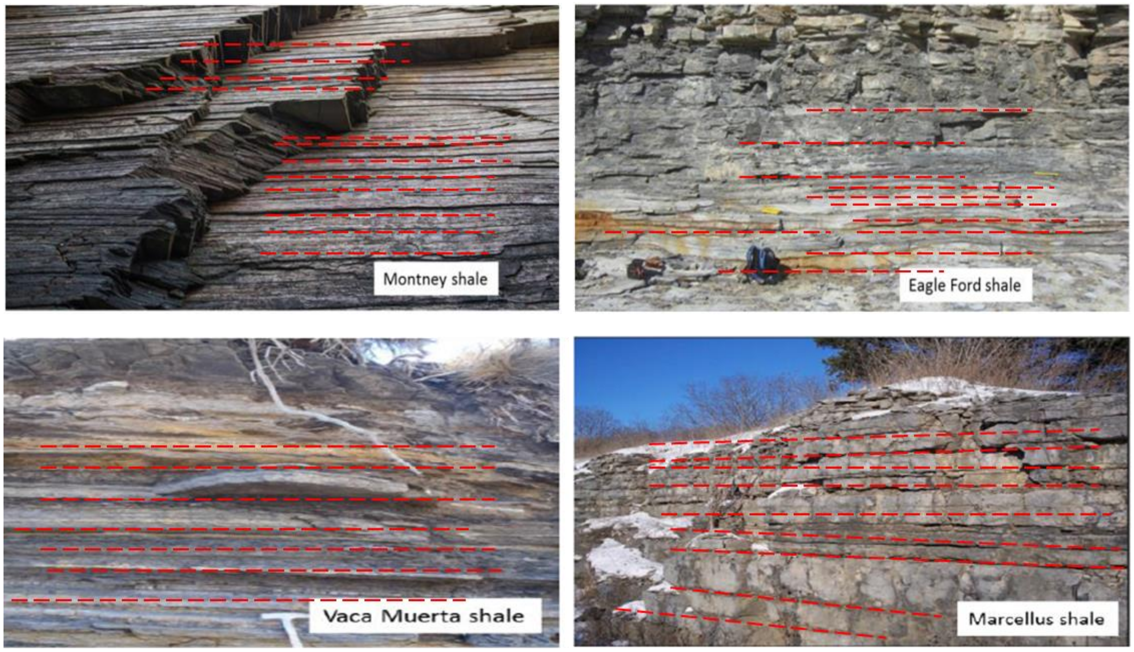

Figure 1.2 Examples of thin rock layering on outcrops from the Montney, Vaca Muerta, Eagle Ford, and Marcellus shales (Suarez-Rivera et al. 2016).

Figure 1.3 shows the stacked package of limestone and the weak interfaces or weak beds in Wolfcamp formation in Permian Basin. The distance between these weak interfaces can be as small as a few feet, and the thickness of these weak beds ranges from a few millimeters to a few feet. Those geo-technical interfaces and beds have considerable impact on the geometries of hydraulic fractures and have significantly increased the complexity of the hydraulic fracture networks as shown in Figure 1.1.

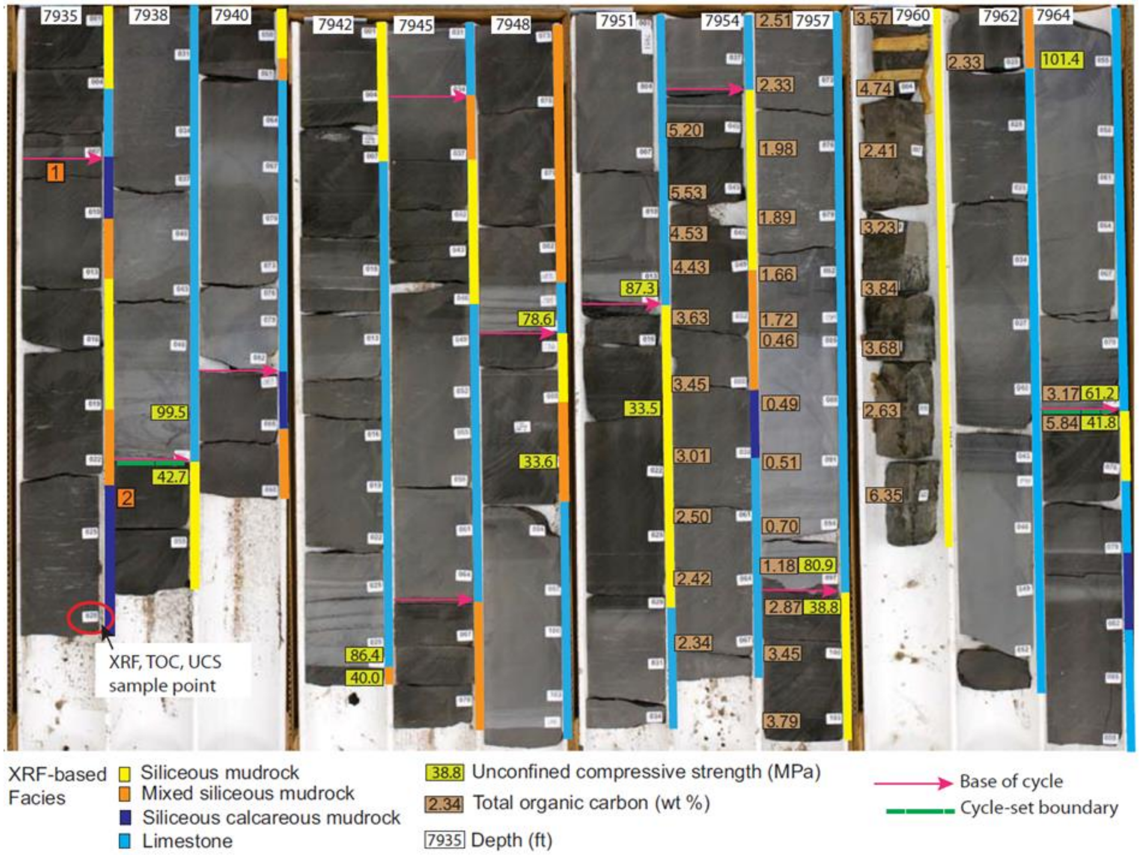

Figure 1.3 Geo-mechanical data and rock composite data of Wolfcamp formations in Permian Basin (Robert et al. 2018).

In such formations where closely-spaced bedding layers and laminations exist, the height propagation of a vertical hydraulic fracture is not only affected by the conventional factors such as the treating pressure, in-situ stress, fracture toughness, Young's modulus, Poisson ratio, fracturing fluid density and viscosity, etc., but can be strongly affected by the horizontal bedding interfaces (Weng et al. 2011; Kresse and Weng 2013; Chuprakov and Prioul 2015; Kress and Weng, 2017; Diaz et al. 2018). An example (Figure 1.4) given by Srinivasan et al (2018) in the Niobrara formation has shown that due to the existence of thin bed laminations rich in bentonites, the hydraulic fracture vertical growth has been limited before it reaches the boundaries.

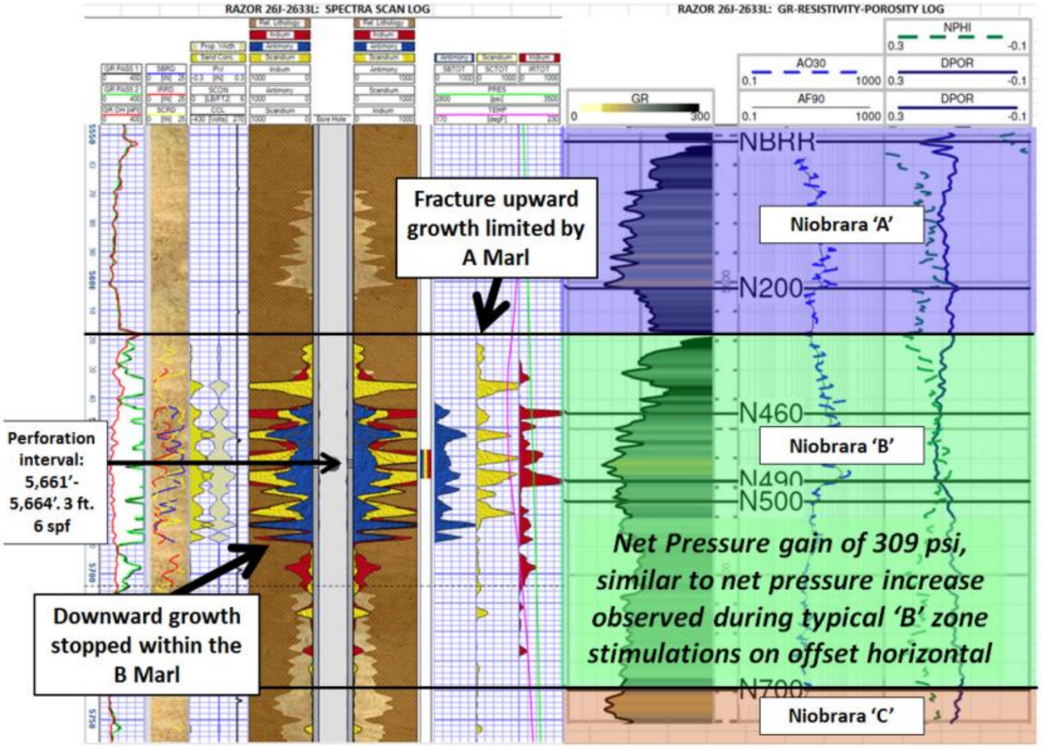

Figure 1.4 Illustration of impact of thin-bed laminations on fracture height growth characteristics in the Niobrara formation (Srinivasan et al. 2018)

To accurately capture the influence of the weak interfaces and the laminations on the hydraulic fracture height containment, plenty of experimental and numerical studies have been conducted since the last two decades. (Kresse and Weng 2013; Diaz et al. 2018; Gao and Ghassemi, 2020; Zhao and Gray, 2021). The experimental studies demonstrated that the bedding layers are affecting the hydraulic fracture propagation by arresting, diverting, or slowing down the vertical growth of fracture height. Quantitative numerical studies show that closely-spaced weak interfaces and beds play a dominant role where the in-situ stress variation between layers are less obvious. These works provided a much better understanding and more accurate prediction of the hydraulic fracture height. However, the existing numerical models are either too sophisticated with a full three-dimensional consideration, or too simplified, which is only limited to a certain case (arresting or diverting) to be incorporated into a general hydraulic fracture design simulator.

The primary objective of this research work in the dissertation is to develop a comprehensive and non-intrusive hydraulic fracture height growth model and incorporate it into a hydraulic fracture propagation simulator to investigate the impact of the horizontal weak interfaces on the hydraulic fracture propagation and the final geometries, and width distributions.

1.2. Literature review

The hydraulic fracturing technology has been studied and developed for more than half century in the oil and gas industry. Prediction of the hydraulic fracture height growth is one of the critical tasks in the design and operations of hydraulic fracturing treatments. Over the last a few decades, it has been widely-recognized that a hydraulic fracture height can be influenced by many factors including the landing depth, perforation pressure, layer interface and its shearing strength, existence of natural fractures, in situ stress, fracture toughness, Young's modulus, Poisson's ratio, tensile strength, fluid leaking off and hydraulic fracturing fluid density (Simonson et al. 1978; Warpinski et al. 1982a; Valko´ and Economides 1993; Abbas et al. 2014; Liu and Valko, 2017).

1.2.1. Hydraulic fracture height models without the effect of weak interfaces

Among all of these influencing factors for hydraulic fracture height growth, the in-situ stress has been acknowledged as the most important factor of containing the hydraulic fracture height in conventional formations. According to previously laboratory and numerical studies, higher in-situ horizontal stress variation between different layers results in smaller hydraulic fracture height, and vice versa (Van Eekelen 1982; Warpinski et al. 1982). Similarly, the fracture toughness is another one of the primary influencing factors controlling the hydraulic fracture height. The fracture toughness is more influencing when the hydraulic fracture is in small scale where the stress variation is less comparable (Thiercelin et al. 1989; Garagash and Detournay 2005; Garagash 2006; Zhang et al. 2010). When the bedding layer exists and are shearing during the hydraulic fracturing, the fracture toughness of the bedding layers may increase in a considerable manner (Morita et al. 1988). The Young's modulus and the Poisson's ratio are the indirect factor for hydraulic fracture height since they affect the height growth by affecting the hydraulic fracture width and the net pressure, as well as the induced horizontal stress profile in target layers. Higher Young's modulus usually leads to narrower fracture widths and larger pressure drop, which results in a shorter overall fracture height. As for the fracturing fluid leaking off into the bedding layers or the weak interfaces, it reduces the pressure in the fracture and slows down the hydraulic fracture height growth (Ahmed 1984; Kresse and Weng 2013; Diaz et al. 2018).

To predict the hydraulic fracture height considering the above-analyzed influencing factors, the so called “equilibrium height belonging to a certain treating pressure” was proposed and developed which can provide an upper limit of the hydraulic fracture height (Simonson et al. 1978; Economides and Nolte 2000; Mack and Warpinski 2000; Weng et al. 2011; Liu and Valko 2017). The “equilibrium status” means when given a treating pressure, the integration of the net pressure inside the fracture along the height (i.e. SIF, K_I) is equal to the fracture toughness K_{Ic} at both upper and lower tips at the same time. If the computed SIFs at either tip is higher than the K_{Ic} at the layer in consideration, the specific tip will grow and propagate, until the computed SIF becomes equal or slightly less than the K_{Ic} of the layer.

The solution for the equilibrium height has been investigated and developed since 1970s. The earliest is given by Simonson et al. in 1978 for a symmetric three-layer formation problem with exactly the same upper and lower minimum horizontal stress and the constant treating pressure along the fracture height, which is given in Equation (1.1).

$$p_{net} = \frac{K_{IC}}{\sqrt{\pi L}}[\frac{1}{\sqrt{1+\varepsilon}} - 1] + 2\frac{\sigma_b - \sigma_a}{\pi}\arccos(\frac{1}{1+\varepsilon}) \qquad (1.1)$$

where p_{net} is the net pressure inside the fracture segment, K_{IC} is the first mode fracture toughness, σ_a and σ_b are stress at fracture tips.

The symmetric-three-layer solution was then extended by Mack and Warpinski to asymmetric multilayer formation problems and is given by Equation (1.2).

$$K_{Iu} = \sqrt{\frac{\pi h_f}{2}} p_{net} + \sqrt{\frac{2}{\pi h_f}} \sum_{i=1}^{n-1} (\sigma_{n+1} - \sigma_i)[\frac{h_f}{2} \cos^{-1}\left(\frac{h_f - 2h_i}{h_f}\right) - \sqrt{h_i(h_f - h_i)}] \quad (1.2)$$

where K_{Iu} is the upper tip stress intensity factor, h_f is the fracture half height, and h_i is the distance from the ith layer.

In 2011, Weng et al. provided more details of the asymmetric multi-layer formation studies and demonstrated the liability of the equilibrium height model. Liu and Valko (2018) have summarized the previous development of the equilibrium height mode and provided more case studies to investigate the effect of rock formation properties on the hydraulic fracture height. The equations they used (Equation (1.3)) are more straightforward and can be easily implemented using numerical algorithms into problems shown by Figure 1.5.

$$\begin{aligned} K_{I+} &= \sqrt{\frac{1}{\pi c}} \int_{-c}^{c} p_{net}(x) \sqrt{\frac{c+x}{c-x}} dx \\ K_{I-} &= \sqrt{\frac{1}{\pi c}} \int_{-c}^{c} p_{net}(x) \sqrt{\frac{c-x}{c+x}} dx \end{aligned} \quad (1.3)$$

where c is the fracture half height, K_{I+} and K_{I-} are the stress intensity factors at the fracture upper and lower tips, respectively.

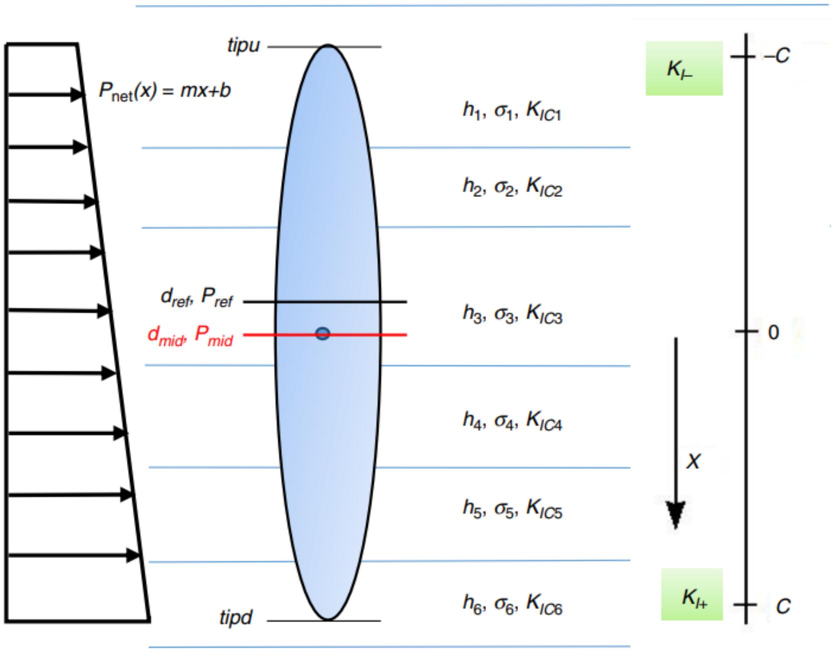

Figure 1.5 Equilibrium hydraulic fracture height in a multilayer formation with hydrostatic fluid pressure inside (Liu and Valko 2018).

The equilibrium height model provides reasonable and reliable height growth map for conventional multi-layer formations. Yet it does not consider the effect of the bedding layers and laminations.

Except from the equilibrium height model, there are other models such as the cohesive zone model and the plane strain model based on the 2D displacement discontinuity method. These models provide more details on the fracture height and the width profile; however, the computational efforts are too expensive to be efficiently applied in fracture simulators for field-scale engineering design.

However, the above-mentioned models generally overestimate the hydraulic fracture height, and the computed hydraulic fracture height is actually an upper limit, especially in shale formations (Liu and Valko 2018; Weng et al. 2018; Kress and Weng 2019). This is because the shale formations are often accompanied by thin laminations and multi-closely-spaced interfaces (Suarez-Rivera et al. 2016; Gamero Diaz et al. 2018) and these weak interfaces may slow down, deflect, or terminate a vertical hydraulic fracture (Zhang and Jeffrey 2008; Daneshy 2009). In conventional formations, this mechanism has hardly drawn attention in characterizing the fracture height growth since few bedding layers are activated during the hydraulic fracturing process and the in-situ stress contrast plays the primary role. On the contrast, in the unconventional shale reservoirs, this mechanism has regained its attention as numerous observations of downhole ultrasonic logs (Zeroug et al. 2018), borehole images (Gamero Diaz et al. 2018), and microseismic events (Rutledge et al. 2016) have evidenced the slippage of the bedding layers. In addition, intensive experimental efforts have demonstrated the significant impact of the bedding-plane slippage on the hydraulic fracture height containment (Burghardt et al. 2015).

1.2.2. Hydraulic fracture height models with the effect of weak interfaces

In unconventional shale formations, weak interfaces and weak beds are always observed. The distance between these weak interfaces can be as small as a few feet, and the thickness of these weak beds ranges from a few millimeters to a few feet. Those geo-technical interfaces and beds have considerable impact on the geometry of hydraulic fractures and have significantly increased the complexity of the hydraulic fracture networks.

Accurate modeling of the hydraulic fracture height in shale laminations has long been a challenge for the oil and gas industry due to various impacting factors as well as the complex subsurface conditions. The hydraulic fracture height growth and lateral propagation in a laminated reservoir is generally a fully-3D problem which involves rock deformation of the fracture coupled with fluid flow inside the fracture. Solving the problem of coupled rock deformation and fluid flow for fracture propagation requires intensive fine grids and huge amount of computational effort, and therefore the problem is often simplified and reduced to the so-called "Pseudo three dimensional" (P3D) problem which contains the hydraulic fracture height growth module and the lateral propagation part. The P3D models maintain the accuracy of approximation but reduce the computational requirement to a large extent, which have been widely adopted in hydraulic fracture modeling in the oil and gas industry (Mack and Warpinski 2000; Adachi et al. 2007; Weng et al. 2018).

Multiple numerical models have been proposed and developed to account for the effect of bedding layers . Zhang and Jeffrey (2008) adopted the two-dimensional displacement discontinuity method (DDM) to investigate the penetration, alteration or arresting of the hydraulic fracture height when encountering the bedding layers. Apart from the DDM, the cohesive-zone model was also applied to study the height growth considering the bedding planes and weak beds (Park et al. 2009). In 2015, Chuprakov et al. provided another way of considering the effect of weak interfaces on hydraulic fracture height by assuming the "H-shape" or "T-shape" of the fracture and introducing a semi-analytical solution for the fracture height and width. In 2019, Xu et al. for the first time considered the fluid leaking off and energy loss of the hydraulic fracture when encountering the bedding layers using an energy equilibrium model. Besides, many other numerical models have been developed to quantitatively analyze the impact of the bedding layers on the hydraulic fracture height growth (Cooke and Underwood 2001; Thiercelin and Makkhyu 2007; Rho et al. 2017; Weng et al. 2018; Tang and Wu 2018; Xu et al. 2019; Kress and Weng 2019). The modeling work enhances understanding of the fracture-interface interaction mechanism and helps bridge the field-monitoring observations and the characterization of fracture geometries.

However, most of the models are computationally-expensive, which prevent incorporating them into hydraulic fracture simulators. Chuprakov and Prioul (2015) proposed an efficient analytical model, which is so call the "FracT" model (as shown in Figure 1.6), that characterizes the hydraulic fracture and weak interface intersection, as well as the shear slippage of the bedding interfaces. The FracT model was then adopted by Weng et al (2018) and Kresse and Weng (2019) to quantify the effectiveness of the bedding interfaces on the hydraulic fracture height and incorporated into a Pseudo-3D-based hydraulic fracture simulator, which is referred to Unconventional Fracturing Model (UFM). This workflow accurately and efficiently captures the mechanism of the bedding layers influencing the hydraulic fracture height propagation. However, as mentioned in the paper, the analytical solution of the FracT model was developed based on the T-shaped and H-shaped hydraulic fractures with a piece-wise constant stress profile. In shale formations with thin laminations and numerous closely-spaced bedding layers, the actual interaction scheme of the fracture-interface may not strictly follow the T-shape or H-shape. In such cases, an efficient numerical model regarding the fracture-interface interaction might be an alternative.

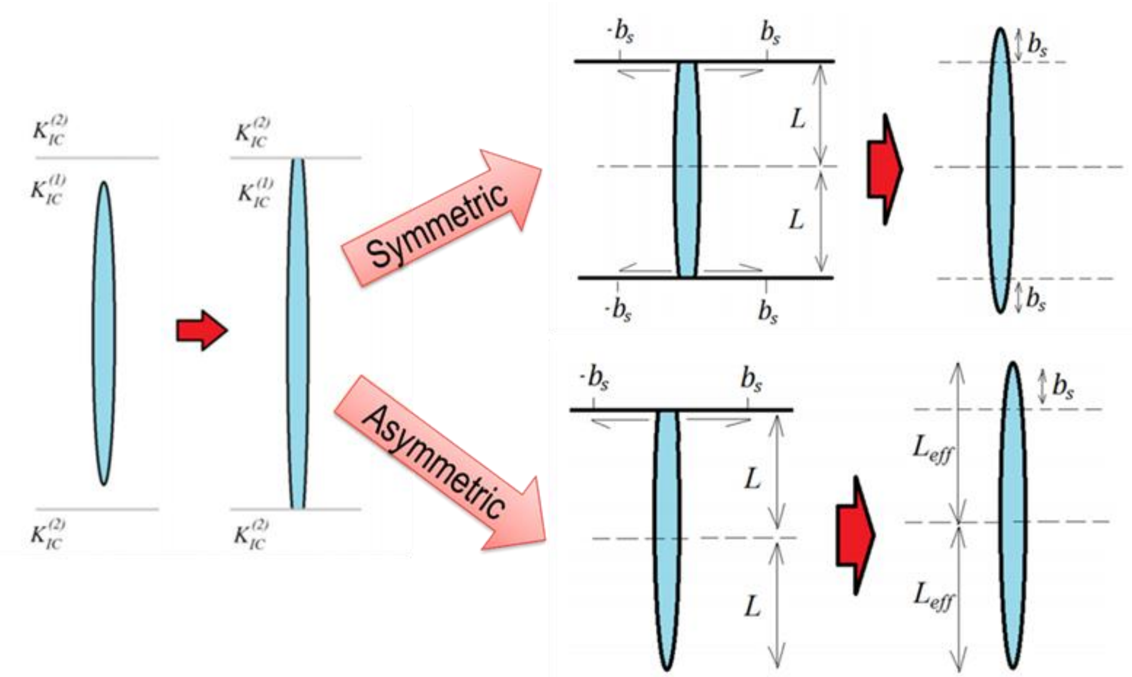

Figure 1.6 Illustration of the T-shaped and H-shaped hydraulic fracture intersection with existing horizontal interface using the fracture straightening method (Adapted from Chuprakov and Prioul 2015).

1.2.3. Hydraulic fracture propagation in laminations

Hydraulic fracturing in shale laminations where natural fractures and horizontal weak interfaces are widely distributed has often resulted in complex fracture networks. Although the hydraulic fracturing technique has been studied and developed for decades, it is still challenging to understand the fracture propagation behavior and to predict the final fracture geometry in shale formations. The difficulties lie in the uncertainly in the subsurface geology and the complexity of the involved physical processes such as the rock deformation of the formation, fluid flow in the fractures, fluid driven fracture propagation, proppant distribution, and fluid driven horizontal interfacial shear slippage etc., which are tightly coupled with each other (Gu 1987; Adachi et al. 2007; Wu et al. 2012; Weng 2015; Hu et al. 2018). The coupling of the solid deformation, fluid flow, and the fracture propagation has been intensively studied by numerous work (Jeffrey et al. 2010; Weng et al. 2011; Sesetty and Ghassemi 2013; Wu and Olson 2015; Detournay 2016; Lecampion et al. 2018; Zheng et al. 2019). However, the understanding of the impact of the horizontal weak interfaces on the fracture propagation behavior and the final geometries remains large space of improvement.

Horizontal weak interfaces have been evidenced by both field observations and laboratory experiments to have impact on the hydraulic fracture vertical propagation (Teuful and Clark 1984; Cooke and Underwood 2001; Rutledge et al. 2014; Suarez-Rivera et al. 2016; Rutledge et al. 2016). Normally, the interaction with a pre-existing horizontal weak interface may result in either a reduction in the hydraulic fracture height growth rate, or a complete arrest of the hydraulic fracture (including diversion), or an offset from the existing path (including branching), depending on the strength and the frictional properties, the in-situ horizontal stress variation between layers, the effective vertical stress at the interface, and the net pressure (Zhang and Jeffery, 2006; Thiercelin et al. 1987; Tang et al. 2018b). The fracture arresting and the fracture offset has been numerically investigated by Jeffery et al. (1987) and experimentally investigated by Teufel and Clark (1984). A similar conclusion was obtained that the fracture termination upon meeting a horizontal interface is more likely to occur with lower normal stress acting on the interface; while crossing the interface usually happens with high normal stress and high interfacial friction. The reduction of the hydraulic fracture height growth rate caused by the horizontal interfaces or bedding planes has been qualitatively assessed by the field studies (Warpinski and Teufel 1987; Rutledge et al. 2016;), laboratory experiments (Bunger et al. 2015; Llanos et al. 2017), and quantitatively studied by numerical analysis (Zhang and Jeffrey 2008; Gu and Weng 2010; Abbas et al. 2014; Chuprakov and Prioul 2015; Zou et al. 2016; Weng et al. 2018). A consensus is obtained that the impact of the horizontal interfaces on the fracture height growth is more significant in formations with low in-situ stress variation between layers than that with high in-situ stress variation between layers.

Compared to the study on the hydraulic fracture vertical growth and height profile influenced by the weak interfaces, the study of the impact on the fracture width and the fracture lateral length is less intensive. Gu et al. (2008) incorporated an interfacial slip model to a pseudo-three-dimensional (P3D) hydraulic fracture simulator and indicated that interfacial slippage along the bedding planes plays a significant role in determining the fracture height growth, fracture width deformation, and entire fracture geometry. Zhang and Jeffery (2006) developed a coupled fluid and elasticity model to analyze the capacity of the pre-existing interfaces to blunt or to change the direction of a fluid-driven hydraulic fracture, and found that the interaction between the pre-existing interface and the hydraulic fracture causes a reduction in vertical fracture width as well as a retardation of the vertical growth rate. Tang et al. (2018a) developed a 3-d hydraulic fracture propagation model applied for multiple-layered considering the effect of horizontal bedding planes. A different width distribution is observed through his study due to the interaction between the vertical fracture and the horizontal plane. Kress and Weng (2019) applied the displacement discontinuity method to investigate the impact of the weak interfaces on the hydraulic fracture height and overall shape, revealing the consideration of the interfacial slip could lead to more contained fractures with shorter height and greater lateral length.

1.3. Objectives

In this work, the objective is to develop a comprehensive and non-intrusive hydraulic fracture height growth model, which not only considers the effect of formation rock mechanical properties, but also quantitatively consider the effect of weak interfaces and bedding layers on the hydraulic fracture height containment, and incorporate the non-intrusive height model into a general hydraulic fracture propagation simulator.

The unifying theme is to study the fundamental physical mechanism of the bedding planes interaction with the hydraulic fracture and the consequent impact on the hydraulic fracture propagation. The process can be divided in four phases:

Phase I: develop an efficient numerical model that is able to accurately capture the impact of formation rock properties, including the in-situ stress variation, fracture toughness, etc. on the hydraulic fracture height containment.

Phase II: develop a coupled fluid flow and rock deformation model for to study the shear dilation of the bedding layers induced by the hydraulic fracture and its impact on the hydraulic fracture height containment. In this phase, the Joint-Element Displacement Discontinuity Method (JE-HDDM) is proposed and developed to overcome the limitations of constant Displacement Discontinuity Method (DDM) which is commonly used in hydraulic-fracture related geo-mechanical problems.

Phase III: incorporate the efficient hydraulic fracture height model with the bedding layer shear dilation model to be a comprehensive height model.

Phase IV: incorporate the comprehensive and non-intrusive hydraulic fracture height model into a general hydraulic fracture propagation simulator.

1.4. Outline of the Dissertation

This dissertation consists of six chapters. In this chapter (Chapter 1), the background and motivation of this research work is introduced, followed by the literature review of the related topics. Then the research objectives are discussed.

Following this chapter, Chapter 2 introduce the Joint-Element based Higher Order Displacement Discontinuity Method (JE-HDDM) developed from the Constant Displacement Discontinuity Method (CDDM). The joint elements are introduced to simultaneously determine the opening, shearing, and closing of each fracture element based on the stress boundary condition, which can avoid the “negative width” of the inner fractures given by CDDM which are mechanically closed under the strong stress shadowing effect. The newly developed JE-HDDM is validated against the CDDM with a typical case. Then a series of numerical case studies based on a close-spacing planar-fracture scenario is provided to demonstrate the effectiveness and efficiency of the JE-HDDM.

In Chapter 3, the JE-HDDM is used to solve the rock deformation problem coupled with the fluid flow in the problem of the intersection between he horizontal weak interface and the vertical hydraulic fracture. Through the numerical modeling, the initiation and the propagation of the shear slippage along the horizontal interface induced by a vertical hydraulic fracture is simulated. Meanwhile, a static model to effectively quantify the impact of the horizontal interfacial shearing on the hydraulic fracture height growth is introduced.

In Chapter 4, the static interfacial shear slippage model is incorporated into an equilibrium height growth model to consider the effect of the horizontal weak interfaces on the fracture height. The effectiveness on the hydraulic fracture height is quantified by correcting the stress intensity factors at the hydraulic fracture tips. The model is applied in the Permian Basin Wolfcamp formation to quantitatively investigate the effect of bedding layers on the hydraulic fracture height growth.

In Chapter 5, the comprehensive hydraulic fracture height growth model is incorporated into an in-house cell-based P3D hydraulic fracture simulator, which uses plane strain deformation in each vertical cross-section coupled with a 2D fluid flow. Numerical examples are performed based on a Midland Basin Wolfcamp shale formation to study the impact of the weak interfaces on the fracture propagation and the final geometry. The proposed workflow effectively captures the mechanism of the horizontal weak interfaces on the hydraulic fracture height growth and the lateral propagation.

Finally, Chapter 6 summarizes the conclusions obtained from this dissertation and provides some pertinent recommendations for future research on this topic.

2. JOINT-ELEMENT HIGHER ORDER DISPLACEMENT DISCONTINUITY METHOD[*]

2.1. Introduction

Multi-stage hydraulic fracturing in a horizontal well has made possible the flourishing hydrocarbon production from unconventional shale reservoirs. To sustain the economical production of unconventional resources, more intensive completions with closer cluster spacing are used in unconventional shale reservoirs (Evans, et al., 2018; Smye, et al., 2020). In unconventional shale reservoirs where the matrix permeability is ultra-low, wells do not drain much farther beyond the hydraulic fractures, and therefore the optimal completion designs of the cluster spacing is much smaller than the previously used, which can be as small as 10 feet (Xiong, et al. 2018; Xiong, et al. 2019; Zheng, et al. 2019; Weijermars, 2020). In close-spacing-fractured reservoirs, the fracture behavior is significantly affected by the stress shadowing effect and becomes challenging to be predicted.

To better understand the hydraulic fracture propagation behavior and the consequent improvement on oil and gas production, numerical analysis and modeling of the hydraulic fracture propagation have been intensively conducted by researchers and engineers. The Constant Displacement Discontinuity Method (CDDM) has been widely used to model rock deformation and characterize the hydraulic fracture geometry due to

---

[*] Part of this chapter is reprinted with permission from “A New Higher Order Displacement Discontinuity Method Based on the Joint Element for Analysis of Close-Spacing Planar Fractures” by Li, J., Liu, Y. and Wu, K., 2022. SPE Journal, 27(02), pp.1123-1139. Copyright [2022] by Society of Petroleum Engineers.

its computational efficiency and flexibility to address non-planar fracture geometry (Detournay and Cheng, 1991; Ghassemi, 1997; Ghassemi and Zhang, 2006; Olson, 2008; McClure, 2012; Rafiee, et al. 2012; Wu, 2018). Many dynamic fracture propagation simulators employ the CDDM to calculate fracture opening and shearing as well as induced stresses during fracturing (Wu and Olson, 2013; Weng, 2015; Zeng and Yao, 2016; Kress and Weng, 2018; Shrivastava and Sharma, 2018). Another promising application is to use the CDDM to develop a forward model for data interpretation of low-frequency distributed acoustic sensing (LF-DAS) and detection of fracture hits (Liu, et al., 2020, 2021; Zhang, et al., 2020). Besides, CDDM is also a significant tool in analysis of interactions between the hydraulic fractures and weak interfaces (Zhang, et al., 2012; Tang, et al., 2018; Tang, et al., 2019).

Although the CDDM shows the accuracy and efficiency in solving geo-mechanical problems in hydraulic fracturing, the assumption of constant displacement discontinuity distribution on each element limits its accuracy in predicting the stresses and displacements for field points closer than approximately one element length from a boundary (Crawford and Curran, 1982; Shou and Crouch, 1995). This mathematical deficiency is negligible when the fracture spacing in multi-stage fracture pattern is relatively large or the fracture half-length is relatively small (Ghassemi, 1997). However, as smaller cluster spacing with large injection volume, correspondingly smaller fracture spacing with large fracture half-length, is used by multi-stage hydraulic fracturing treatments, the results of the CDDM deviate from the accurate ones and become inaccurate and unreliable. Moreover, another significant problem observed in close fracture-spacing case is that the inner fractures have “negative width” due to strong stress shadowing effect given by the results from the CDDM. The “negative width” solutions mathematically satisfy the boundary conditions but are physically unrealistic. In addition, the displacement discontinuities are key parameters in calculating the stress intensity factors (SIFs) which govern the propagation of the fractures and the stresses around the fracture tips and are vital in analysis of fracture interactions (Zhang, et al., 2012; Weng, 2015; Li, et al., 2020).

To mitigate the mathematical deficiency of the CDDM, higher order approximations of displacement discontinuity were proposed and implemented (Crawford and Curran, 1982; Shou and Crouch, 1995), which significantly improved the accuracy of DDM. Crawford and Curran’s method implemented the higher order approximations by introducing additional collocation points within each element, indicating that the improvement of accuracy comes at the expense of huge amount of computational time. In Shou and Crouch’s method, the higher order distribution of displacement discontinuity was interpolated along the patched elements which does not introduce additional computational points, indicating that this higher order displacement discontinuity method (HDDM) does not increase the computational time but improves the accuracy to a large extent.

To avoid the negative opening of inner fractures due to strong stress shadowing effect of close-spacing fractures, the joint elements with three contact modes: stick, shear, and open, are introduced to original DDM. Each contact mode has its own specific governing equations relating the displacement discontinuities and the boundary stresses

(Crouch and Starfield, 1983; Pine and Batchelor, 1984). Given boundary stress conditions, the contact mode of each element of the fractures and the corresponding displacement discontinuities are solved simultaneously and iteratively until all the contact modes and displacement discontinuities converge.

In this section, we developed the Joint Element based Higher order Displacement Discontinuity Method (JE-HDDM) to study the closely spaced fracture behavior. This JE-HDDM gives the same results with the CDDM when fracture spacing is large. However, for closely spaced fracture problems where the CDDM fails to accurately predict the fracture behavior, the combination of stick and open mode of the joint elements in the JE-HDDM eliminates the negative width of the inner fractures calculated by the CDDM, and presents the results in a pattern of opening part and closing part of the fracture segments. Our study helps us understand the limitations of the CDDM in close-spacing fracture problems and introduced a new technique, the JE-HDDM, for analysis of geo-mechanical problems where multi-close-spacing fractures exist.

2.2. Efficient higher order displacement discontinuity method formulation

The new method, JE-HDDM, is developed originally from the displacement discontinuity method (DDM), a boundary element method that expresses the stresses and displacements at a point due to a constant displacement discontinuity over a line segment in an elastic body. The higher order collocation of the displacement discontinuities is applied on the elements with different joint contact types and the corresponding equations.

2.2.1. Three-element patch for a fracture element

The efficient HDDM employs the quadratic approximation of displacement discontinuity along a three-element patch, as shown in Figure 2.1. Figure 2.1 depicts the collocation patch for a straight fracture where all elements are in the same inclination. As shown in the figure, a_1, a_2 and a_3 are the half-lengths of the three elements, $(D_i)_1$, $(D_i)_2$, and $(D_i)_3$ are the corresponding nodal displacement discontinuities, respectively.

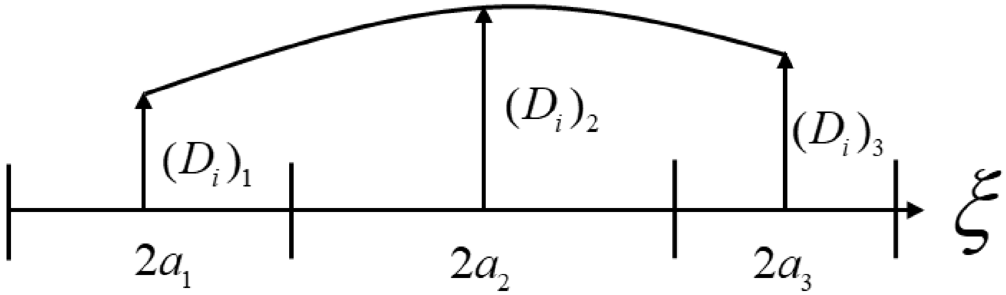

Figure 2.1 The patched-element pattern for quadratic collocation of displacement discontinuities of the efficient HDDM (modified from Shou and Crouch, 1995).

In each patch of the three elements, three collocation points are used for shape functions, one at the center of the source element and others at the centers of the adjacent elements. The three collocation points from three adjacent elements make it possible to conduct quadratic interpolation of the displacement discontinuities over the elements without increasing the degrees of freedom, i.e., the computational time. The quadratic distribution of the displacement discontinuities is expressed in Equation (2.1) (Shou and Crouch, 1995):

$$D_i(\xi) = \sum_{j=1}^{3} N_j(\xi) D_i(j), i = x, y \tag{2.1}$$

where $N_j(\xi)$ are the quadratic shape functions given as:

$$\begin{aligned}
N_1(\xi) &= \xi(\xi - a_2 - a_3) / [(a_1 + a_2)(a_1 + 2a_2 + a_3)] \\
N_2(\xi) &= -(\xi + a_1 + a_2)(\xi - a_2 - a_3) / [(a_1 + a_2)(a_2 + a_3)] \\
N_3(\xi) &= \xi(\xi + a_1 + a_2) / [(a_2 + a_3)(a_1 + 2a_2 + a_3)]
\end{aligned} \tag{2.2}$$

Substituting Equation (2.2) to Equation (2.1) gives:

$$\begin{aligned}
&D_i(\xi) \\
&= [-\frac{-a_1a_2 - a_1a_3 - a_2{}^2 - a_2a_3}{(a_1 + a_2)(a_2 + a_3)}(D_i)_2] \\
&+[\frac{-a_2 - a_3}{(a_1 + a_2)(a_1 + 2a_2 + a_3)}(D_i)_1 - \frac{-a_2 - a_3 + a_1 + a_2}{(a_1 + a_2)(a_2 + a_3)}(D_i)_2 + \frac{a_1 + a_2}{(a_2 + a_3)(a_1 + 2a_2 + a_3)}(D_i)_3]\xi \\
&+[\frac{1}{(a_1 + a_2)(a_1 + 2a_2 + a_3)}(D_i)_1 - \frac{1}{(a_1 + a_2)(a_2 + a_3)}(D_i)_2 + \frac{1}{(a_2 + a_3)(a_1 + 2a_2 + a_3)}(D_i)_3]\xi^2 \\
&= \left[C_{01}(D_i)_1 + C_{02}(D_i)_2 + C_{03}(D_i)_3\right] \\
&+ \left[C_{11}(D_i)_1 + C_{12}(D_i)_2 + C_{13}(D_i)_3\right]\xi \\
&+ \left[C_{21}(D_i)_1 + C_{22}(D_i)_2 + C_{23}(D_i)_3\right]\xi^2 \\
&= \left[(D_i)_1 \quad (D_i)_2 \quad (D_i)_3\right] \begin{bmatrix} C_{01} & C_{11} & C_{21} \\ C_{02} & C_{12} & C_{22} \\ C_{03} & C_{13} & C_{23} \end{bmatrix} \begin{bmatrix} 1 \\ \xi \\ \xi^2 \end{bmatrix}
\end{aligned}$$

(2.3)

where

$$
\begin{aligned}
C_{01} &= 0 \\
C_{02} &= -\frac{-a_1a_2 - a_1a_3 - a_2{}^2 - a_2a_3}{(a_1+a_2)(a_2+a_3)} \\
C_{03} &= 0 \\
C_{11} &= \frac{-a_2 - a_3}{(a_1+a_2)(a_1+2a_2+a_3)} \\
C_{12} &= -\frac{-a_2 - a_3 + a_1 + a_2}{(a_1+a_2)(a_2+a_3)} \\
C_{13} &= +\frac{a_1 + a_2}{(a_2+a_3)(a_1+2a_2+a_3)} \\
C_{21} &= \frac{1}{(a_1+a_2)(a_1+2a_2+a_3)} \\
C_{22} &= -\frac{1}{(a_1+a_2)(a_2+a_3)} \\
C_{23} &= \frac{1}{(a_2+a_3)(a_1+2a_2+a_3)}
\end{aligned}
\tag{2.4}
$$

2.2.2. Higher order formulation

The higher order formulation is derived from the original two-dimensional DDM which is based on the analytical solution of plane-strain problem for the stresses due to the displacement discontinuities D_x and D_y along the fracture segment $\left|x\right| \le a, y = 0$ (Crouch 1976).

$$
\begin{aligned}
\sigma_{xx} &= 2G\left[2f_{,xy} + yf_{,xyy}\right] + 2G\left[2g_{,yy} + yg_{,yyy}\right] \\
\sigma_{yy} &= 2G\left[-yf_{,xyy}\right] + 2G\left[g_{,yy} - yg_{,yyy}\right] \\
\sigma_{xy} &= 2G\left[f_{,yy} + yf_{,yyy}\right] + 2G\left[-yg_{,xyy}\right]
\end{aligned}
\tag{2.5}
$$

where $\sigma_{xx}, \sigma_{yy}, \sigma_{xy}$ are the stress components, v is the Poisson's ratio, G is the shear modulus, $f(x,y)$ and $g(x,y)$ are solution functions to the Kelvin's problem and are defined as following:

$$\begin{aligned} f(x,y) &= \frac{-1}{4\pi(1-v)} \int_{-a}^{a} D_x(\xi) \ln[(x-\xi)^2 + (y)^2]^{0.5} d\xi \\ g(x,y) &= \frac{-1}{4\pi(1-v)} \int_{-a}^{a} D_y(\xi) \ln[(x-\xi)^2 + (y)^2]^{0.5} d\xi \end{aligned} \tag{2.6}$$

whose quadratic format can be derived by substituting Equation (2.6) into Equation (2.3) and are given here by Equations (2.7) and (2.8):

$$\begin{aligned} f(x,y) &= \frac{-1}{4\pi(1-v)} \int_{-a}^{a} D_x(\xi) \ln[(x-\xi)^2 + (y)^2]^{0.5} d\xi \\ &= \frac{-1}{4\pi(1-v)} \int_{-a}^{a} \left[C_{01}(D_x)_1 + C_{02}(D_x)_2 + C_{03}(D_x)_3\right] \ln[(x-\xi)^2 + (y)^2]^{0.5} d\xi \\ &+ \frac{-1}{4\pi(1-v)} \int_{-a}^{a} \left[C_{11}(D_x)_1 + C_{12}(D_x)_2 + C_{13}(D_x)_3\right] \xi \ln[(x-\xi)^2 + (y)^2]^{0.5} d\xi \\ &+ \frac{-1}{4\pi(1-v)} \int_{-a}^{a} \left[C_{21}(D_x)_1 + C_{22}(D_x)_2 + C_{23}(D_x)_3\right] \xi^2 \ln[(x-\xi)^2 + (y)^2]^{0.5} d\xi \\ &= \frac{-1}{4\pi(1-v)} \left[(D_x)_1 \quad (D_x)_2 \quad (D_x)_3\right] \begin{bmatrix} C_{01} & C_{11} & C_{21} \\ C_{02} & C_{12} & C_{22} \\ C_{03} & C_{13} & C_{23} \end{bmatrix} \begin{bmatrix} Int^0 \\ Int^1 \\ Int^2 \end{bmatrix} \end{aligned} \tag{2.7}$$

$$
\begin{aligned}
g(x,y) &= \frac{-1}{4\pi(1-v)}\int_{-a}^{a} D_y(\xi)\ln[(x-\xi)^2+(y)^2]^{0.5}\,d\xi \\
&= \frac{-1}{4\pi(1-v)}\int_{-a}^{a}\left[C_{01}(D_y)_1+C_{02}(D_y)_2+C_{03}(D_y)_3\right]\ln[(x-\xi)^2+(y)^2]^{0.5}\,d\xi \\
&+ \frac{-1}{4\pi(1-v)}\int_{-a}^{a}\left[C_{11}(D_y)_1+C_{12}(D_y)_2+C_{13}(D_y)_3\right]\xi\ln[(x-\xi)^2+(y)^2]^{0.5}\,d\xi \qquad (2.8) \\
&+ \frac{-1}{4\pi(1-v)}\int_{-a}^{a}\left[C_{21}(D_y)_1+C_{22}(D_y)_2+C_{23}(D_y)_3\right]\xi^2\ln[(x-\xi)^2+(y)^2]^{0.5}\,d\xi \\
&= \frac{-1}{4\pi(1-v)}\begin{bmatrix}(D_y)_1 & (D_y)_2 & (D_y)_3\end{bmatrix}\begin{bmatrix}C_{01} & C_{11} & C_{21}\\ C_{02} & C_{12} & C_{22}\\ C_{03} & C_{13} & C_{23}\end{bmatrix}\begin{bmatrix}Int^0\\ Int^1\\ Int^2\end{bmatrix}
\end{aligned}
$$

where

$$
\begin{aligned}
Int^0 &= \int_{-a}^{a}\ln[(x-\xi)^2+(y)^2]^{0.5}\,d\xi \\
Int^1 &= \int_{-a}^{a}\xi\ln[(x-\xi)^2+(y)^2]^{0.5}\,d\xi \qquad (2.9) \\
Int^2 &= \int_{-a}^{a}\xi^2\ln[(x-\xi)^2+(y)^2]^{0.5}\,d\xi
\end{aligned}
$$

The Int^0 , Int^1 , Int^2 are constant, linear and quadratic form kernels which are given as:

$$Int^0 = \int_{-a}^{a} \ln[(x-\xi)^2+(y)^2]^{0.5}d\xi = y(\Theta_1-\Theta_2)-(x-a)\ln\delta_1+(x+a)\ln\delta_2-2a$$

$$Int^1 = \int_{-a}^{a} \xi\ln[(x-\xi)^2+(y)^2]^{0.5}d\xi = xy(\Theta_1-\Theta_2)+0.5(y^2-x^2+a^2)(\ln\delta_1-\ln\delta_2)-ax$$

$$Int^2 = \int_{-a}^{a} \xi^2\ln[(x-\xi)^2+(y)^2]^{0.5}d\xi = {}^{y}\!/_{3}(3x^2-y^2)(\Theta_1-\Theta_2)+{}^{\ln\delta_1}\!/_{3}(3xy^2-x^3+a^3)$$
$$-{}^{\ln\delta_2}\!/_{3}(3xy^2-x^3-a^3)-{}^{2a}\!/_{3}(x^2-y^2+{}^{a^2}\!/_{3}) \tag{2.10}$$

in which,

$$\begin{aligned}\Theta_1 &= \arctan(y/(x-a))\\ \Theta_2 &= \arctan(y/(x+a))\\ \delta_1 &= \sqrt{(x-a)^2+y^2}\\ \delta_2 &= \sqrt{(x+a)^2+y^2}\end{aligned} \tag{2.11}$$

The derivatives of $f(x,y)$ and $g(x,y)$ that are used in Equation (2.5) are obtained by taking derivatives of Int^0, Int^1, Int^2. For example:

$$\begin{aligned}f(x,y)_{,x} &= F_2 = \frac{d(f(x,y))}{dx}\\ &= \frac{-1}{4\pi(1-v)}\left[(D_x)_1 \quad (D_x)_2 \quad (D_x)_3\right]\begin{bmatrix}C_{01} & C_{11} & C_{21}\\ C_{02} & C_{12} & C_{22}\\ C_{03} & C_{13} & C_{23}\end{bmatrix}\frac{d}{dx}\left(\begin{bmatrix}Int^0\\ Int^1\\ Int^2\end{bmatrix}\right)\\ &= \frac{-1}{4\pi(1-v)}\left[(D_x)_1 \quad (D_x)_2 \quad (D_x)_3\right]\begin{bmatrix}C_{01} & C_{11} & C_{21}\\ C_{02} & C_{12} & C_{22}\\ C_{03} & C_{13} & C_{23}\end{bmatrix}\begin{bmatrix}Int^0{}_{,x}\\ Int^1{}_{,x}\\ Int^2{}_{,x}\end{bmatrix}\end{aligned} \tag{2.12}$$

and,

$$g(x,y)_{,x}=G_2=\frac{d(g(x,y))}{dx}$$

$$=\frac{-1}{4\pi(1-v)}\begin{bmatrix}(D_y)_1 & (D_y)_2 & (D_y)_3\end{bmatrix}\begin{bmatrix}C_{01} & C_{11} & C_{21}\\ C_{02} & C_{12} & C_{22}\\ C_{03} & C_{13} & C_{23}\end{bmatrix}\frac{d}{dx}\left(\begin{bmatrix}Int^0\\ Int^1\\ Int^2\end{bmatrix}\right) \qquad (2.13)$$

$$=\frac{-1}{4\pi(1-v)}\begin{bmatrix}(D_y)_1 & (D_y)_2 & (D_y)_3\end{bmatrix}\begin{bmatrix}C_{01} & C_{11} & C_{21}\\ C_{02} & C_{12} & C_{22}\\ C_{03} & C_{13} & C_{23}\end{bmatrix}\begin{bmatrix}Int^0{}_{,x}\\ Int^1{}_{,x}\\ Int^2{}_{,x}\end{bmatrix}$$

Therefore, $f_{,xy}(F_4)$, $f_{,xx}(F_5)$, $f_{,xyy}(F_6)$, $f_{,yyy}(F_7)$, and $g_{,xy}(G_4)$, $g_{,xx}(G_5)$, $g_{,xyy}(G_6)$, $g_{,yyy}(G_7)$ can be obtained by computing $Int^0{}_{,x}$, $Int^0{}_{,y}$, $Int^0{}_{,xy}$, $Int^0{}_{,xx}$, $Int^0{}_{,xyy}$, $Int^0{}_{,yyy}$; $Int^1{}_{,x}$, $Int^1{}_{,y}$, $Int^1{}_{,xy}$, $Int^1{}_{,xx}$, $Int^1{}_{,xyy}$, $Int^1{}_{,yyy}$, $Int^2{}_{,x}$, $Int^2{}_{,y}$, $Int^2{}_{,xy}$, $Int^2{}_{,xx}$, $Int^2{}_{,xyy}$, $Int^2{}_{,yyy}$, which are given in Appendix A

Equations (2.7) are then substituted into Equation (2.5) for each segment of the discretized fractures to obtain the matrix format of HDDM by summing up from all the segments, which can be solved numerically for the displacement discontinuities.

2.2.3. Treatment on fracture tips

As previously mentioned, the displacement discontinuities are key factors in calculating the stress intensity factors (SIF) which govern the propagation of the fractures and the stresses around the crack tips. Another significant goal for HDDM is to predict accurate results around the fracture tips. For crack tip elements, there are not enough adjacent elements to form a three-element patch. Therefore, special treatments for the tip elements are required. Analytical solutions to crack problems show that the relative displacement between the crack surfaces is proportional to square root distribution (Rice, 1968). To maintain the accuracy of this HDDM, we adopt square root variation of the displacement discontinuity on the tip elements, which is defined as:

$$D_i(\xi) = \left(\xi/a\right)^{0.5} D_{ci} \tag{2.14}$$

where D_{ci} are the displacement discontinuity values at the center of the crack-tip elements.

Substituting Equation (2.14) into Equation (2.7) gives

$$f(x,y) = \frac{-1}{4\pi(1-v)} \int_{-a}^{a} \left(\xi/a\right)^{0.5} D_{ci} \ln[(x-\xi)^2 + (y)^2]^{0.5} d\xi \tag{2.15}$$

Rewriting the Equation (2.15):

$$\begin{aligned} f(x,y) &= \frac{-1}{4\pi(1-v)} \frac{1}{a^{0.5}} D_{ci} \int_{-a}^{a} \xi^{0.5} \ln[(x-\xi)^2 + (y)^2]^{0.5} d\xi \\ &= \frac{-1}{4\pi(1-v)} \frac{1}{a^{0.5}} Int^c \end{aligned} \tag{2.16}$$

where Int^c is computed and given as:

$$\begin{aligned} Int^c &= \int_{-a}^{a} \xi^{0.5} \ln[(x-\xi)^2 + (y)^2]^{0.5} d\xi \\ &= \frac{x^2+y^2}{2} A_1 - A_2 x \end{aligned} \tag{2.17}$$

The derivatives are given in the Appendix A.

2.2.4. Influencing coefficients and matrix assembly

The matrix assembly is based on the three-elements patch pattern to avoid introducing additional unknows and thus increasing the dimensions of the matrix. The three-element patch is shown in Figure 2.1. As shown in the figure, a_1, a_2 and a_3 are the half-lengths of the three elements, $(D_i)_1, (D_i)_2$, and $(D_i)_3$ are the corresponding nodal displacement discontinuities, respectively. In each patch of the three elements, three collocation points are used for shape functions, one at the center of the source element and others at the centers of the adjacent elements. For example, the $(D_x)_1, (D_x)_2$, and $(D_x)_3$ of the ith element patch are $(D_x)_{j-1}, (D_x)_j$, and $(D_x)_{j+1}$, respectively.

The shear and normal stresses at the midpoint of the ith element due to the displacement discontinuity components at the jth element patch is written as:

$$\begin{aligned}
\overset{i}{\sigma}_s &= \begin{bmatrix} \overset{i(j-1)}{A}_{ss} & \overset{ij}{A}_{ss} & \overset{i(j+1)}{A}_{ss} \end{bmatrix} \begin{bmatrix} \overset{j-1}{D}_s \\ \overset{j}{D}_s \\ \overset{j+1}{D}_s \end{bmatrix} + \begin{bmatrix} \overset{i(j-1)}{A}_{sn} & \overset{ij}{A}_{sn} & \overset{i(j+1)}{A}_{sn} \end{bmatrix} \begin{bmatrix} \overset{j-1}{D}_n \\ \overset{j}{D}_n \\ \overset{j+1}{D}_n \end{bmatrix} \\
\overset{i}{\sigma}_n &= \begin{bmatrix} \overset{i(j-1)}{A}_{ns} & \overset{ij}{A}_{ns} & \overset{i(j+1)}{A}_{ns} \end{bmatrix} \begin{bmatrix} \overset{j-1}{D}_s \\ \overset{j}{D}_s \\ \overset{j+1}{D}_s \end{bmatrix} + \begin{bmatrix} \overset{i(j-1)}{A}_{nn} & \overset{ij}{A}_{nn} & \overset{i(j+1)}{A}_{nn} \end{bmatrix} \begin{bmatrix} \overset{j-1}{D}_n \\ \overset{j}{D}_n \\ \overset{j+1}{D}_n \end{bmatrix}
\end{aligned} \qquad (2.18)$$

for $i = 1 \sim N$, where $\overset{ij}{A}_{ss}$, etc., are the boundary influence coefficients for the stress. Considering the patched elemental displacement discontinuity at each of the N segments for $j = 1 \sim N$ along the crack (Non-tip elements), we obtain the influence of all segments on ith element:

For tip elements, the equations are introduced in the previous section. The simpler treatment, for example, for one fracture, the tip elements are $j = 1, N$ (for multiple fractures, there are more tips between 1 and N). When $j=1$, $j-1=j_0$ is the additional introduced collocation point one-quarter of an element length away from the end of the crack, where $a_0=0.25a_1$ and $(D_i)_0=0$, similar treatment is conducted for $j=N$.

For each $\overset{j}{D}_s, j=1\sim N$, the coefficients for $\overset{i}{\sigma}_s$ are composed of three parts: $\overset{ik}{A}_{ss}, k=j$, $\overset{i(k-1)}{A}_{ss}, k=j+1$, and $\overset{i(k+1)}{A}_{ss}, k=j-1$.

The influencing coefficients in Equations (2.18) are developed from the analytical solution to the problem of a quadratic displacement discontinuity distribution over a three-element patch. Since the Equations are for local coordinates of the jth element patch, we need to transform the global coordinate x, y to local coordinates $\bar{x}, \bar{y}$, as shown in Figure 2.2. The equation is given by

$$\begin{aligned}\bar{x} &= (\overset{i}{x}-\overset{j}{x})\cos\overset{j}{\beta}+(\overset{i}{y}-\overset{j}{y})\sin\overset{j}{\beta}\\ \bar{y} &= -(\overset{i}{x}-\overset{j}{x})\sin\overset{j}{\beta}+(\overset{i}{y}-\overset{j}{y})\cos\overset{j}{\beta}\end{aligned} \tag{2.19}$$

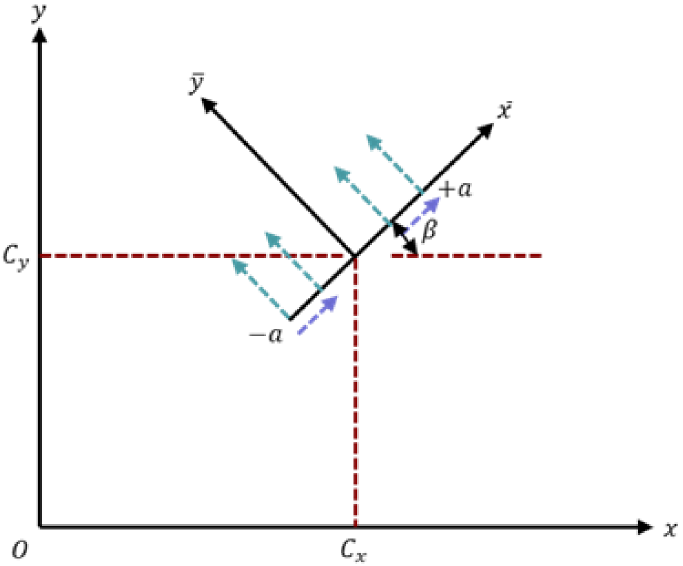

Figure 2.2 Demonstration of co-ordinates transformation for calculation of the DDM influencing coefficients.

The stresses of ith element due to displacement discontinuity components $D_{\bar{x}}$ and $D_{\bar{y}}$ over the jth element can be written as

$$\begin{aligned} \sigma_{\bar{x}\bar{y}} &= 2G\left[f_{,\bar{y}\bar{y}} + \bar{y} f_{,\bar{y}\bar{y}\bar{y}} \right] + 2G\left[-\bar{y} g_{,\bar{x}\bar{y}\bar{y}} \right] \\ \sigma_{\bar{y}\bar{y}} &= 2G\left[-\bar{y} f_{,\bar{x}\bar{y}\bar{y}} \right] + 2G\left[g_{,\bar{y}\bar{y}} - \bar{y} g_{,\bar{y}\bar{y}\bar{y}} \right] \end{aligned} \tag{2.20}$$

Through Equation (2.5) we can transform the stresses in local coordinate of the jth element to the local coordinate of ith element, which are expressed as:

$$\begin{aligned} \overset{i}{\sigma}_{\overline{x'y'}} &= 2G\left[-\sin 2\gamma \overline{F}_4 - \cos 2\gamma \overline{F}_5 - \bar{y}\left(\sin 2\gamma \overline{F}_6 - \cos 2\gamma \overline{F}_7 \right) \right] \\ &\quad + 2G\left[-\bar{y}\left(\cos 2\gamma \overline{G}_6 + \sin 2\gamma \overline{G}_7 \right) \right] \\ \overset{i}{\sigma}_{\overline{y'y'}} &= 2G\left[2\sin^2 \gamma \overline{F}_4 + 2\sin \gamma \overline{F}_5 - \bar{y}\left(\cos 2\gamma \overline{F}_6 + \sin 2\gamma \overline{F}_7 \right) \right] \\ &\quad + 2G\left[-\overline{G}_5 + \bar{y}\left(\sin 2\gamma \overline{G}_6 - \cos 2\gamma \overline{G}_7 \right) \right] \end{aligned} \tag{2.21}$$

where $\gamma = \overset{i}{\beta} - \overset{j}{\beta}$ gives the inclination of the ith element with reference to the jth element. Note that $\overset{j}{D}_{\bar{x}} = \overset{j}{D}_s, \overset{j}{D}_{\bar{y}} = \overset{j}{D}_n$ and $\overset{i}{\sigma}_{\overline{x'y'}} = \overset{i}{\sigma}_s, \overset{i}{\sigma}_{\overline{y'y'}} = \overset{i}{\sigma}_n$, we have the final equations for calculating the influencing coefficients in the numerical procedure:

$$\begin{aligned} \overset{i}{\sigma}_s &= 2G\left[-\sin 2\gamma \overline{F}_4 - \cos 2\gamma \overline{F}_5 - \bar{y}\left(\sin 2\gamma \overline{F}_6 - \cos 2\gamma \overline{F}_7 \right) \right] \\ &\quad + 2G\left[-\bar{y}\left(\cos 2\gamma \overline{G}_6 + \sin 2\gamma \overline{G}_7 \right) \right] \\ \overset{i}{\sigma}_n &= 2G\left[2\sin^2 \gamma \overline{F}_4 + 2\sin \gamma \overline{F}_5 - \bar{y}\left(\cos 2\gamma \overline{F}_6 + \sin 2\gamma \overline{F}_7 \right) \right] \\ &\quad + 2G\left[-\overline{G}_5 + \bar{y}\left(\sin 2\gamma \overline{G}_6 - \cos 2\gamma \overline{G}_7 \right) \right] \end{aligned} \tag{2.22}$$

Substituting Equations (2.12) and (2.13) into Equation (2.22) we can obtain:

$$
\begin{aligned}
\overset{i}{\sigma}_s = 2G & \left[-\sin 2\gamma \left[(D_x)_{j-1} \quad (D_x)_j \quad (D_x)_{j+1} \right] \begin{bmatrix} \overset{j}{\overline{IntC}}{}_{,4}^{1} \\ \overset{j}{\overline{IntC}}{}_{,4}^{2} \\ \overset{j}{\overline{IntC}}{}_{,4}^{3} \end{bmatrix} - \cos 2\gamma \left[(D_x)_{j-1} \quad (D_x)_j \quad (D_x)_{j+1} \right] \begin{bmatrix} \overset{j}{\overline{IntC}}{}_{,5}^{1} \\ \overset{j}{\overline{IntC}}{}_{,5}^{2} \\ \overset{j}{\overline{IntC}}{}_{,5}^{3} \end{bmatrix} \right. \\
& \left. -\bar{y} \left(\sin 2\gamma \left[(D_x)_{j-1} \quad (D_x)_j \quad (D_x)_{j+1} \right] \begin{bmatrix} \overset{j}{\overline{IntC}}{}_{,6}^{1} \\ \overset{j}{\overline{IntC}}{}_{,6}^{2} \\ \overset{j}{\overline{IntC}}{}_{,6}^{3} \end{bmatrix} - \cos 2\gamma \left[(D_x)_{j-1} \quad (D_x)_j \quad (D_x)_{j+1} \right] \begin{bmatrix} \overset{j}{\overline{IntC}}{}_{,7}^{1} \\ \overset{j}{\overline{IntC}}{}_{,7}^{2} \\ \overset{j}{\overline{IntC}}{}_{,7}^{3} \end{bmatrix} \right) \right] \\
+ 2G & \left[-\bar{y} \left(\cos 2\gamma \left[(D_y)_{j-1} \quad (D_y)_j \quad (D_y)_{j+1} \right] \begin{bmatrix} \overset{j1}{\overline{IntC}}{}_{,6}^{0} \\ \overset{j2}{\overline{IntC}}{}_{,6}^{1} \\ \overset{j3}{\overline{IntC}}{}_{,6}^{2} \end{bmatrix} + \sin 2\gamma \left[(D_y)_{j-1} \quad (D_y)_j \quad (D_y)_{j+1} \right] \begin{bmatrix} \overset{j1}{\overline{IntC}}{}_{,7}^{0} \\ \overset{j2}{\overline{IntC}}{}_{,7}^{1} \\ \overset{j3}{\overline{IntC}}{}_{,7}^{2} \end{bmatrix} \right) \right]
\end{aligned}
$$

(2.23)

Now the influencing coefficients for jth element can be expressed as:

$$\overset{i(j-1)}{A}_{ss} = 2G\left[-\sin 2\gamma\,\overset{j1}{\overline{IntC}}{}_{,4}^{0} - \cos 2\gamma\,\overset{j1}{\overline{IntC}}{}_{,5}^{0} - \bar{y}\left(\sin 2\gamma\,\overset{j1}{\overline{IntC}}{}_{,6}^{0} - \cos 2\gamma\,\overset{j1}{\overline{IntC}}{}_{,7}^{0}\right)\right]$$

$$\overset{ij}{A}_{ss} = 2G\left[-\sin 2\gamma\,\overset{j1}{\overline{IntC}}{}_{,4}^{1} - \cos 2\gamma\,\overset{j1}{\overline{IntC}}{}_{,5}^{1} - \bar{y}\left(\sin 2\gamma\,\overset{j1}{\overline{IntC}}{}_{,6}^{1} - \cos 2\gamma\,\overset{j1}{\overline{IntC}}{}_{,7}^{1}\right)\right]$$

$$\overset{i(j+1)}{A}_{ss} = 2G\left[-\sin 2\gamma\,\overset{j1}{\overline{IntC}}{}_{,4}^{2} - \cos 2\gamma\,\overset{j1}{\overline{IntC}}{}_{,5}^{2} - \bar{y}\left(\sin 2\gamma\,\overset{j1}{\overline{IntC}}{}_{,6}^{2} - \cos 2\gamma\,\overset{j1}{\overline{IntC}}{}_{,7}^{2}\right)\right]$$

(2.24)

For $(j-1)th$ element

$$\overset{i(j-2)}{A}_{ss} = 2G\left[-\sin 2\gamma\,\overset{(j-1)2}{\overline{IntC}}{}_{,4}^{0} - \cos 2\gamma\,\overset{(j-1)2}{\overline{IntC}}{}_{,5}^{0} - \bar{y}\left(\sin 2\gamma\,\overset{(j-1)2}{\overline{IntC}}{}_{,6}^{0} - \cos 2\gamma\,\overset{(j-1)2}{\overline{IntC}}{}_{,7}^{0}\right)\right]$$

$$\overset{i(j-1)}{A}_{ss} = 2G\left[-\sin 2\gamma\,\overset{(j-1)2}{\overline{IntC}}{}_{,4}^{1} - \cos 2\gamma\,\overset{(j-1)2}{\overline{IntC}}{}_{,5}^{1} - \bar{y}\left(\sin 2\gamma\,\overset{(j-1)2}{\overline{IntC}}{}_{,6}^{1} - \cos 2\gamma\,\overset{(j-1)2}{\overline{IntC}}{}_{,7}^{1}\right)\right]$$

$$\overset{ij}{A}_{ss} = 2G\left[-\sin 2\gamma\,\overset{(j-1)2}{\overline{IntC}}{}_{,4}^{2} - \cos 2\gamma\,\overset{(j-1)2}{\overline{IntC}}{}_{,5}^{2} - \bar{y}\left(\sin 2\gamma\,\overset{(j-1)2}{\overline{IntC}}{}_{,6}^{2} - \cos 2\gamma\,\overset{(j-1)2}{\overline{IntC}}{}_{,7}^{2}\right)\right]$$

(2.25)

For $(j+1)th$ element

$$\overset{ij}{A}_{ss} = 2G\left[-\sin 2\gamma\,\overset{(j+1)0}{\overline{IntC}}{}_{,4}^{0} - \cos 2\gamma\,\overset{(j+1)0}{\overline{IntC}}{}_{,5}^{0} - \bar{y}\left(\sin 2\gamma\,\overset{(j+1)0}{\overline{IntC}}{}_{,6}^{0} - \cos 2\gamma\,\overset{(j+1)0}{\overline{IntC}}{}_{,7}^{0}\right)\right]$$

$$\overset{i(j+1)}{A}_{ss} = 2G\left[-\sin 2\gamma\,\overset{(j+1)0}{\overline{IntC}}{}_{,4}^{1} - \cos 2\gamma\,\overset{(j+1)0}{\overline{IntC}}{}_{,5}^{1} - \bar{y}\left(\sin 2\gamma\,\overset{(j+1)0}{\overline{IntC}}{}_{,6}^{1} - \cos 2\gamma\,\overset{(j+1)0}{\overline{IntC}}{}_{,7}^{1}\right)\right]$$

$$\overset{i(j+2)}{A}_{ss} = 2G\left[-\sin 2\gamma\,\overset{(j+1)0}{\overline{IntC}}{}_{,4}^{2} - \cos 2\gamma\,\overset{(j+1)0}{\overline{IntC}}{}_{,5}^{2} - \bar{y}\left(\sin 2\gamma\,\overset{(j+1)0}{\overline{IntC}}{}_{,6}^{2} - \cos 2\gamma\,\overset{(j+1)0}{\overline{IntC}}{}_{,7}^{2}\right)\right]$$

(2.26)

The total influencing coefficient of the shear displacement discontinuity of jth element on the shear stress of ith element is then expressed as

$$\begin{aligned}
\overset{ij}{A}_{ss}(total) = {} & 2G\left[-\sin 2\gamma\, \overset{(j+1)0}{\overline{IntC}}{}_{,4}^{\,0} - \cos 2\gamma\, \overset{(j+1)0}{\overline{IntC}}{}_{,5}^{\,0} - \bar{y}\left(\sin 2\gamma\, \overset{(j+1)0}{\overline{IntC}}{}_{,6}^{\,0} - \cos 2\gamma\, \overset{(j+1)0}{\overline{IntC}}{}_{,7}^{\,0}\right)\right] \\
& +2G\left[-\sin 2\gamma\, \overset{j1}{\overline{IntC}}{}_{,4}^{\,1} - \cos 2\gamma\, \overset{j1}{\overline{IntC}}{}_{,5}^{\,1} - \bar{y}\left(\sin 2\gamma\, \overset{j1}{\overline{IntC}}{}_{,6}^{\,1} - \cos 2\gamma\, \overset{j1}{\overline{IntC}}{}_{,7}^{\,1}\right)\right] \qquad (2.27) \\
& +2G\left[-\sin 2\gamma\, \overset{(j-1)2}{\overline{IntC}}{}_{,4}^{\,2} - \cos 2\gamma\, \overset{(j-1)2}{\overline{IntC}}{}_{,5}^{\,2} - \bar{y}\left(\sin 2\gamma\, \overset{(j-1)2}{\overline{IntC}}{}_{,6}^{\,2} - \cos 2\gamma\, \overset{(j-1)2}{\overline{IntC}}{}_{,7}^{\,2}\right)\right]
\end{aligned}$$

Similarly, we can obtain the expressions for A_{sn} , A_{ns} and A_{nn}

2.3. Joint-element higher order displacement discontinuity method

For computational purposes, a segment of joint can be introduced and modeled as an elemental displacement discontinuity whose opposite surfaces are connected by a spring, with the normal and shear stiffness of the spring chosen to be representative of the properties of the joint-filling material (as shown in Figure 2.3, Crouch and Starfield, 1983). The values of the displacement discontinuity components are related to the normal and shear stresses acting on the joint element. A joint element can have three different types of contact mode: stick, shear, and open modes, as shown in Figure 2.4. A joint with different modes has its unique control equations between the displacement discontinuities and the stresses.

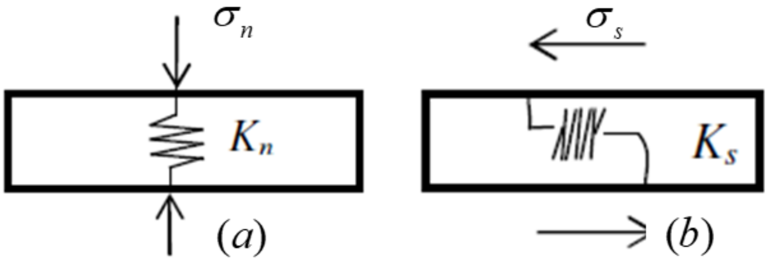

Figure 2.3 Demonstration of the spring-like joint elements (Crouch and Starfield 1983).

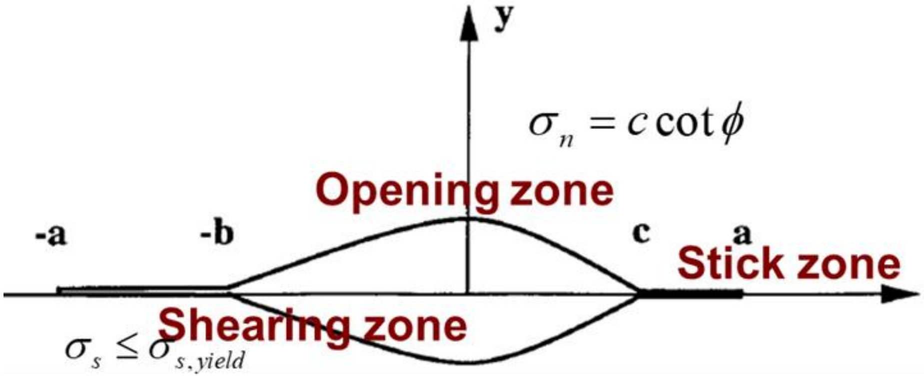

Figure 2.4 Demonstration of the three types of the contact mode of a joint element: opening model, shearing mode and the stick mode, with the corresponding criteria.

In the close-spacing multi-fracture problem where the CDDM gives negative values of the opening width for the inner fractures due to the strong stress shadowing effect, which are physically impossible, joint elements successfully help DDM avoid the negative openings by assigning the stick contact type. The joint stick mode has the assumption that the element of interest has reached the equilibrium with in-situ stress and is closed. The element does not deform elastically under the combined influence of net pressure from hydraulic fracturing and the stress shadowing effect from outer fractures, whose control equation between the stresses and displacement discontinuities are shown in Equation (2.28).

$$
\begin{aligned}
0 &= \sum_{j=1}^{N}\left(\overset{ij}{A}_{ss}\,\overset{j}{D}{}'_{s}+\overset{ij}{A}_{sn}\,\overset{j}{D}{}'_{n}\right)+\left(\overset{i}{K}_{s}\right)\left(\overset{i}{D}{}'_{s}\right)\\
0 &= \sum_{j=1}^{N}\left(\overset{ij}{A}_{ns}\,\overset{j}{D}{}'_{s}+\overset{ij}{A}_{nn}\,\overset{j}{D}{}'_{n}\right)+\left(\overset{i}{K}_{n}\right)\left(\overset{i}{D}{}'_{n}\right)
\end{aligned}
\qquad (2.28)
$$

where N is the total number of elements, $\overset{ij}{A}_{ss}, \overset{ij}{A}_{sn}, \overset{ij}{A}_{ns}, \overset{ij}{A}_{nn}$ are the influencing coefficients, $D_n{}'$ and $D_s{}'$ are the induced normal and shear displacement discontinuities, K_n and K_s are the normal and shear rigidity.

The joint shear mode occurs when the total shear stress across the joint element exceeds the total yield stress, as indicated by Equation (2.29):

$$
\left|\sigma_s^i\right| \geq \sigma_{s,yield}^{i} = \tan\overset{i}{\phi}\,\sigma_n^i + \overset{i}{c} \qquad (2.29)
$$

The governing equation is given by:

$$
\begin{aligned}
-\left(\overset{i}{\sigma}_{s}\right)_{0} &= \sum_{j=1}^{N}\left(\overset{ij}{A}_{ss}\,\overset{j}{D}{}'_{s}+\overset{ij}{A}_{sn}\,\overset{j}{D}{}'_{n}\right)\mp\sigma_{yield}^{i}\\
-\left(\overset{i}{\sigma}_{n}\right)_{0} &= \sum_{j=1}^{N}\left(\overset{ij}{A}_{ns}\,\overset{j}{D}{}'_{s}+\overset{ij}{A}_{nn}\,\overset{j}{D}{}'_{n}\right)+\left(\overset{i}{K}_{n}\right)\left(\overset{i}{D}{}'_{n}\right)
\end{aligned}
\qquad (2.30)
$$

where $\left(\sigma_n\right)_0$ and $\left(\sigma_s\right)_0$ are the remote normal and shear stresses, σ_{yield}^{i} is the yield stress on i element.

The joint open mode, or separation mode, means the two surfaces of the joint element are separated from each other, which is identical to the phenomenon of fracture opening. This mode occurs when the tensile stress across an element is larger than the tensile strength. In hydraulic fracturing problems, the equation for joint open mode is identical to the original DDM form, whose discrete matrix form is expressed in Equation (2.31). The equations and the corresponding criteria for those three contact types are elaborated in Crouch and Starfield (1983) and will not be repeatedly here.

$$\begin{aligned} \left(\sigma_s^i\right)^{ind} &= \sum_{j=1}^{N}\left(A_{ss}^{ij} D_s^{j'} + A_{sn}^{ij} D_n^{j'}\right) \\ \left(\sigma_n^i\right)^{ind} &= \sum_{j=1}^{N}\left(A_{ns}^{ij} D_s^{j'} + A_{nn}^{ij} D_n^{j'}\right) \end{aligned} \tag{2.31}$$

where $(\sigma_n)^{ind}$ and $(\sigma_s)^{ind}$ are the induced normal and shear stresses.

For fracture problems involving joint elements, the contact type (stick, shear or open) and the corresponding displacement discontinuities/stresses of each element along the joint are unknown, but they can be solved simultaneously and iteratively until the convergence of the contact modes. We developed a workflow incorporating the joint element into the HDDM which can be summarized as following (Figure 2.5): the initial contact modes of the discretized fracture elements are assumed, where a very good assumption is based on the HDDM results, i.e., elements with positive opening width are assumed open mode while elements with negative opening width are assumed stick mode; therefore the opening, shearing, and sticking equations (anyone or combination) can be solved simultaneously to obtain the normal and shear displacement discontinuities. Then the total normal and shear stress states can be obtained from the induced displacement discontinuities by Equation (2.32) and used to check the contact types. If the contact type for all the fracture segments agree with the given ones, the converged results are obtained.

Otherwise, the new contact type of the elements computed from the stress states will be the used as assumption for next iteration, until the contact type of all the elements converge.

$$\begin{aligned}\left(\overset{i}{\sigma}_s\right)_{total} &= \left(\overset{i}{\sigma}_s\right)_0 + \sum_{j=1}^{N}\left(\overset{ij}{A}_{ss}\,\overset{j}{D}{}_s^{'} + \overset{ij}{A}_{sn}\,\overset{j}{D}{}_n^{'}\right)\\ \left(\overset{i}{\sigma}_n\right)_{total} &= \left(\overset{i}{\sigma}_n\right)_0 + \sum_{j=1}^{N}\left(\overset{ij}{A}_{ns}\,\overset{j}{D}{}_s^{'} + \overset{ij}{A}_{nn}\,\overset{j}{D}{}_n^{'}\right)\end{aligned} \tag{2.32}$$

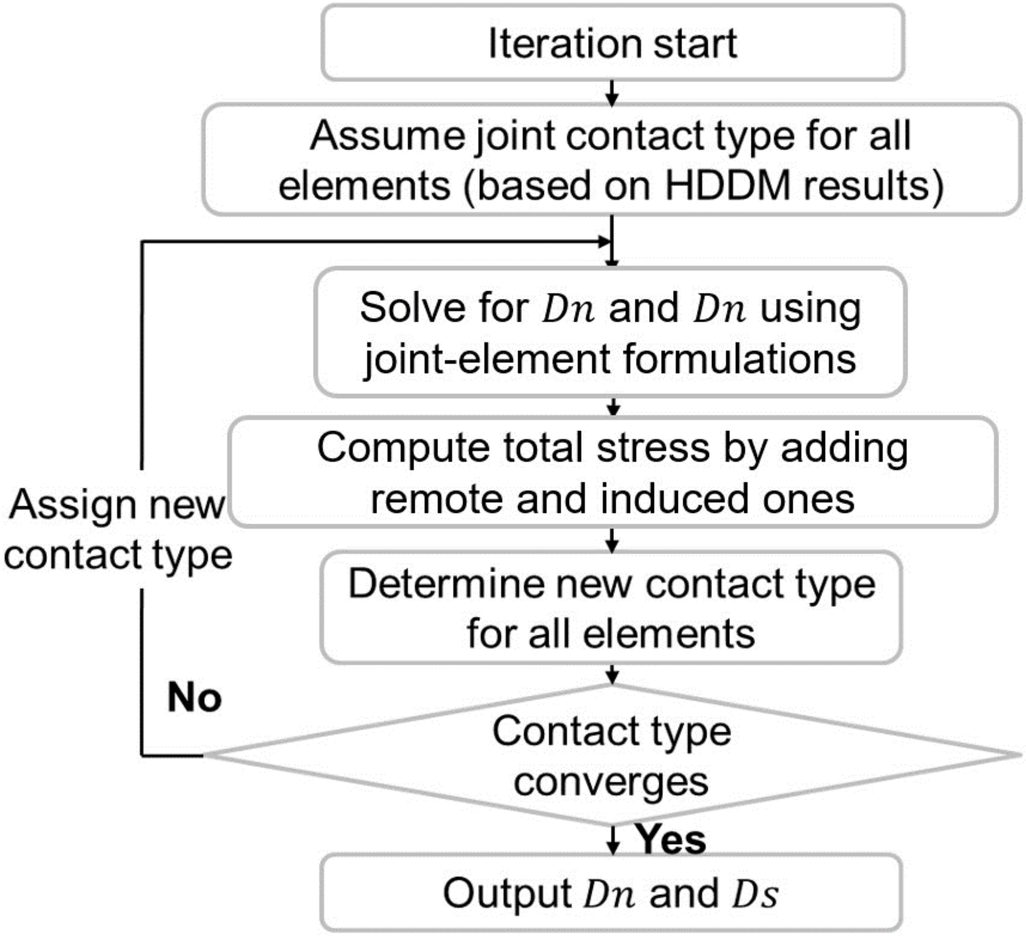

Figure 2.5 Iteration workflow for determining the contact type of the fracture elements and the displacement discontinuities in JE-HDDM.

2.4. Verification

The newly developed JE-HDDM was designated for the two-dimensional close-spacing multi-fracture problem where the CDDM loses accuracy or stability. However, for relatively large spacing fracture cases, the JE-HDDM should have the same results with the CDDM. Therefore, an example case with four uniform bi-wing fractures whose half lengths are 100 meters and spacing is 30 meters was investigated for verification. The fluid pressure is assumed constant inside the fracture and the net normal and shear stresses in the internal boundary are 2 MPa and 0, respectively. The normal and shear rigidity for the joint element is set to be 50 GPa/m and 25 GPa/m. Experiments results (Ye et al. 2016) show that under the confining pressure of thousands of psi, the stiffness values of fractures in shale formations display highly linear properties and the yield stress of the fracture element is much larger than the in-situ stress of the formation. The typical stiffness values (normal and shear) vary from tens to hundreds of GPa/m. The Young's modulus is 45 GPa, and the Poisson's ratio is 0.25.

Since the fracture is uniform and the spacing is identical, the four fractures can be grouped into two inner fractures and two outer fractures, whose results should be the same in each group. Figure 2.6 and Figure 2.7 presented the comparison of normal and shear displacement discontinuities of the outer fracture (F1) and the inner fracture (F2) between the JE-HDDM and CDDM. Both methods use the same length of element, which is 10 meters and the same number of fracture elements, which is 80 in total. From Figure 2.6 and Figure 2.7, it is observed that the JE-HDDM has a good agreement with CDDM in both DN and DS results except around the tips of the fractures. This difference is caused by the deficiency of CDDM due to the assumption of constant values at the tips and the improvement of HDDM by special tip treatment as introduced in the section 2. Detailed discussion with regard to the accuracy will be explained in next sections. In large-spacing cases such that fractures do not have negative width, the numerical workflow of the joint element converges at the first iteration, which is the same results as the CDDM.

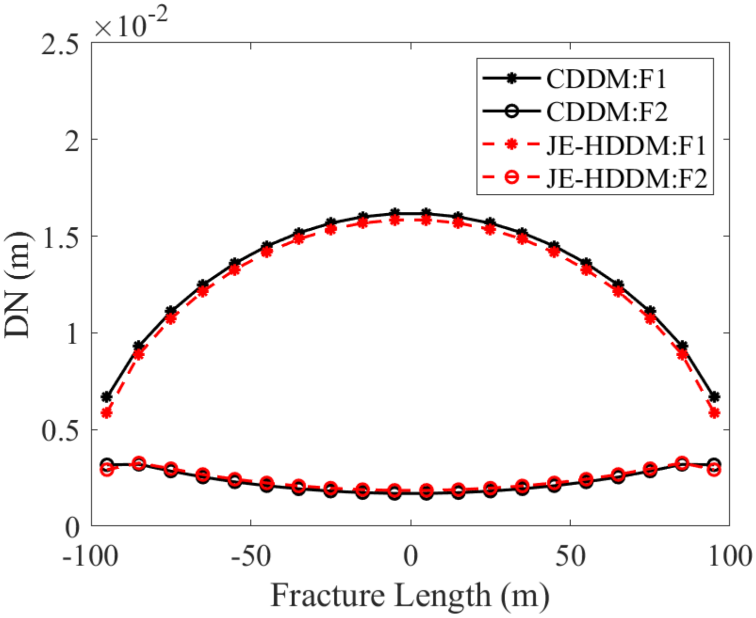

Figure 2.6 Validation of JE-HDDM against CDDM in terms of normal displacement discontinuities for the outer fracture (F1) and the inner fracture (F2) using 4 fracture case (half-length = 300 m, spacing = 30 m). (Reprinted from Li et al 2022)

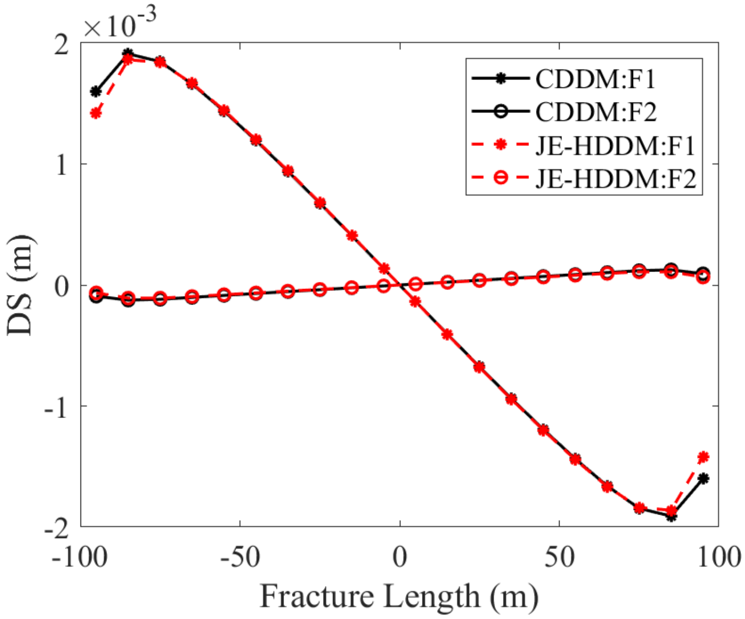

Figure 2.7 Validation of JE-HDDM against CDDM in terms of shear displacement discontinuities for the outer fracture (F1) and the inner fracture (F2) using 4 fracture case (half-length = 300 m, spacing = 30 m). (Reprinted from Li et al 2022)

2.5. Application to close-spacing planar fracture analysis

To test the outperformance of the JE-HDDM over the CDDM in accuracy as well as efficiency in dealing with close-spacing fractures, a two-dimensional base case (Figure 2.8) with eight bi-wing close-spacing fractures is studied. The fracture half-length is 300 meters along the y axis and the fracture spacing is 10 meters. The fluid pressure is assumed constant inside the fracture and the net normal and shear stresses in the internal boundary are 2 MPa and 0, respectively. The normal and shear rigidity for the joint element is set to be 50 GPa/m and 25 GPa/m for all elements. As shown in Figure 2.8, eight black lines represent the eight fractures and the red lines are locations where we are investigating the induced stresses in the following sections.

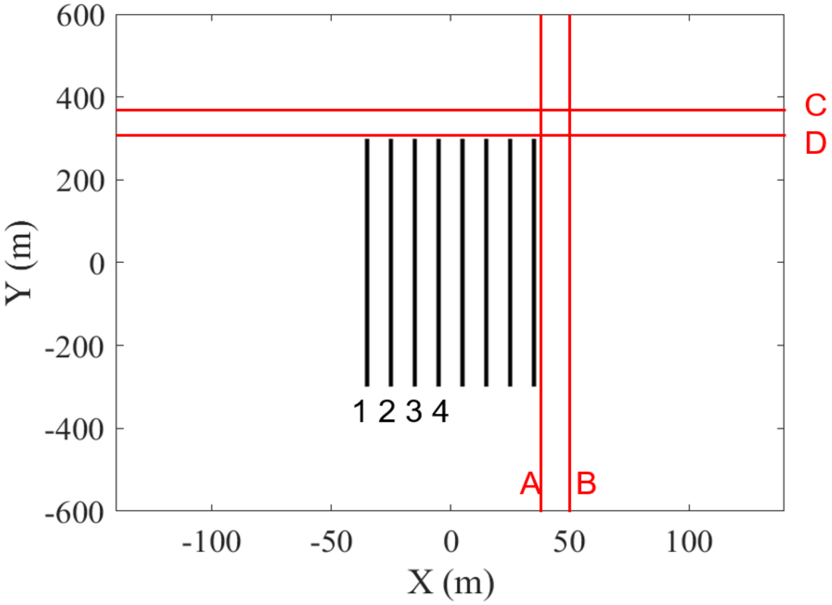

Figure 2.8 Illustration of eight bi-wing fracture problem with 10 m spacing and 300 m half length. (Reprinted from Li et al 2022)

2.5.1. Displacement discontinuities

One of the most concerning parameters in the fracture problems is the fracture width, which is the value of normal displacement discontinuity. In this section we demonstrated the outperformance of the JE-HDDM over the CDDM in accuracy as well as efficiency in calculating displacement discontinuities.

Due to the symmetry of the eight bi-wing fracture problem, only four fractures' results are presented and the rest four have the same values. Figure 2.9-Figure 2.12 compare the normal displacement discontinuity results of the four fractures indicated in Figure 2.8 between the CDDM, HDDM and JE-HDDM using different element lengths (EL). As observed from black-asterisk lines of these four figures, CDDM with element length 10 m (i.e. 480 elements in total) predicts inaccurate and physically unreasonable results for all four fractures. This is attributed to the strong stress shadowing effect by close-spacing and large half-length fractures. The wavy behavior of the displacement discontinuity distributions along the fractures are due to the incompetence of the CDDM to give physically accurate results to such problem. Although the wavy results mathematically satisfy the given boundary conditions, they are physically unreliable since the width of a fracture cannot be negative and cannot show the wavy behavior under the constant boundary conditions. When using element length of 1 m (i.e. total 4800 computational elements) as shown by the black lines, CDDM is able to predict physically reliable results. However, from the black curves in Figure 2.9-Figure 2.12, it is noticed that negative opening width of the fractures were given by the CDDM for inner fractures, which is physically impossible. The HDDM results with different element lengths are presented in the red curves. It is observed that the HDDM gives stable results with both coarse element (EL = 10 m) and fine element (EL = 1 m) and the results are the same with the CDDM using the fine element. However, the HDDM is not able to avoid the negative width of the inner fractures, as shown in Figure 2.9, 2.10, 2.11, and 2.12. In contrast, as shown by the two blue curves, the JE-HDDM demonstrated the accuracy and stability for both element lengths of 10 m and 1 m, which indicates the outperformance of higher order approximation of displacement discontinuities over constant assumption. In fracture segments where the CDDM and HDDM predict negative widths, these segments may be mechanically closed due to the strong stress shadowing effect induced by the outer fractures. In such condition, the JE-HDDM assigned stick-mode to the joint elements and re-calculate the displacement discontinuity distributions of all elements until the convergence of contact type of all elements, which eliminates the negative opening widths for the mechanically closed fracture segments.

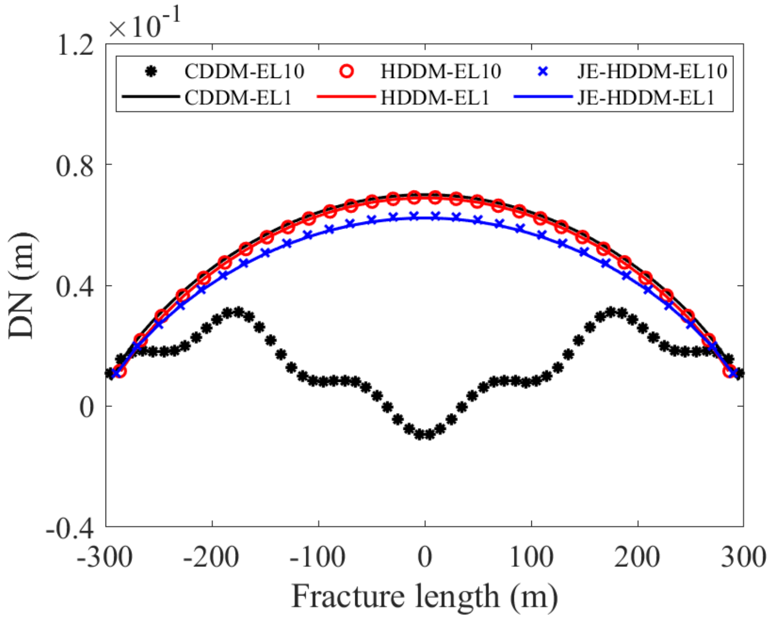

Figure 2.9 Comparison of normal displacement discontinuities (DN) of fracture 1 between CDDM, HDDM and JE-HDDM using different element lengths (EL = 10 m, 1 m). (Reprinted from Li et al 2022)

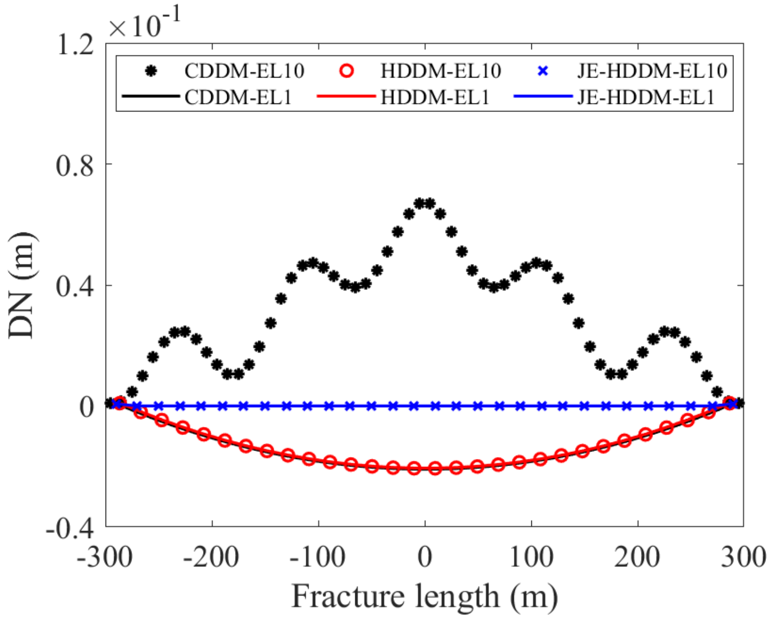

Figure 2.10 Comparison of normal displacement discontinuities (DN) of fracture 2 between CDDM, HDDM and JE-HDDM using different element lengths (EL = 10 m, 1 m). (Reprinted from Li et al 2022)

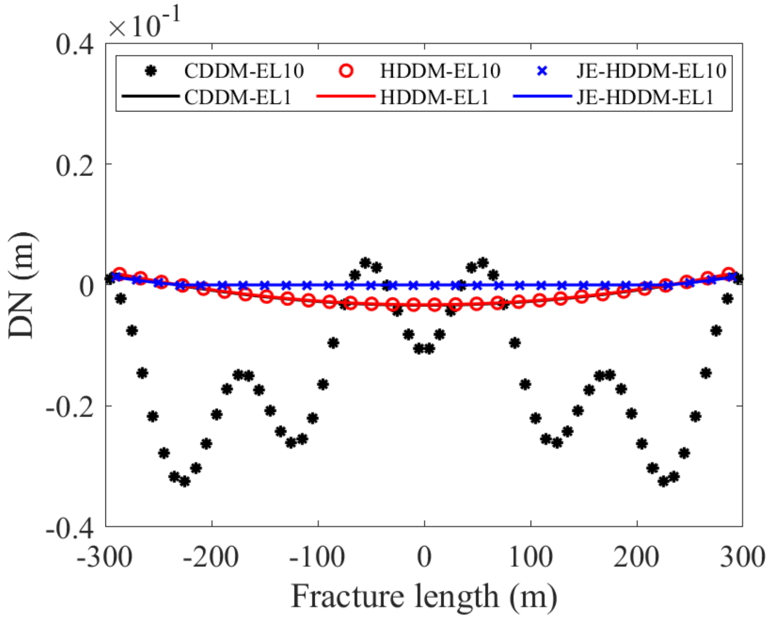

Figure 2.11 Comparison of normal displacement discontinuities (DN) of fracture 3 between CDDM, HDDM and JE-HDDM using different element lengths (EL = 10 m, 1 m). (Reprinted from Li et al 2022)

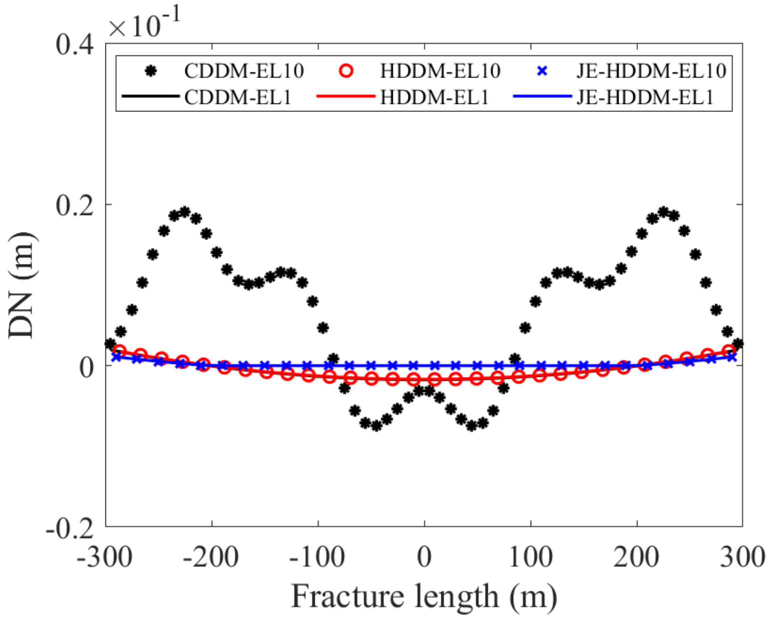

Figure 2.12 Comparison of normal displacement discontinuities (DN) of fracture 4 between CDDM, HDDM and JE-HDDM using different element lengths (EL = 10 m, 1 m). (Reprinted from Li et al 2022)

Figure 2.13-2.16 show the comparison of the shear displacement discontinuity of the four fractures indicated in Figure 2.8 using the CDDM, HDDM and JE-HDDM with different element lengths (EL). It is found that JE-HDDM and HDDM always demonstrate stability and high accuracy for all four fractures. Results with element length 10 m or 1 m have minor difference between each other. For CDDM, simulation results of the 10 m element length are again inaccurate (as indicated by the black- asterisk lines), as same as the normal displacement discontinuity results, while simulation results of the 1 m element length have a good agreement with the JE-HDDM results (as indicated by the black lines). It is to be noted that in Figure 2.15 and Figure 2.16, the results given by the CDDM with 10 m element length are multiplied by 0.01 because the inaccurate values are much larger than the accurate results.

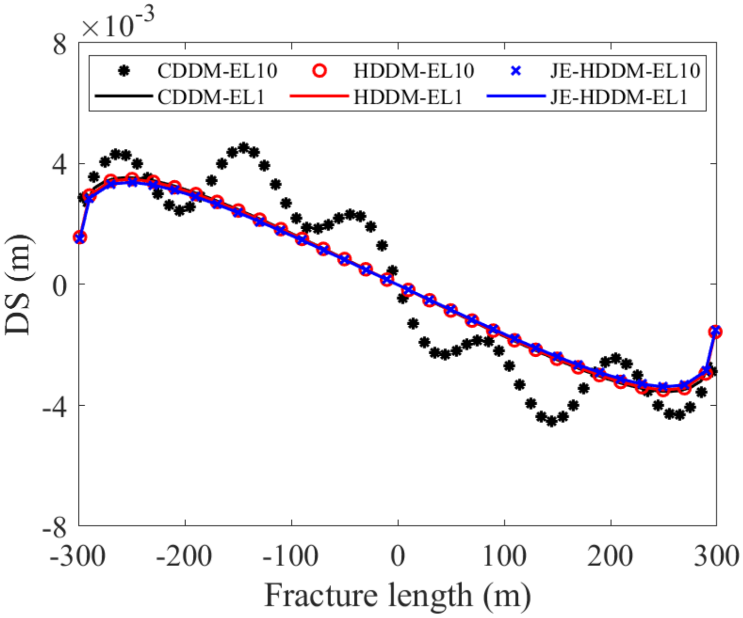

Figure 2.13 Comparison of shear displacement discontinuities (DS) of fracture 1 between CDDM, HDDM and JE-HDDM using different element lengths (EL = 10 m, 1 m). (Reprinted from Li et al 2022)

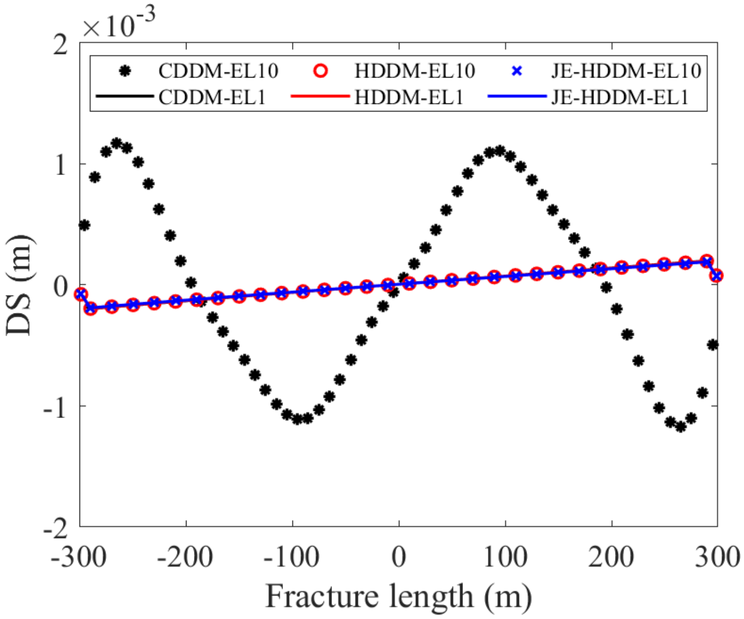

Figure 2.14 Comparison of shear displacement discontinuities (DS) of fracture 2 between CDDM, HDDM and JE-HDDM using different element lengths (EL = 10 m, 1 m). (Reprinted from Li et al 2022)

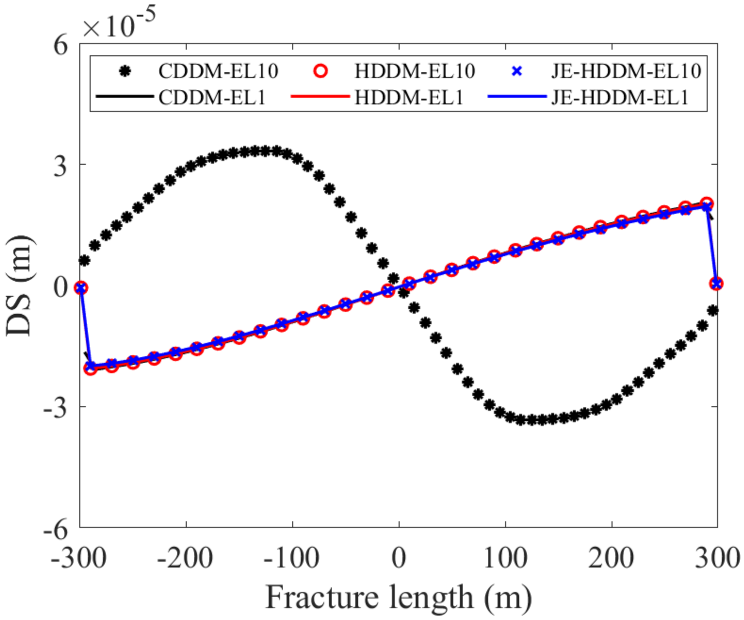

Figure 2.15 Comparison of shear displacement discontinuities (DS) of fracture 3 between CDDM, HDDM and JE-HDDM using different element lengths (EL = 10 m, 1 m). (Reprinted from Li et al 2022)

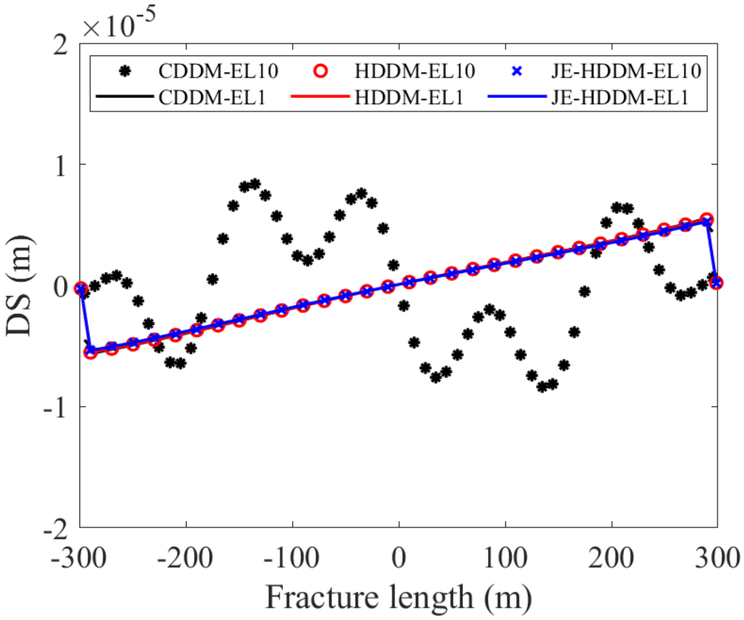

Figure 2.16 Comparison of shear displacement discontinuities (DS) of fracture 4 between CDDM, HDDM and JE-HDDM using different element lengths (EL = 10 m, 1 m). (Reprinted from Li et al 2022)

It is also indicated from Figure 2.9-2.16 that the JE-HDDM has a high computational efficiency since the results of 10 m element length coincided with the results of 1 m element length, which means that compared with CDDM, JE-HDDM can use a larger element length to achieve accurate results by reducing a large amount of computational time.

To demonstrate the higher efficiency and high accuracy of the JE-HDDM, we conducted a series of simulations using the JE-HDDM and JE-CDDM for eight fractures with different spacing and obtained the allowed-maximum element length and the corresponding simulation time for the two methods to give an engineering acceptable results whose average relative error is less than 10%. The allowed-maximum element length and the corresponding total simulation time are listed in Table 2.1 and Table 2.2 and are depicted in Figure 2.17. The average relative error is compared against the results given by JE-HDDM using element length 1 m, which are 600 elements for each fracture and 4800 elements in total.

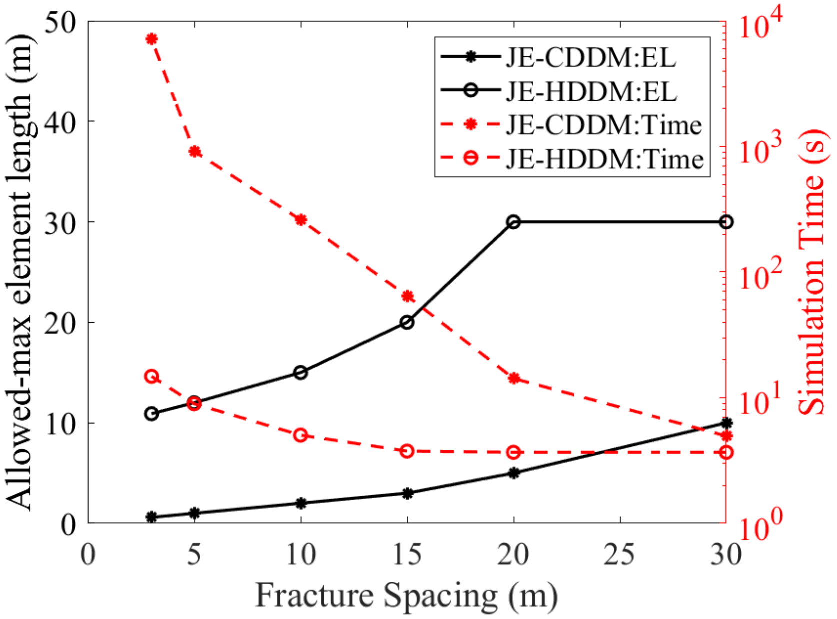

Figure 2.17 Comparison between JE-HDDM and JE-CDDM in terms of the allowed-maximum element length (EL, m) and the corresponding simulation time (second) for results with less than 10% DN and DS relative error for eight-fracture cases with different fracture spacings (meter). (Reprinted from Li et al 2022)

Table 2.1 Allowed-maximum element length and simulation time to obtain engineering acceptable results (relative error < 10%) by JE-CDDM and JE-HDDM for eight fractures with different fracture spacings. (Reprinted from Li et al 2022)

Fracture spacing (m)		30	20	15	10	5	3
Allowed-maximum element length (m)	JE-CDDM	10	5	3	2	1	0.6
	JE-HDDM	30	30	20	15	12	11
Simulation time (s)	JE-CDDM	4.98	14.24	67.42	260.39	911.67	7153
	JE-HDDM	3.68	3.68	3.78	5.14	9.11	14.82

Table 2.2 Average relative error of normal displacement discontinuity computed by CDDM using different element sizes under different fracture spacing cases compared with fine grid HDDM results. (Reprinted from Li et al 2022)

Fracture spacing (m) / Element size (m)	30		20		10	
	CDDM	HDDM	CDDM	HDDM	CDDM	HDDM
30	unstable	1.01%	Unstable	1.81%	unstable	4.88%
20	14.29%	0.08%	>100%	0.12%	unstable	0.98%
10	3.66%	<0.01%	52.13%	0.02%	unstable	0.05%
5	0.79%	accurate	9.04%	0.01%	24.28%	<0.01%
1	<0.01%	accurate	0.79%	accurate	5.49%	accurate

As shown from Figure 2.17, the JE-HDDM provides engineering acceptable results using relatively large element lengths (above 10 meters), while in contrast, the JE-CDDM requires much finer elements (element length less than 1 meter) to obtain accurate results due to the limitation of the constant-element assumption, especially for the cases with close fracture spacing. Meanwhile, large computational effort must be made to achieve the accurate results through fine grids simulation. Figure 2.17 demonstrates the outperformance in accuracy and efficiency of the JE-HDDM. In field scale geo-mechanical problems, such as hydraulic fracturing modeling, the JE-HDDM far outperforms the CDDM since much fewer numbers of elements are required to obtain accurate results.

2.5.2. Induced stresses

The induced stresses by hydraulic fractures is another important factor for hydraulic fracturing problems. In this section we investigated and demonstrated the outperformance of the JE-HDDM in terms of the induced stress profiles. The induced stress profiles were calculated using the HDDM and CDDM, based on results of the normal and shear displacement discontinuities given by the JE-HDDM and JE-CDDM, respectively.

Figure 2.18-2.21 depict the induced Sxx and Sxy stress profiles given by JE-HDDM and JE-CDDM using different element lengths along the fractures in different locations A and B as indicated in Figure 2.8. Three element lengths are used for both methods to calculate the results. For JE-HDDM, only simulation results of 10 m element length are presented since results of the other two element lengths are coincided due to high accuracy of JE-HDDM. It is observed from the figures that JE-HDDM always maintains high accuracy with large element length (10 m) near the fractures, while JE-CDDM is only accurate with small element length (1 m) in calculating stress far away from the fractures. For example, Figure 2.20 and Figure 2.21 show that along location B, JE-CDDM gives accurate results with small element lengths (1 m and 5 m) and has observable errors with the large element length (10 m) while JE-HDDM is always accurate with different element lengths. In Figure 2.18 and Figure 2.20 showing results in near fracture area (location A), JE-CDDM is only accurate with 1 m element length while JE-HDDM can give accurate results with 10 m element length.

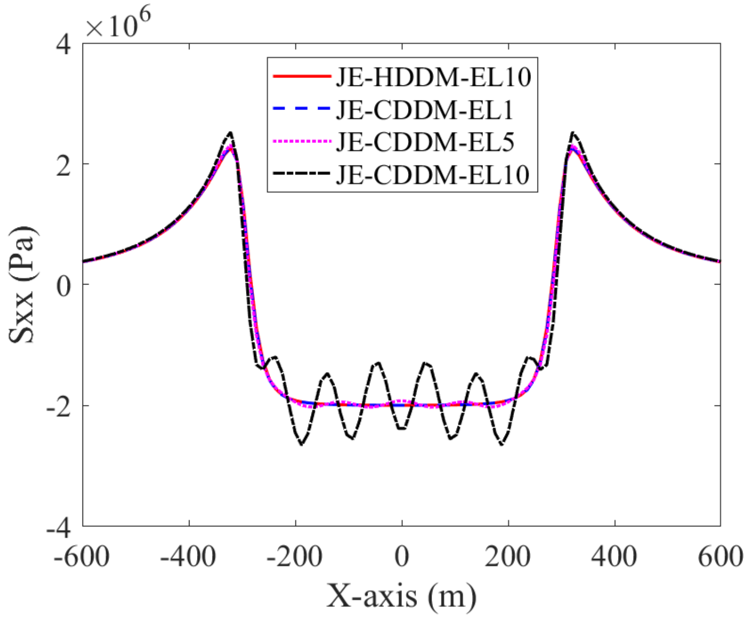

Figure 2.18 Comparison of JE-HDDM and JE-CDDM in terms of induced Sxx profiles along the fractures using different element lengths at location A. (Reprinted from Li et al 2022)

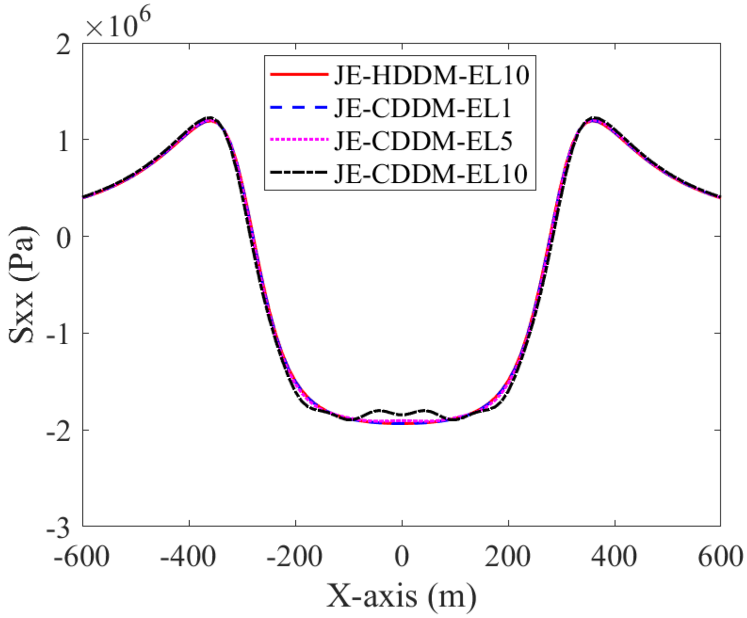

Figure 2.19 Comparison of JE-HDDM and JE-CDDM in terms of induced Sxx profiles along the fractures using different element lengths at location B. (Reprinted from Li et al 2022)

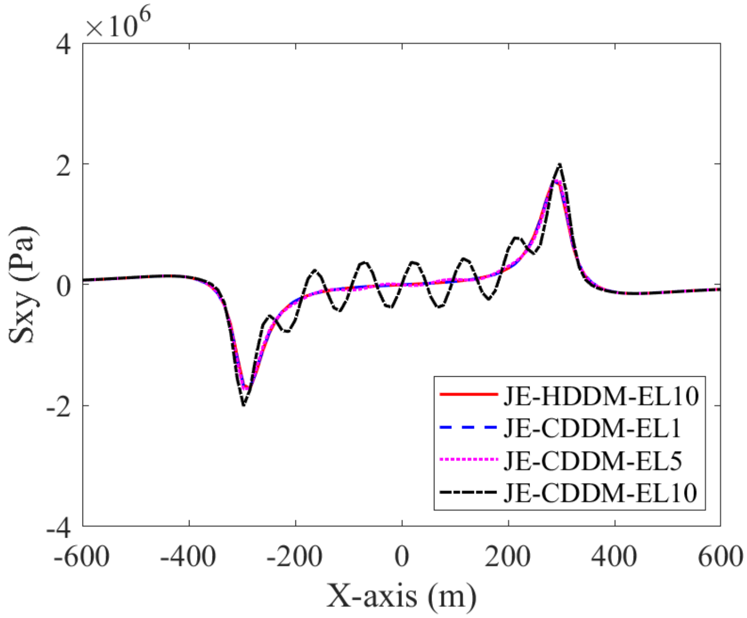

Figure 2.20 Comparison of JE-HDDM and JE-CDDM in terms of induced Sxy profiles along the fractures using different element lengths at location A. (Reprinted from Li et al 2022)

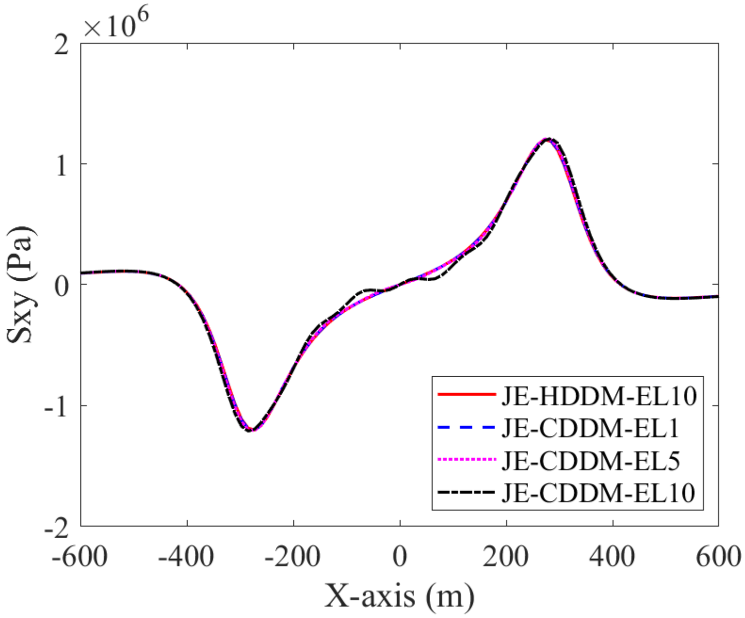

Figure 2.21 Comparison of JE-HDDM and JE-CDDM in terms of induced Sxy profiles along the fractures using different element lengths at location B. (Reprinted from Li et al 2022)

Figure 2.22-2.25 illustrate the induced stress profiles S_{xx} and S_{xy} along y axis and perpendicular to the hydraulic fracture in different distances, as indicated in Figure 2.8 locations C and D. Overall, we observed the similar trend with Figure 2.18-2.21. JE-HDDM maintains high accuracy and stability no matter at what locations using different lengths of element, while JE-CDDM loses stability and accuracy when getting closer to the fractures. In near-fracture area, the deficiency and inaccuracy of the JE-CDDM results are more obvious than the results along the fractures. This deficiency of JE-CDDM may result in inaccurate prediction of hydraulic fracture propagation direction. The development and application of JE-HDDM and the joint element is of vital importance.

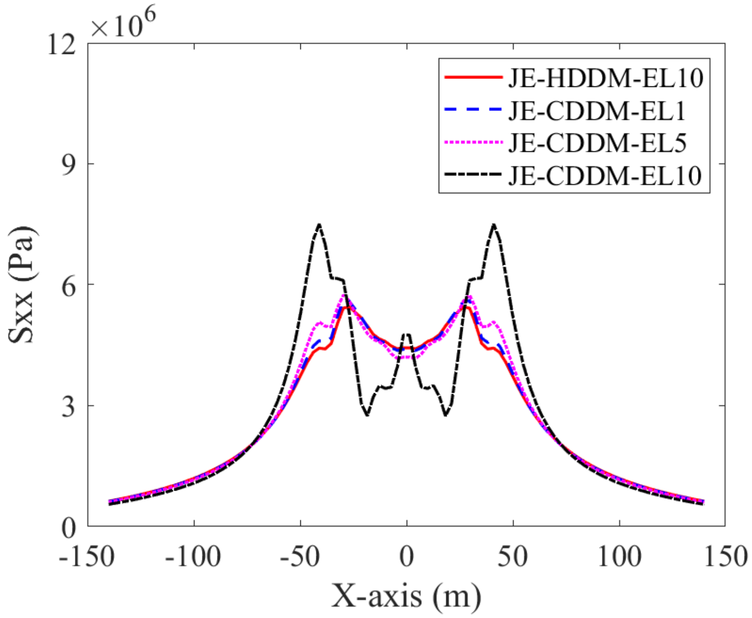

Figure 2.22 Comparison of JE-HDDM and JE-CDDM in terms of induced Sxx profiles perpendicular to the fractures using different element lengths at location C. (Reprinted from Li et al 2022)

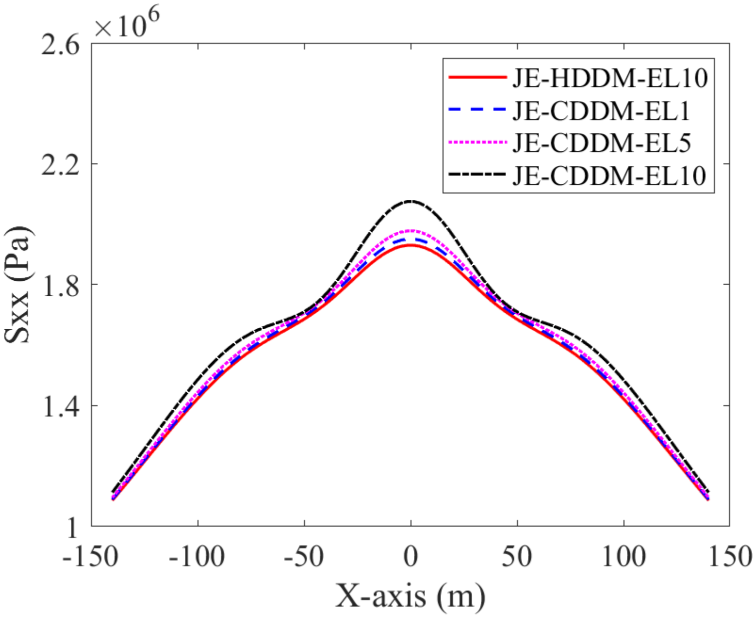

Figure 2.23 Comparison of JE-HDDM and JE-CDDM in terms of induced Sxx profiles perpendicular to the fractures using different element lengths at location D. (Reprinted from Li et al 2022)

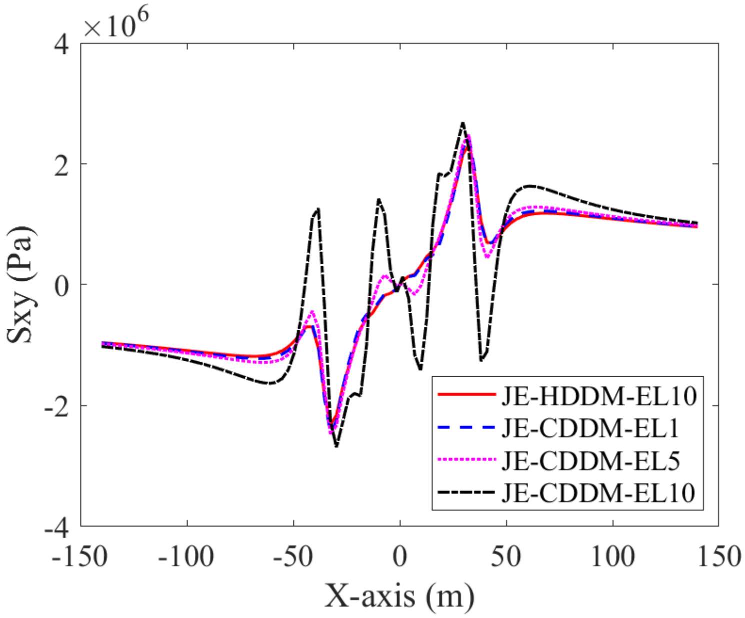

Figure 2.24 Comparison of JE-HDDM and JE-CDDM in terms of induced Sxy profiles perpendicular to the fractures using different element lengths at location C. (Reprinted from Li et al 2022)

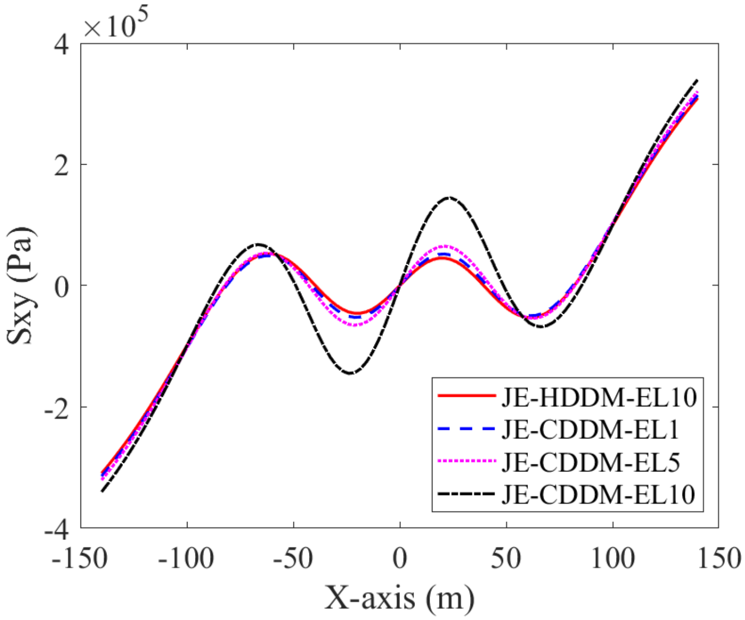

Figure 2.25 Comparison of JE-HDDM and JE-CDDM in terms of induced Sxy profiles perpendicular to the fractures using different element lengths at location D. (Reprinted from Li et al 2022)

2.5.3. Stress intensity factors

Stress intensity factors are important in the analysis of geo-mechanical problems because they are directly related to the fracture propagation and rock failure criteria. As mentioned before, the assumption of constant displacement discontinuities limits the accuracy of CDDM. In this section, we investigated the accuracy of the JE-HDDM in calculating the stress intensity factors over JE-CDDM. The relationship between the stress intensity factors (first and second mode) and the corresponding displacements of the tip element are given by Kachanov et al. (2003), which is expressed as following:

$$\begin{aligned} u_n^{\pm} &= \pm 2\frac{1-v^2}{E}\sqrt{\frac{2r}{\pi}}K_I \\ u_s^{\pm} &= \pm 2\frac{1-v^2}{E}\sqrt{\frac{2r}{\pi}}K_{II} \end{aligned} \tag{2.33}$$

where u_n and u_s are the normal and shear displacements, v is the Poisson's ratio, E is the Young's modulus, r is the half length of the element length, K_I and K_{II} are Mode I and Mode II stress intensity factors. Rearranging the Equation (2.33) and noticing that $D_{n(s)} = u_{n(s)}^{-} - u_{n(s)}^{+}$ we obtain the equations for computing the stress intensity factors using the displacement discontinuities of the tip element as well as the element length, as expressed as follows

$$\begin{aligned} K_I &= \frac{D_n}{4\frac{1-v^2}{E}\sqrt{2r/\pi}} \\ K_{II} &= \frac{D_s}{4\frac{1-v^2}{E}\sqrt{2r/\pi}} \end{aligned} \tag{2.34}$$

In section 2.5.1 we have already demonstrated the difference of the two methods, JE-HDDM and JE-CDDM, for predicting the displacement discontinuities. We have noticed that larger relative errors occur around the fracture tips. In this section we investigate the stress intensity factors of the four fractures indicated in Figure 2.8 using the displacement discontinuities calculated from these two methods. The results are shown in Figure 2.26 and Figure 2.27. The results given by JE-HDDM using 1 m element length are set to be accurate and the relative errors are compared against the accurate results. Figure 2.26 and Figure 2.27 indicate that the JE-CDDM overall generates results with large errors and the errors keep increasing when using larger computational elements, while JE-HDDM can provide accurate results, even using coarse elements. The largest relative error given by JE-HDDM using 10 m element is less than 6%, while the largest relative error given by the JE-CDDM is over 100%, as shown in Figure 2.26-2.27. Table 2.3 and 2.4 record the Relative error of first mode stress intensity factor computed by the displacement discontinuities given by HDDM and CDDM for fractures 1, 2, 3, and 4.

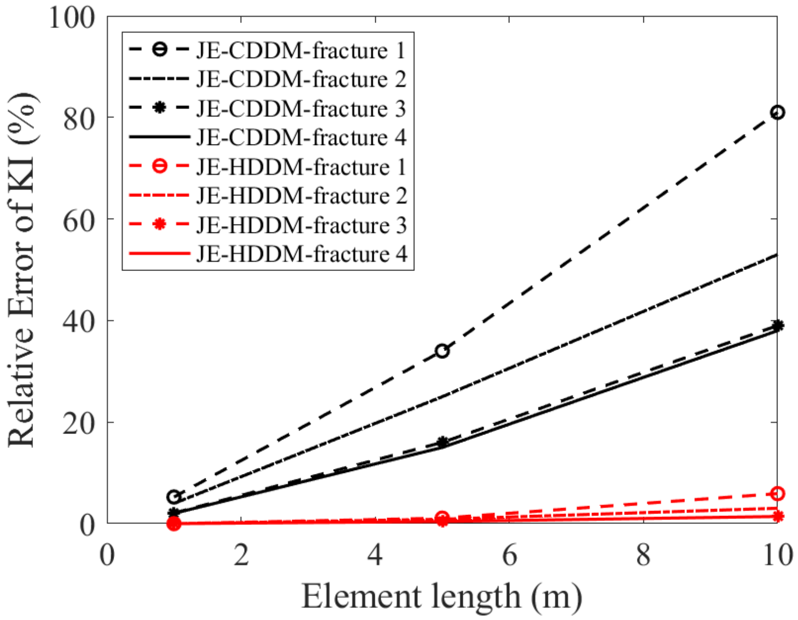

Figure 2.26 Relative error of the Mode I stress intensity factor computed by the displacement discontinuities given by JE-HDDM and JE-CDDM for fractures 1, 2, 3, and 4. (Reprinted from Li et al 2022)

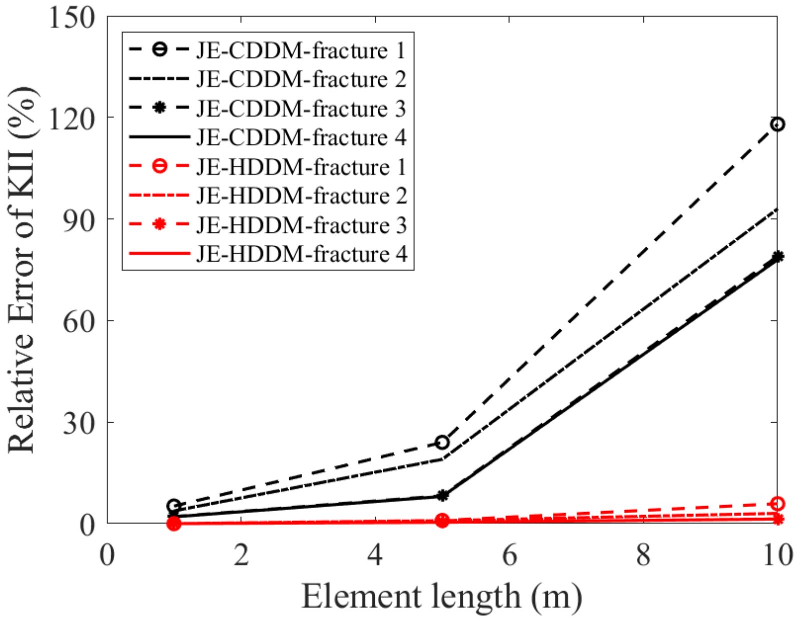

Figure 2.27 Relative error of the Mode II stress intensity factor computed by the displacement discontinuities given by JE-HDDM and JE-CDDM for fractures 1, 2, 3, and 4. (Reprinted from Li et al 2022)

Table 2.3 Relative error of first mode stress intensity factor computed by the displacement discontinuities given by HDDM and CDDM for fractures 1, 2, 3, and 4. (Reprinted from Li et al 2022)

Fracture	1		2		3		4	
EL(m)	CDDM	HDDM	CDDM	HDDM	CDDM	HDDM	CDDM	HDDM
10	81%	1.97%	53%	1.01%	39%	0.47%	39%	0.47%
5	34%	0.36%	25%	0.29%	16%	0.14%	16%	0.14%
1	5.24%	accurate	3.98%	Accurate	2.09%	accurate	2.09%	accurate

Table 2.4 Relative error of second mode stress intensity factor computed by the displacement discontinuities given by HDDM and CDDM for fractures 1, 2, 3, and 4. (Reprinted from Li et al 2022)

Fracture	1		2		3		4	
EL(m)	CDDM	HDDM	CDDM	HDDM	CDDM	HDDM	CDDM	HDDM
10	78%	1.96%	53%	1.01%	39%	0.47%	39%	0.47%
5	32%	0.31%	25%	0.29%	16%	0.14%	16%	0.14%
1	5.19%	accurate	3.98%	Accurate	2.09%	accurate	2.09%	accurate

Another interesting trend observed by comparing Figures 23 and 24 is that JE-CDDM loses accuracy in predicting K_{II} much faster than K_I when increasing the element length, while JE-HDDM does not. As shown in Figures 23 and 24, the relative error of K_{II} using 10 m element length by JE-CDDM is over 100% while the relative error of K_I is 81%, but the results of K_{II} provided by JE-HDDM using 10 m element length is more accurate than that of K_I. This suggests that when dealing with the shear slippage or shear dilation of the fractures or bedding planes where the second mode stress intensity factor is of great importance, JE-HDDM is highly recommended otherwise intensive fine grids of JE-CDDM must be used.

2.6. Conclusions

The joint element higher order displacement discontinuity method (JE-HDDM) is developed in this chapter. A new efficient higher order displacement discontinuity method (HDDM) is developed from 2D CDDM but has quadratic approximation of displacement discontinuity instead of constant variation. It can also be extended to 3D in a similar way. The quadratic approximation is performed on a three-element patch to avoid introducing the additional degrees of freedom on each element. Comparisons between the CDDM and HDDM of the same problems with the same sizes of elements show that HDDM has much higher accuracy than that of CDDM while maintains the same magnitude of computational time. The HDDM gives almost the same result with the CDDM when the fracture spacing is large (fracture spacing to fracture half-length ratio larger than around 1/10) and the fine grids are used. For close-spacing multi-fracture problems, the inner fractures are strongly affected by the stress shadowing effect and are mechanically closed. In such cases, the CDDM gives negative normal displacement discontinuities which are physically unrealistic. The joint-element higher order displacement discontinuity method (JE-HDDM) should be used to quantitatively and accurately capture the closure, opening, and shearing of the fractures. When decreasing the fracture spacing between multiple fractures, the CDDM requires more and more finer grids to give accurate results, and may become unstable and fail to capture the fracture behavior even using extremely fine grids when the spacing is too small. However, the HDDM does not require finer grid sizes to obtain accurate results and precisely predict the fracture opening, which saves a huge amount of computational time.

3. HYDRAULICALLY INDUCED SHEAR SLIPPAGE OF WEAK BEDDING INTERFACES IN SHALE LAMINATIONS

3.1. Introduction

Bedding planes are widely distributed in the unconventional shale formations and are affecting the hydraulic fracturing in a way we haven’t clearly understood. Usually these bedding layers are not mechanically open due to large overburden stress, yet hydraulic fracturing has been inferred to trigger the injection-induced seismic events as related to the nucleation and propagation of the pre-existing weak bedding interfaces. Although the basic principles of the injection-induced bedding interface shear slippage have been extensively studied and researched, critical details remain incomplete as regard to the activation and the subsequent propagation of the shear slippage.

The way the hydraulic fracture height growth being influenced by the bedding layers can be summarized as crossing, slowing down, deflecting, and terminating depending on different types of the rock fabric elements, as shown in Figure 3.1. As depicted in the figure, the type of horizontal interfaces can be divided into four categories, i.e., weak interfaces, stiff interfaces, stringers, and the weak beds. Shear sliding and the slippage propagation are more likely to happen in the horizontal weak interfaces. During hydraulic fracturing process, the fluid injection pressure exceeds the minimum in-situ stress, consequently creating and propagating one or more tensile fractures.

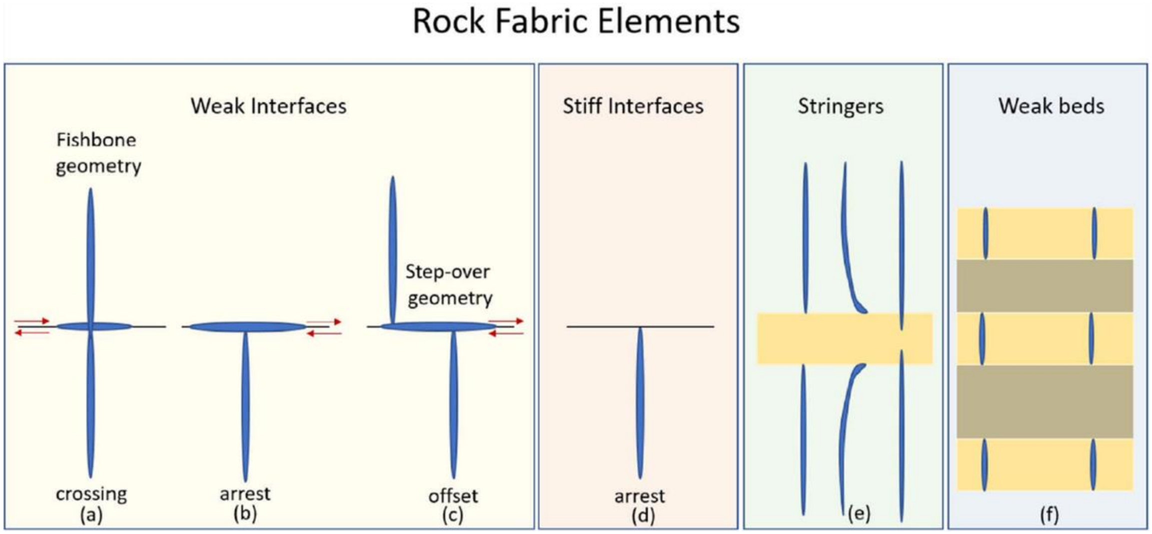

Figure 3.1 Different types of the rock fabric elements and the impacts on the hydraulic fracture vertical propagation.

In case of a laminated shale formation, a hydraulic fracture will intersect horizontal weak interfaces between the laminations. If the weak interface is permeable, the fracture fluid will leak off from the vertical hydraulic fracture into the horizontal weak interface. The fluid leaking into the interface will elevate the pore pressure inside the interface which will reduce the effective normal stress acting on the natural fracture. Depending on the in-situ stresses, this reduction in effective stress may lead to shear failure or slippage along the horizontal weak interface. Shear slippage causes dilation due to mismatching of the fracture surfaces due to surface roughness. This can potentially increase the bedding interfacial conductivity and enhance fluid flow deeper into the interface (shown in Figure 3.2). Under the right stress conditions and natural fracture orientation, this shear-induced slippage can continue to propagate to a significant distance, driven by the fluid pressure from the main hydraulic fracture.

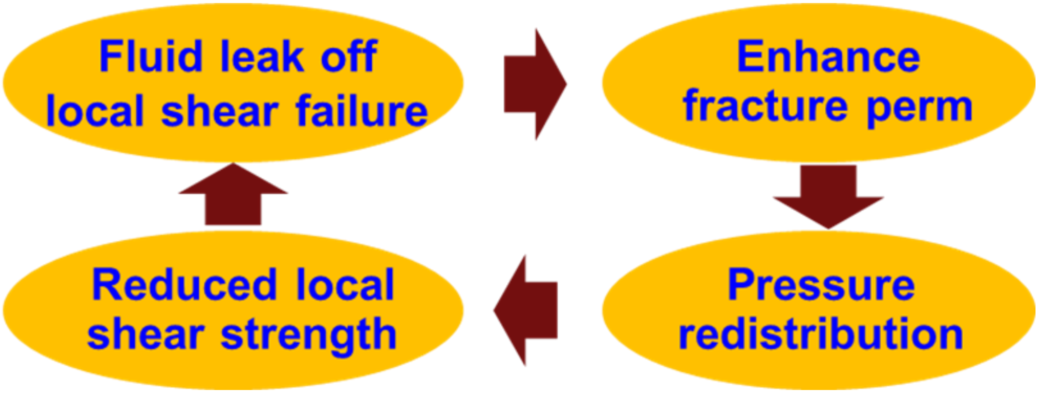

Figure 3.2 Physical procedure of the shear activation and slippage propagation in the horizontal weak bedding interface.

In this chapter, a coupled fluid flow and rock mechanical model is developed to better understand the physical process of bedding layer shear dilation and how it's influencing hydraulic fracture propagation and height growth. To accurately capture the shear slippage and propagation of the bedding layers induced by the hydraulic fracture, we applied a joint element based higher order displacement discontinuity method (JE-HDDM) which outperforms the constant displacement discontinuity method in accuracy but maintains same amount of computational time.

Then a static shear slippage model based on the "FracT" model (Chuprakov and Prioul 2015) is proposed and developed to effectively capture the sliding zone of the bedding interfaces as well as the shear displacement discontinuities. The static shear slippage model is a combination of the analytical "FracT" model and the JE-HDDM, which calculates the impact of the shear slippage of the horizontal weak bedding interfaces on the fracture height growth in a much more efficient way.

3.2. Dynamic shear slippage

The dynamic process of the interaction between a vertical hydraulic fracture with multiple horizontal bedding interfaces depicted in Figure 3.3 can be considerably complex, as this process is coupled by several physical mechanisms including but not limited to the rock deformation, hydraulic fracture propagation, bedding layer activation and propagation, interaction between hydraulic fracture and bedding layers, interaction among the bedding layers, and fluid flow in both hydraulic fracture and bedding layers against time. Rigorous modeling of this process is not only mathematically sophisticated but also computationally expensive. When the hydraulic fracture height reaches the equilibrium state at the given perforation pressure, the horizontal bedding layers are also assumed to reach the equilibrium state. Therefore, the initial activation of the shear slippage of the bedding layers and the dynamic fluid flow inside the fractures are less essential compared to other mechanisms and will not be considered in this model. A geometric depiction of a hydraulic fracture interaction with a horizontal bedding interface is demonstrated in Figure 3.3, where the blue color indicates the vertical hydraulic fracture, the black indicates the horizontal interface, the black arrow indicates the shear slippage propagation, and the red arrows indicate the fluid diffusion. σ_v is the in-situ vertical stress and τ_0 is the shear stress.

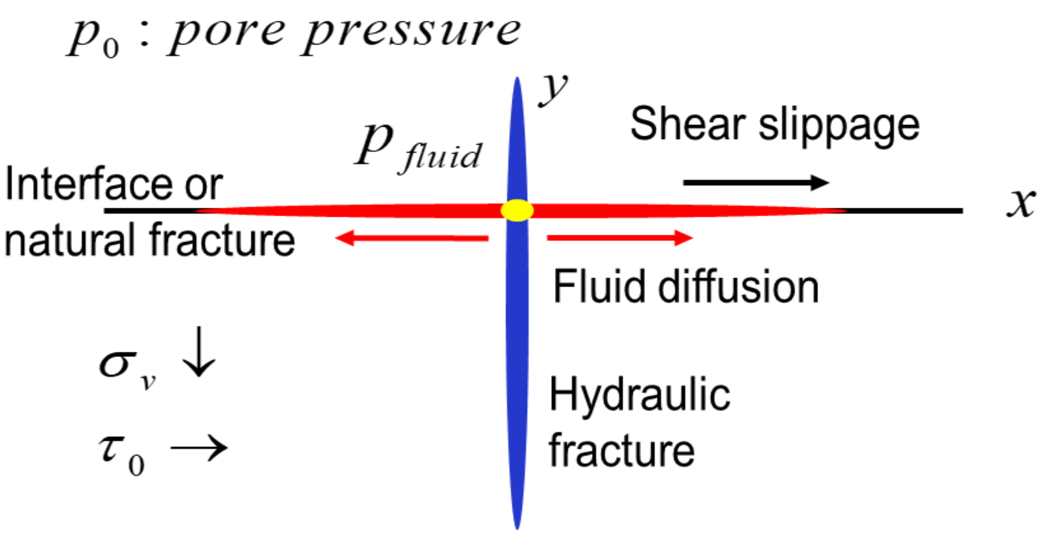

Figure 3.3 Geometric depiction of a vertical hydraulic fracture interaction with a horizontal weak interface.

3.2.1. Rock deformation

For a 2D crack propagation in an elastic medium, the equation governing the surface stress conditions and the fracture opening displacement is given by:

$$T(x,y)=\frac{G}{4\pi(1-v)}\int_{\Omega}\left(\frac{\partial}{\partial x}\left(\frac{1}{r}\right)\frac{\partial w}{\partial x'}+\frac{\partial}{\partial y}\left(\frac{1}{r}\right)\frac{\partial w}{\partial y'}\right)dx'dy' \tag{3.1}$$

where $r=\sqrt{(x-x')^2+(y-y')^2}$, $T(x,y)$ is the normal traction on the fracture surface, w is the fracture width, G is the shear modulus, v is the Poisson's ratio, and Ω is the fracture surface. For a straight horizontal weak bedding interfacial crack, the Equation (3.1) can be reduced to:

$$\sigma(x,t)-\sigma_0=\int_{-L_s}^{L_s}G(x,s)\Delta w(s)ds \tag{3.2}$$

$$\tau(x,t)-\tau_0=\int_{-L_s}^{L_s} G(x,s)u_s(s)ds \tag{3.3}$$

where G is Green's function given as:

$$G(x,s)=\frac{E'}{(x-s)^2} \tag{3.4}$$

E' is plane strain elastic modulus, $E'=\frac{E}{(1-v^2)}$, E and v are Young's modulus and Poisson's ratio, respectively.

3.2.2. Fluid mechanics

In a horizontal weak interface, the fluid pressure variation along the vertical direction can be negligible. An incompressible Newtonian fluid is considered in this model. Although the properties of the fracture fluid are often described by a non-Newtonian power law, the assumption of a Newtonian fluid simplifies the problem and provides a better physical understanding of the flow phenomenon. For an incompressible Newtonian fluid, the Navier-Stokes equation can be written in the following form (Currie, 1974):

$$\rho\frac{\partial v}{\partial t}=-\nabla p+\rho F+\mu\nabla^2 v \tag{3.5}$$

where $v=(v_x,v_y,v_z)$ is the velocity vector, p is the pressure, μ is the viscosity of the fluid, ρ is the density of the fluid, and F is the body force per unit mass.

Considering that the volume rate of the fluid flow per unit length in the x and y directions are defined as:

$$q = \int_{-w/2}^{w/2} v ds \tag{3.6}$$

Combining Equations (3.5) and (3.6) we can obtain the continuity equation which is written as:

$$\frac{\partial q}{\partial x} + \frac{\partial w}{\partial t} + q_L = 0 \tag{3.7}$$

where w is the effective mechanical aperture of the horizontal interface, and q_L is the fluid loss rate through the fracture walls into the neighboring rock matrix. The mechanical aperture is referred to an effective opening of the two surfaces in contact that gives the same storage volume provided by the void space at the interface due to the roughness of the surfaces.

The evolution of the effective permeability due to the pressure change and the shear dilation can be modeled by the following equation (Willis-Richards et al. 1966):

$$\begin{aligned} w &= w_n + w_s + w_{res} \\ &= \frac{w_0}{1 + 9 \sigma_n' / \sigma_{nref}} + u_s \tan \phi_{dil}^{eff} + w_{res} \end{aligned} \tag{3.8}$$

where w_0 is the initial fracture aperture without shear slippage, w_n is the fracture aperture without shear slippage, w_s is the shear slip induced dilation, w_{res} is the residual aperture which is generally negligible, σ_n' is the effective normal stress, and σ_{nref} is the reference stress in accordance with the stress that causes reduction of the aperture from w_0, u_s is the relative shear displacement, and ϕ_{dil}^{eff} is the effective shear dilation angle. According to Willis-Richards et al. (1966), ϕ_{dil}^{eff} is the dependent on the confining stress and has a similar form as w_n. Barton et al. (1985) developed an empirical formula for the hydraulic aperture w_f to the mean mechanical aperture w and the surface roughness:

$$w_f = \frac{w^2}{JRC^{2.5}} \tag{3.9}$$

where apertures are measured in microns, and *JRC* refers to the "joint roughness coefficient" and is dimensionless parameter that describes the surface roughness profile defined by Barton and Choubey (1977).

Apart from the continuity equation, the pressure gradient equation is needed to describe the fluid flow, which is described by the following equation:

$$\frac{\partial p}{\partial x} = -\frac{12\mu q}{w_f^3} \tag{3.10}$$

Here the cubic law is adopted, where the fracture permeability is related to the hydraulic fracture aperture:

$$k_f = \frac{w_f^2}{12} \tag{3.11}$$

Combining Equation (3.10) and (3.11) we can obtain the governing equation for the fluid flow inside the horizontal weak interface:

$$\frac{\partial}{\partial x}\left[\frac{w_f^3}{12\mu}\frac{\partial p}{\partial x}\right]=\frac{\partial w}{\partial t}+\frac{2c}{\sqrt{t-\tau(x)}} \tag{3.12}$$

where c is the leakoff coefficient from the horizontal weak interface into the matrix, and $\tau(x)$ is the time of the fluid arrival at location x.

3.2.3. Boundary Conditions

For a typical case where the hydraulic fracture is interacting with a horizontal weak interface, the following boundary conditions are satisfied:

$$p\left(0,t\right)=p_i \tag{3.13}$$

$$u_s(L_s,t)=0 \tag{3.14}$$

where p_i is the fluid pressure at the intersection point between the hydraulic fracture and the interface. These two boundary conditions indicate that the fluid pressure is constant at the intersection point, and that the shear and opening displacement discontinuities at the shearing front are both zero. To simplify the problem without loss of capturing the essential behavior of the shear slippage, another assumption is made that the interfacial pressure is initially equal to the reservoir pressure, i.e.:

$$p(L_f,t)=p_0 \tag{3.15}$$

At the meantime, the remote shear stress at the initial status satisfies the following condition:

$$\lambda_s(\sigma_0-p_{intf})<\tau_0<\lambda_s(\sigma_0-p_0) \tag{3.16}$$

where λ_s is the static Coulomb friction coefficient. This boundary condition indicates that the horizontal weak interface would not be activated under the initial in-situ stress conditions. However, after the fluid is injected from the hydraulic fracture into the horizontal interface and the pressure p_0 is elevated to p_{intf}, the shearing condition would be satisfied based on the Coulomb frictional law.

3.2.4. Numerical workflow

As mentioned in section 3.1 introduction, the procedure of the nucleation and the propagation of the shear slip is a coupled rock deformation and fluid flow problem. The rock deformation described in section 3.2.1 is discretized using the displacement discontinuity method based on the joint element. The JE-DDM formula for the closed part of the interface is given by:

$$-(\overset{i}{\sigma}_s)_0 = \begin{bmatrix} \overset{i(j-1)}{A}_{ss} & \overset{ij}{A}_{ss} & \overset{i(j+1)}{A}_{ss} \end{bmatrix} \begin{bmatrix} \overset{j-1}{D}_s{}' \\ \overset{j}{D}_s{}' \\ \overset{j+1}{D}_s{}' \end{bmatrix} + \begin{bmatrix} \overset{i(j-1)}{A}_{sn} & \overset{ij}{A}_{sn} & \overset{i(j+1)}{A}_{sn} \end{bmatrix} \begin{bmatrix} \overset{j-1}{D}_n{}' \\ \overset{j}{D}_n{}' \\ \overset{j+1}{D}_n{}' \end{bmatrix} + (\overset{i}{K}_s)(\overset{i}{D}_s{}')$$

$$-(\overset{i}{\sigma}_n)_0 = \begin{bmatrix} \overset{i(j-1)}{A}_{ns} & \overset{ij}{A}_{ns} & \overset{i(j+1)}{A}_{ns} \end{bmatrix} \begin{bmatrix} \overset{j-1}{D}_s{}' \\ \overset{j}{D}_s{}' \\ \overset{j+1}{D}_s{}' \end{bmatrix} + \begin{bmatrix} \overset{i(j-1)}{A}_{nn} & \overset{ij}{A}_{nn} & \overset{i(j+1)}{A}_{nn} \end{bmatrix} \begin{bmatrix} \overset{j-1}{D}_n{}' \\ \overset{j}{D}_n{}' \\ \overset{j+1}{D}_n{}' \end{bmatrix} + (\overset{i}{K}_n)(\overset{i}{D}_n{}')$$

(3.17)

and the formula for the shearing part of the interface is given by:

$$-({}^{i}\sigma_s)_0 = \begin{bmatrix} {}^{i(j-1)}A_{ss} & {}^{ij}A_{ss} & {}^{i(j+1)}A_{ss} \end{bmatrix} \begin{bmatrix} {}^{j-1}D_s' \\ {}^{j}D_s' \\ {}^{j+1}D_s' \end{bmatrix} + \begin{bmatrix} {}^{i(j-1)}A_{sn} & {}^{ij}A_{sn} & {}^{i(j+1)}A_{sn} \end{bmatrix} \begin{bmatrix} {}^{j-1}D_n' \\ {}^{j}D_n' \\ {}^{j+1}D_n' \end{bmatrix} - \lambda \sigma_n^i$$

$$-({}^{i}\sigma_n)_0 = \begin{bmatrix} {}^{i(j-1)}A_{ns} & {}^{ij}A_{ns} & {}^{i(j+1)}A_{ns} \end{bmatrix} \begin{bmatrix} {}^{j-1}D_s' \\ {}^{j}D_s' \\ {}^{j+1}D_s' \end{bmatrix} + \begin{bmatrix} {}^{i(j-1)}A_{nn} & {}^{ij}A_{nn} & {}^{i(j+1)}A_{nn} \end{bmatrix} \begin{bmatrix} {}^{j-1}D_n' \\ {}^{j}D_n' \\ {}^{j+1}D_n' \end{bmatrix} + ({}^{i}K_n)({}^{i}D_n')$$

(3.18)

where the coefficients A are explained and computed in details in section 2.2.4.

The fluid flow equation (3.12) is discretized using the finite difference method (FDM) and is solved for fluid pressure for a given distribution of mechanical hydraulic fracture aperture and the effective fracture opening. A numerical workflow is developed to iteratively solve this coupled problem, as shown in Figure 3.4. For each time step, an initial guess for fluid front, width distribution is assumed. Then the fluid flow equation and the rock deformation are solved iteratively based on Picard iteration method. While checking the status of the joint element, i.e., the separation mode, shearing mode, and close mode. The iteration process shown in Figure 2.5 is also involved. The convergence criterion is that the assumed width distribution agrees with the computed width distribution.

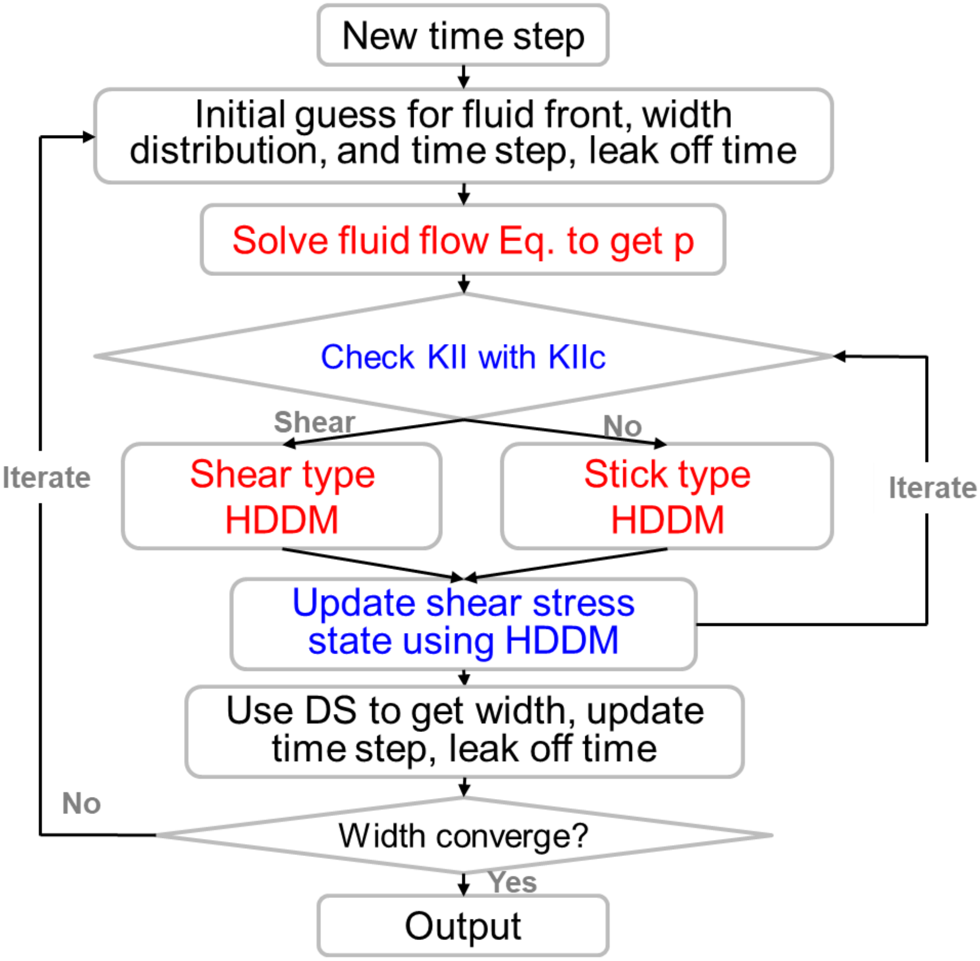

Figure 3.4 Numerical workflow for the mathematical model of the shear activation and slippage in the bedding interface.

3.3. Synthetic case study

A synthetic numerical case example is presented in this section to demonstrate the interaction between the hydraulic fracture and the interface, and the nucleation as well as the propagation of the shear slippage along the horizontal interface. The total half length of the bedding interface is 25 m and the initial effective opening of the interface is 5e-4 mm. The rest of the geomechanics properties and the fluid flow properties are recorded in Table 3.1.

Table 3.1 Parameters for the synthetic study of the hydraulic fracture and horizontal weak interface interaction.

Reservoir pressure	27 MPa
Injection pressure	62 MPa
Fluid viscosity	0.001 $Pa \cdot s$
JRC	10
Leakoff coefficient	2.36e-7 m/s
Normal stress	62 MPa
Shear stress	3.6 MPa
Young's Modulus	34.5 GPa
Poisson's ratio	0.25
Joint element K_N	13.57 GPa
Joint element K_S	13.57 GPa
Frictional coefficient	0.364
Shear dilation angle	10

Figure 3.5 presents the hydraulic fracture induced shear slippage activation and propagation of the horizontal weak interface. The whole procedure is much slower than that of the hydraulic fracture propagation. It takes around 2 hours for the shear slippage to propagate about 25 m, while a hydraulic fracture might propagate up to 250 m at the same time. At the initial state, the effective interfacial hydraulic aperture is only 5e-4 mm.

According to the cubic law, the effective permeability of the horizontal interface is much slower than the permeability in the main hydraulic fracture. The hydraulic fracturing fluid leaks from the vertical hydraulic fracture into the horizontal weak interface at a low pace due to the low permeability. Once the fluid enters the horizontal interface, the pressure inside the horizontal interface is elevated from the reservoir pressure to the fracture pressure at the contact point. The elevated interfacial pressure decreases the effective normal stress acting on the interface. Consequently, the shear strength is reduced according to Equation (3.16). Under the influence of the in-situ shear stress and the vertical fracture induced shear stress, the shear failure might happen in the horizontal interface. As a result, the effective opening is increased and the fluid leaking into the interface is further enhanced, as described in Figure 3.2.

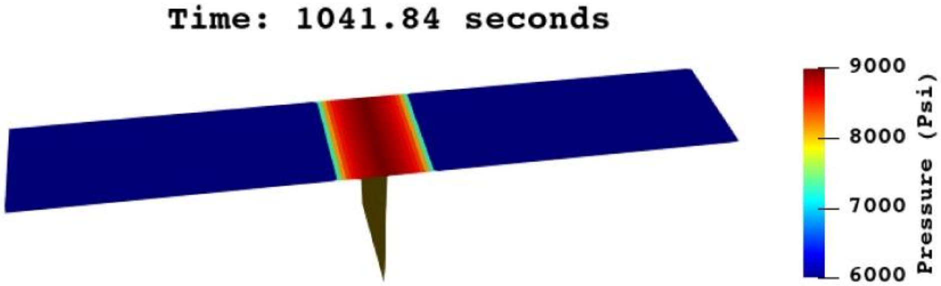

(a)

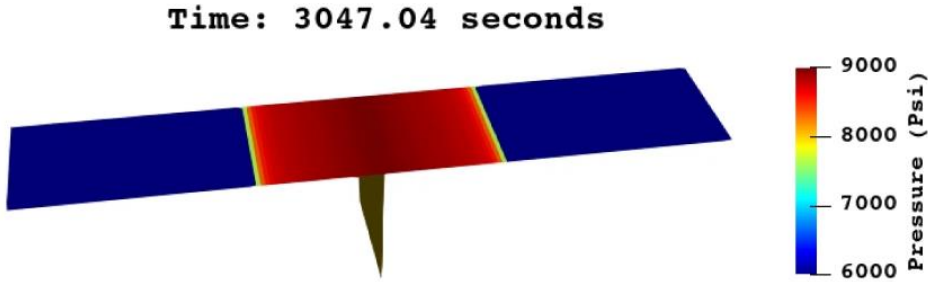

(b)

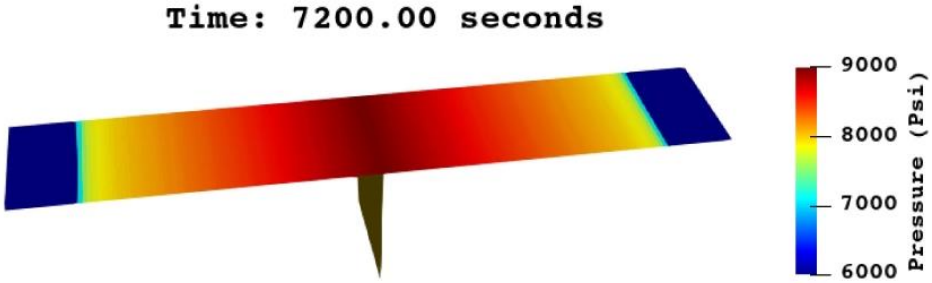

(c)

Figure 3.5 Hydraulically induced shear slippage activation and propagation in the horizontal weak interface at different time.

The fluid leaking off front and the induced shear slippage sliding front versus the injection time is described in Figure 3.6. As clearly seen in the figure, at the early state, the fracturing fluid is firstly leaking into the weak interface, inducing the shear slippage. The shear slip front together with the fluid front moves slowly at early stage due to the low permeability. As shown in Figure 3.6, at around 6000 seconds the enhanced conductivity of the horizontal interface speeds up the shear slippage and the shear slippage front take over the fluid front. The transitions of these two stages can be visualized in Figure 3.7.

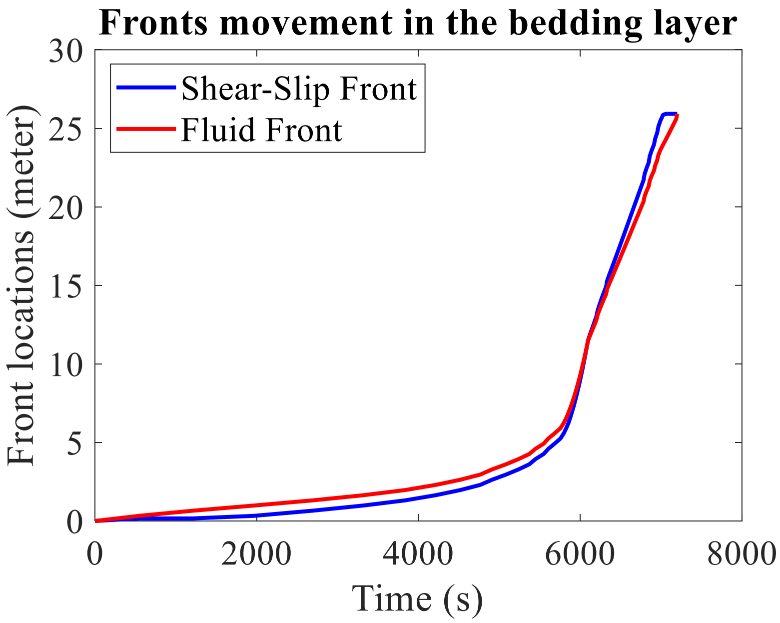

Figure 3.6 Fluid leaking off front and the induced shear slippage sliding front versus the injection time.

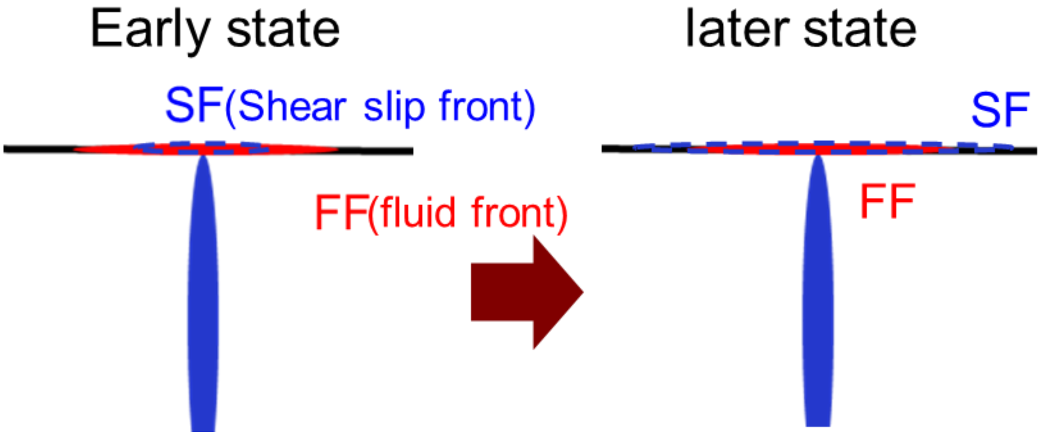

Figure 3.7 Fluid flow front and the shear slippage front at different stages.

The fluid leaking off volume and the evolution of the average conductivity of the horizontal interface against time are shown in Figure 3.8 and Figure 3.9. From these two figures we observe find out that the parameters increase slowly at the early stage and then rapidly at the later stage, which demonstrates similar trend as the shear slippage activation and the propagation. Ultimately, the fluid leaking off volume is around 0.25 m^2 / m, which is about few percent of the fracturing fluid. The ultimate average conductivity of the weak interface is around several md-ft, which is much less competitive than the propped fracture conductivity, while similar magnitude of a unpropped fracture conductivity.

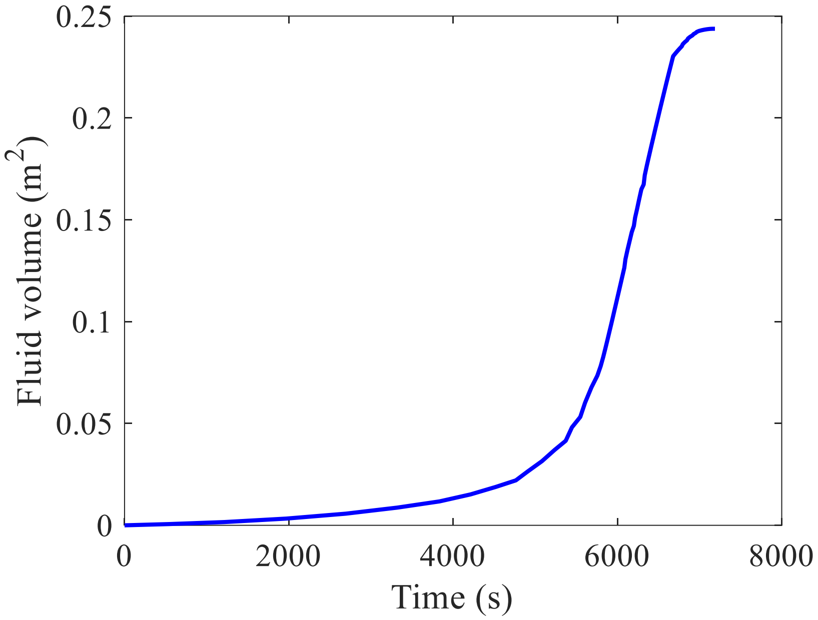

Figure 3.8 Fluid volume leaking into the horizontal weak interface against the injection time.

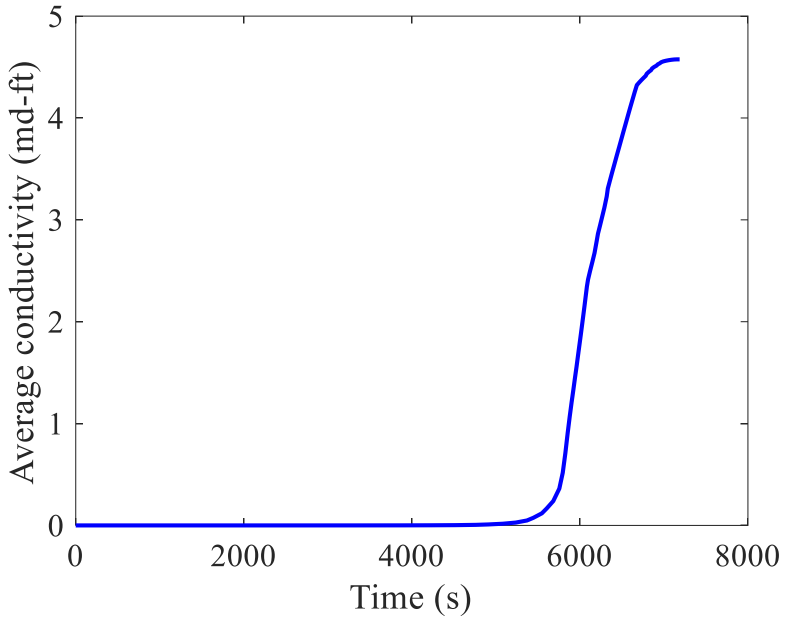

Figure 3.9 Evolution of the average conductivity of the horizontal weak interface against the injection time.

Understanding the process of the hydraulically induced shear slippage activation and the propagation is essential for quantifying the impact of the bedding interfaces on the hydraulic fracture height evolution. The dynamic coupled fluid flow and rock deformation model provides a tool for numerical simulation of the physical process and the analysis of the impact factors. In the following sections, we investigate the effects of the fluid viscosity and the initial interface width on the shear slippage and dilation.

3.3.1. Effect of fluid viscosity on the shear dilation

In this section, the effect of the fracturing fluid viscosity is investigated. The fluid viscosity not only has a considerable impact on the hydraulic fracture propagation, but also a significant influence on the horizontal weak interfacial shear slippage and dilation.

Three cases with different fluid viscosities are compared in this section, i.e., 0.1 cp, 1.0 cp, and 10 cp, with 1.0 cp our base case. The shear sliding length and the pressure distribution along the horizontal interface in these three cases are shown in Figure 3.10. As indicated in the figure, the shear sliding propagates faster with low fluid viscosity and slower with large fluid viscosity. In 2 hours, the shear sliding length for the fluid viscosity 0.1 cp, 1.0cp, and 10 cp are 25 m, 19.8 m, and 13.4 m, respectively. Correspondingly, the fluid volume that is leaking from the hydraulic fracture into the horizontal interface is decreasing from 0.26 m^2 when viscosity is 0.1 cp, to 0.23 m^2 and 0.19 m^2, when fluid viscosity is 1.0 cp and 10 cp, respectively.

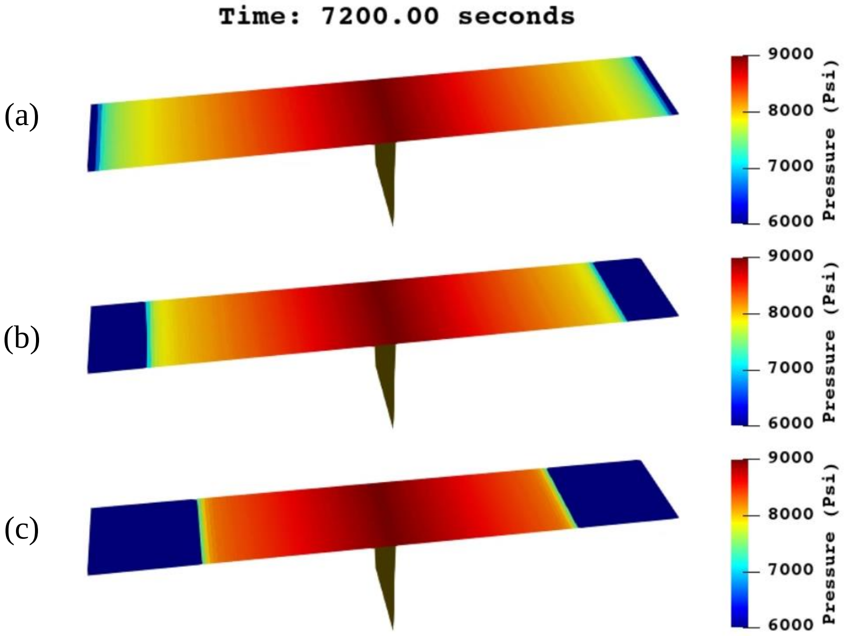

Figure 3.10 Shear slippage and pressure distribution along the horizontal interface at different fluid viscosities. (a) fluid viscosity = 0.1 cp, (b) fluid viscosity = 1.0 cp, (c) fluid viscosity = 10 cp.

3.3.2. Effect of Initial Bedding Layer Width

The initial horizontal weak interface effective aperture is another parameter that has considerable impact on the shear sliding process. Three different initial effective hydraulic apertures of the interface, i.e., (a) 0.001 mm, (b) 0.0005 mm, and (c) 0.0001 mm are assigned and simulated to investigate the impact on the shear sliding process. The results are presented in Figure 3.11. The figure indicates that smaller initial horizontal interfacial aperture has much slower shear slippage process and much shorter sliding zone. This is because that smaller initial hydraulic aperture generates low fracture permeability and conductivity. Lower permeability indicates lower process of the fluid leaking off from the hydraulic fracture into the horizontal interface, which results in a lower process of the shear activation and the consequent propagation. After 2 hours injection from the hydraulic fracture, the total fluid leaking volume from the hydraulic fracture into the horizontal interface for the three cases (a), (b), (c) are 0.28 m^2, 0.23 m^2, and 0.07 m^2, respectively. The fluid volume in case (c) is almost negligible compared to the fracturing fluid volume. Additionally, the sliding length in case (c) is only a few meters, indicating that the shear slippage mechanism in small-initial-aperture interfaces can be negligible.

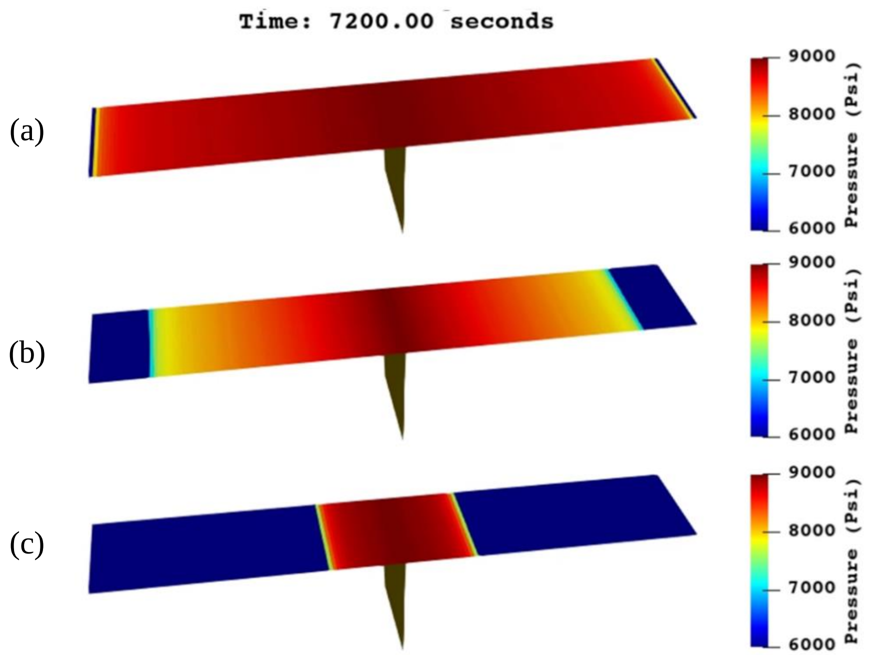

Figure 3.11 Shear slippage and pressure distribution along the horizontal interface at initial effective hydraulic aperture. (a) initial aperture = 0.001 mm, (b) initial aperture = 0.0005 mm, (c) initial aperture = 0.0001 mm.

3.4. Static shear slippage

The dynamic coupled fluid flow and rock deformation model of the shear activation and propagation has improved our understanding of the bedding interfacial shear slippage. Yet it is too computationally intensive to be incorporated into an efficient height model for field-scale engineering design. In this section, a static shear slippage model based on the “FracT” model (Chuprakov and Prioul 2015) is proposed and developed to effectively capture the sliding zone of the bedding interfaces as well as the shear displacement discontinuities. The static shear slippage model is a combination of the analytical model and the JE-HDDM, which calculates the impact of the shear slippage of the horizontal weak bedding interfaces on the fracture height growth in a much more efficient way. To maintain the computational efficiency, the dynamic fluid flow process is not explicitly calculated in this static model. Details regarding to the impact of the fluid flow on the shearing process are referred to the section 3.2.

The fracture straightening method (FSM) is proposed by Chuprakov (2015) to approximate the width profile and the lateral sliding length of a T-shaped hydraulic fracture. The FSM is based on the analytical solution (equation 7) of a straight plane-strain fracture in an infinite homogeneous elastic medium (Kachanov et al., 2013).

$$w(x) = \frac{4}{\pi E'} \int P(a) \ln \frac{l^2 - ax + \sqrt{l^2 - a^2}\sqrt{l^2 + a^2}}{l\left|x - a\right|} da \tag{3.19}$$

where l is the fracture half length, a ranges from $-l$ to l. P is the net pressure, E' is the Young's modulus for plane strain problem, x is the location for width computation.

In FSM, a T-shaped hydraulic fracture is virtually straightened into a straight hydraulic fracture, as shown in figure 7. L stands for the original fracture half height. L_{str} stands for the straightened fracture half height. For symmetric-arrest hydraulic fracture, $L_{str} = L + b_s$; for asymmetric-arrest hydraulic fracture, $L_{str} = L + b_s / 2$. The straightened hydraulic fracture follows two assumptions and two boundary conditions.

- Assumption 1. The actual opening of the T-shaped hydraulic fracture in the zone $\left|y\right| < L$ is assumed to be equal to the opening of the straightened fracture, which is

$$w(y) \approx w_{str}(y), 0 < \left|y\right| < L \tag{3.20}$$

- Assumption 2. The sliding at the interface segments is assumed to be equal to half of the opening of the straightened fracture past the interface

$$w(|y|-L) \approx w_{str}(y)/2, L<|y|<L_{str} \tag{3.21}$$

- Boundary condition 1. The net pressure within the segment $|y|<L$ is set equal to the one of the straightened fracture

$$p'(y) \approx p'_{str}(y), 0<|y|<L \tag{3.22}$$

- Boundary condition 2. The critical shear stress τ_m at the frictional interface multiplied by a calibration factor is equal to the negative of the net pressure past the interface

$$\bar{\tau}_m = -p'_{str}(y), L<|y|<L_{str}, \bar{\tau}_m = \chi\tau_m \tag{3.23}$$

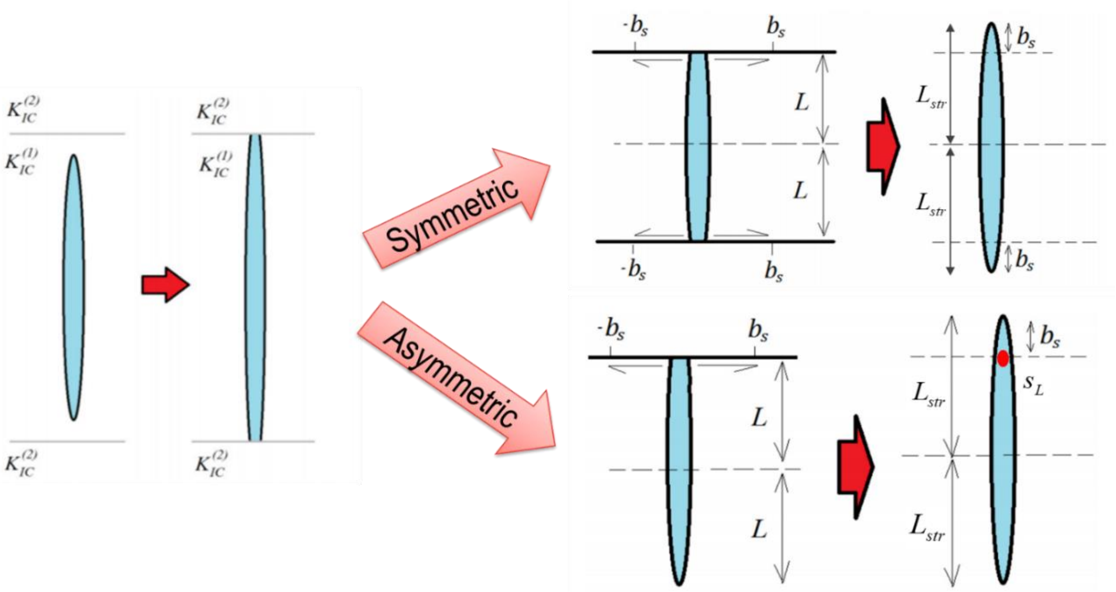

Figure 3.12 Fracture straightening method, Symmetric arrest: H-shaped fracture, Asymmetric arrest: T-shaped hydraulic fracture (Modified from Chuprakov and Prioul 2015).

Based on the above assumptions, the following equations can be obtained for the horizontal interfaces under the equilibrium status:

$$K_{II}^{intf} = K_{IIc}^{intf} \tag{3.24}$$

$$K_I^{str} = K_{II}^{intf} \tag{3.25}$$

According to the linear elastic fracture mechanics, the stress intensity factor of the straightened vertical fracture can be calculated by:

$$K_I^{str} = \sqrt{\frac{1}{\pi h_f^{eff}}} \int_{-h_f^{eff}}^{h_f^{eff} - S_L} (p(y) - \sigma(y)) \sqrt{\frac{h_f^{eff} + y}{h_f^{eff} - y}} dy + \sqrt{\frac{1}{\pi h_f^{eff}}} \int_{h_f^{eff} - S_L}^{h_f^{eff}} (p_{str} - \sigma_v) \sqrt{\frac{h_f^{eff} + y}{h_f^{eff} - y}} dy \tag{3.26}$$

where h_f^{eff} is the effective straightened hydraulic fracture half height, S_L is the distance from the bedding layer shear slippage tip to the hydraulic fracture, i.e., half of total shearing length, σ_v is the vertical in-situ stress acting on the bedding layers. By solving Equations (3.24) - (3.26) we can obtain the bedding layer shear slippage length at the equilibrium state.

Once the length of the shear sliding zone is obtained from the static model, the shear displacement discontinuities of the horizontal interfaces can be calculated using the proposed JE-HDDM method introduced in Chapter 2.

3.5. Conclusions

In this chapter, the hydraulic fracture induced shear slippage activation and the fluid-driven propagation in the horizontal weak interface in shale laminations is investigated. Two models are developed to study the physical process and the geometries of the shear slippage including the dynamic shear slippage model coupling the fluid and the rock deformation, and the static model under the equilibrium status assuming the linear elastic fracture mechanics.

The dynamic model captures the activation of the shear slippage based on the boundary conditions and the Mohr-Coulomb criterion. The propagation of the shear slippage is initially driven by the fluid leaking off from the vertical fracture into the interface, and then driven by the shear induced dilation of the fracture interfaces.

The static model provides us an efficient way to predict and calculate the final geometry of the horizontal shear slippage, which can be used in the fracture height model to quantify the effectiveness on the fracture height growth and simultaneous lateral propagation.

4. HYDRAULIC FRACTURE HEIGHT GROWTH CONSIDERING EFFECT OF WEAK BEDDING PLANES*

4.1. Introduction

Understanding and quantifying the effect of the weak bedding layers on the hydraulic fracture height growth in shale formations have always been challenging during the hydraulic fracturing design and operations. This chapter introduces a comprehensive and non-intrusive hydraulic fracture height growth model that accounts for both formation rock properties and the weak interfaces, and can be incorporated into pseudo-3D hydraulic fracture simulators. The formation rock properties are handled by the equilibrium fracture height model. The shear slippage of the weak bedding layers is simulated by an efficient 2D higher order displacement discontinuity method and the effectiveness on the hydraulic fracture height is quantified by correcting the stress intensity factors at the hydraulic fracture tips. The model is applied in the Permian Basin Wolfcamp formation to quantitatively investigate the effect of bedding layers on the hydraulic fracture height growth. Numerical studies show that the shear slippage of the beddings can significantly slow down the hydraulic fracture height growth and that the shear fracture toughness of the bedding layers and the spacing between the laminations have considerable impact on the effectiveness of the shear slippage on the fracture height growth. Larger shear fracture toughness and smaller spacing of the bedding layers add more mechanical resistance on

---

* Part of this chapter is reprinted with permission from “An Efficient Model for Hydraulic Fracture Height Growth Considering the Effect of Bedding Layers in Unconventional Shale Formations” by Li, J. and Wu, K. 2022. SPE Journal, pp.1-17., Copyright [2022] by Society of Petroleum Engineers.

the fracture height propagation and requires larger pressure to breakthrough. Additional results show that the effect of bedding layers is more significant in formations with low-stress-contrast but less obvious in formations with high-stress-contrast. The impact of the landing depth on the hydraulic fracture height growth is also investigated to provide crucial insights on the optimization of the landing depth in laminated formations.

4.2. The equilibrium fracture height theory

The so called "equilibrium height belonging to a certain treating pressure" is adopted here which can provide an upper limit of the hydraulic fracture height in homogeneous rock (Simonson et al. 1978; Economides and Nolte 2000; Mack and Warpinski 2000; Weng et al. 2011; Liu and Valko 2017). The equilibrium means when given a treating pressure, the integration of the net pressure inside the fracture along the height (i.e. SIF, K_I) is equal to the fracture toughness K_{Ic} at both upper and lower tips at the same time. If the computed SIFs at either tip is higher than the K_{Ic} at the layer in consideration, the specific tip will grow and propagate, until the computed SIF becomes equal or slightly less than the K_{Ic} of the layer.

The solution for the equilibrium height has been investigated and developed since 1970s. The earliest solution was given by Simonson et al. in 1978 for a symmetric three-layer formation problem with exactly the same upper and lower minimum horizontal stress and the constant treating pressure along the fracture height, then it was extended by Mack and Warpinski to asymmetric multilayer formation problems. Liu and Valko have summarized the previous development of the equilibrium height mode and provided more case studies to investigate the effect of rock formation properties on the hydraulic fracture height. In this work, we adopt Liu and Valko's equation (Equation (4.1)) and their algorithm to develop the equilibrium height model, and improve the model to avoid the unrealistic solution pair and consider effect of bedding layers fracture toughness.

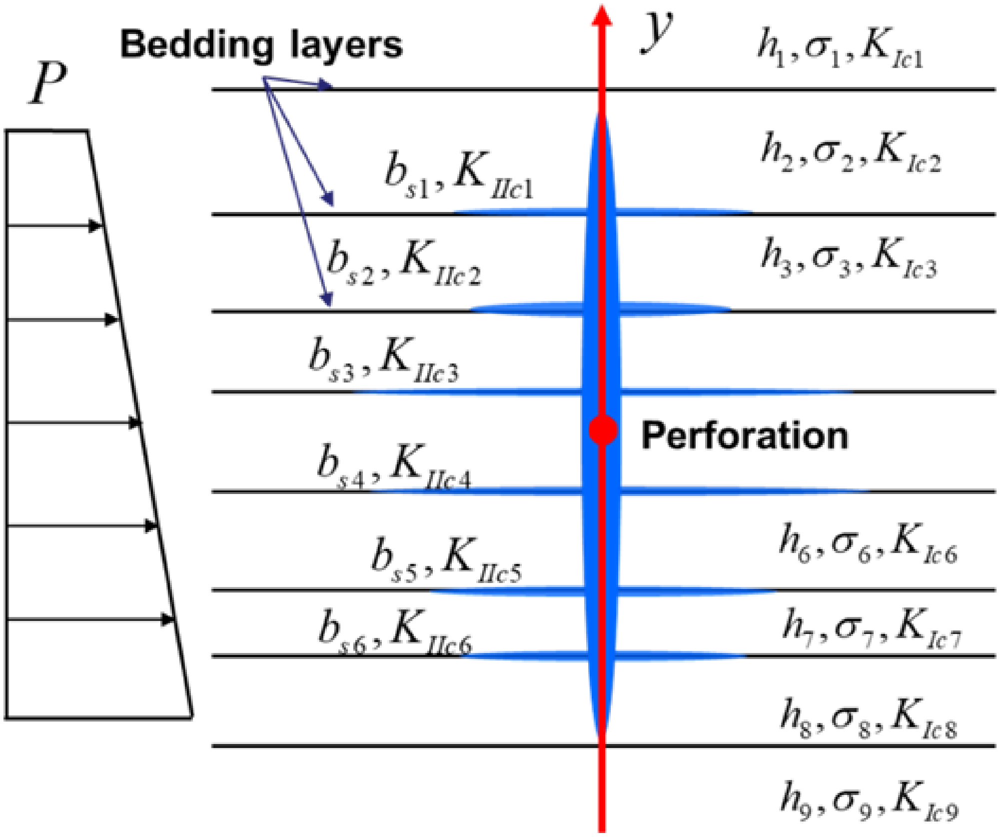

Figure 4.1 Mathematical depiction of hydraulic fracture height containment in thin laminations. (Reprinted from Li and Wu 2022b)

$$
\begin{aligned}
K_{I+} &= \sqrt{\frac{1}{\pi c}} \int_{-c}^{c} p_{net}(x) \sqrt{\frac{c+x}{c-x}} dx \\
K_{I-} &= \sqrt{\frac{1}{\pi c}} \int_{-c}^{c} p_{net}(x) \sqrt{\frac{c-x}{c+x}} dx
\end{aligned}
\tag{4.1}
$$

To obtain the equilibrium location of both upper tip and lower tip of the hydraulic fracture, we first need to discretize the whole layer in question into multiple thin layers. For example, as shown in Figure 4.1, the fracture vertical growth in three layers are computed by discretizing the three layers into multiple layers. For each step, the stress intensity factors (SIF) at both upper and lower fracture tips are computed using Equation (4.2). Then the SIFs are compared to the critical SIFs, or the fracture toughness of the layers. The equilibrium means the SIF is equal to the fracture toughness at both upper and lower tips at the same time. If the computed SIFs at either tip is higher than the K_{Ic} at the layer in consideration, the specific tip will grow and propagate, until the computed SIF becomes equal or slightly less than K_{Ic} the of the layer, where the "equilibrium status" is reached.

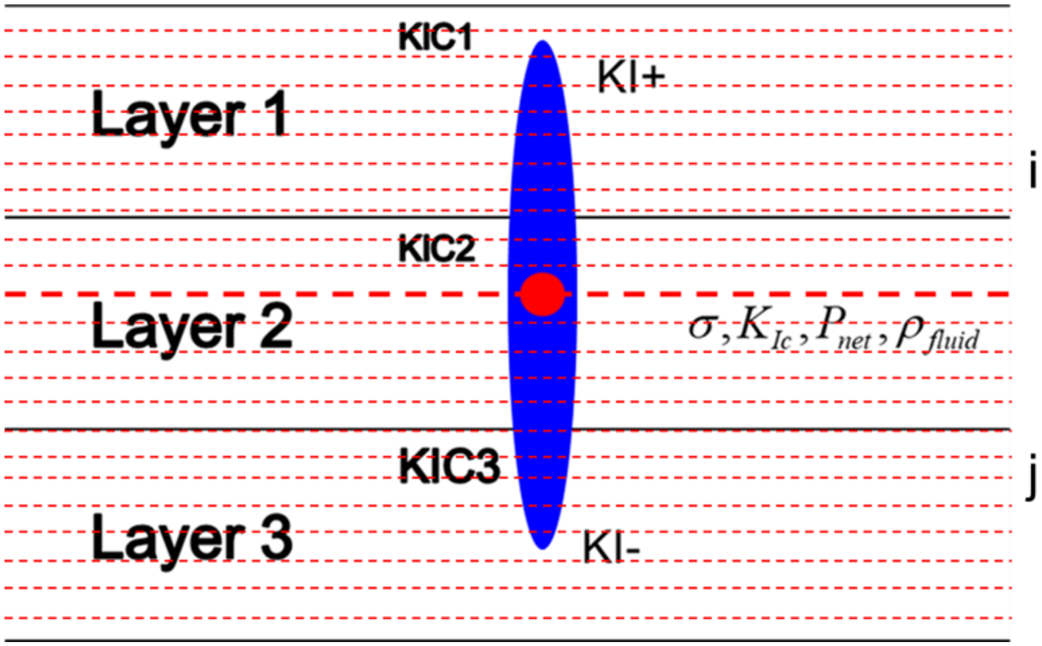

Figure 4.2 Discretization of the target layers for hydraulic fracture height growth.

$$
\begin{aligned}
K_I^{upper} &= \sqrt{\frac{\pi h_f}{2}}\left[\rho g\left(h_{perf}-\frac{3h_f}{4}\right)+p_{perf}-\sigma_n\right] \\
&+\sqrt{\frac{2}{\pi h_f}}\sum_{i=1}^{n-1}\left(\sigma_{i+1}-\sigma_i\right)\left[\frac{h_f}{2}\cos^{-1}\left(\frac{h_f-2h_i}{h_f}\right)-\sqrt{h_f(h_f-h_i)}\right] \\
K_I^{lower} &= \sqrt{\frac{\pi h_f}{2}}\left[\rho g\left(h_{perf}-\frac{h_f}{4}\right)+p_{perf}-\sigma_n\right] \\
&+\sqrt{\frac{2}{\pi h_f}}\sum_{i=1}^{n-1}\left(\sigma_{i+1}-\sigma_i\right)\left[\frac{h_f}{2}\cos^{-1}\left(\frac{h_f-2h_i}{h_f}\right)+\sqrt{h_f(h_f-h_i)}\right]
\end{aligned}
\tag{4.2}
$$

where h_{perf} is the perforation depth measured from the fracture lower tip, p_{perf} is the fluid pressure at the perforation depth, σ_i and h_i are the minimum in-situ stress and the distance from the i th layer (counted from upper tip) to the fracture lower tip.

Given a series of injection pressure, a full hydraulic fracture height map can be obtained with the equilibrium model. With the results, we are able to investigate the effect of the geo-mechanical properties of the rock formation, the fluid properties, the landing depth, and the bedding layers resistance caused by the enhanced fracture toughness.

The procedure is to compare the SIFs against the associated fracture toughness at the tips, if the SIF at either tip is higher than the associated fracture toughness, the tip will grow, otherwise the tip will be contained at the equilibrium state. The above workflow properly handled the formation rock parameters in the hydraulic fracture height growth. The effectiveness of the bedding layers is quantified by correcting the effective stress intensity factors at the fracture tips due to the interaction between bedding layers and hydraulic fracture.

4.3. Effect of bedding plane shear slippage on the hydraulic fracture height

At the equilibrium state, similar to the concept of the equilibrium fracture height theory, the equilibrium tip status of the bedding layers in a homogeneous rock can be expressed by

$$K_{II}^{intf} = K_{IIc}^{intf} \tag{4.3}$$

where K_{II}^{intf} is the mode II SIF of the bedding layers and K_{IIc}^{intf} is the critical mode II SIF of the bedding layers. At such state with the given perforation pressure, the bedding layer shearing has propagated to the maximum distance and reached the equilibrium.

The K_{IIc}^{intf} is to be measured and the K_{II}^{intf} can be computed from the integration of the net pressure inside the bedding layers. In shale formations, the bedding layers in the thin laminations are mostly mineralized with almost-zero permeability (Gale and Holder 2008; Weng et al. 2018) and may not be mechanically open throughout the whole stage of the hydraulic fracturing jobs. Yet the fluid leaking off into the bedding layers will induce the shear slippage as well as the propagation of the bedding layers, and consequently influences the pressure distribution. In real cases, the contact type of the bedding layer interfaces may include stick mode, shearing mode, or separation mode, or combinations of any two or three modes, and the fluid flow inside the interfaces may include more than one regime. Therefore, accurate simulation of the pressure distribution within the interfaces considering all of the physical mechanisms may be too technically difficult. Chuprakov and Prioul (2015) proposed an extensive semi-analytical way of estimating the mode II SIFs of the bedding layer interfaces without using the pressure distribution inside the interfaces. The idea is that under equilibrium state, the shear displacements at the interfacial segment can be effectively straightened to the open displacements at the corresponding segment of the vertical hydraulic fracture. And the pressure along the interfacial segment is assumed the same as that of the straightened parts. Therefore, the mode II SIF of the interface is equivalent to the mode I SIF of the straightened vertical fracture, which is expressed in Equation (4.4) (Since the left side is symmetric to the right side, a uniform equation is presented).

$$K_I^{str} = K_{II}^{intf} \tag{4.4}$$

The SIF of the straightened vertical fracture is given by:

$$K_I^{str} = \sqrt{\frac{1}{\pi h_f^{eff}}} \int_{-h_f^{eff}}^{h_f^{eff}-S_L} (p(y)-\sigma(y)) \sqrt{\frac{h_f^{eff}+y}{h_f^{eff}-y}}\,dy + \sqrt{\frac{1}{\pi h_f^{eff}}} \int_{h_f^{eff}-S_L}^{h_f^{eff}} (p_{str}-\sigma_v) \sqrt{\frac{h_f^{eff}+y}{h_f^{eff}-y}}\,dy \tag{4.5}$$

where h_f^{eff} is the effective straightened hydraulic fracture half height, S_L is the distance from the bedding layer shear slippage tip to the hydraulic fracture, i.e., half of total shearing length, σ_v is the vertical in-situ stress acting on the bedding layers. By solving Equations (4.4)-(4.5) we can obtain the bedding layer shear slippage length at the equilibrium state. Chuprakov and Prioul (2015) provided analytical solutions to the equation under conditions where either symmetric or asymmetric arrest of the hydraulic fracture by the interfaces is occurred. In our model the Equations (4.4)-(4.5) are solved numerically to maintain the accuracy in more complex field situations.

With the shear slippage length calculated, the interaction between the hydraulic fracture and the bedding layers, and the interaction among the bedding layers can be modeled by a 2D elasticity solution for the stress and displacements relationship (Equations (4.6)) using a boundary-element method. The derivation of the solution and the discretization of the formulation are elaborated in Crouch and Starfield (1983).

$$\begin{aligned} \overset{i}{\sigma}_s &= \sum_{j=1}^{N}\left(\overset{ij}{A}_{ss}\,\overset{j}{D}_s + \overset{ij}{A}_{sn}\,\overset{j}{D}_n \right) \\ \overset{i}{p} - \overset{i}{\sigma}_n &= \sum_{j=1}^{N}\left(\overset{ij}{A}_{ns}\,\overset{j}{D}_s + \overset{ij}{A}_{nn}\,\overset{j}{D}_n \right) \end{aligned} \tag{4.6}$$

where σ_s and σ_n are the shear and normal stresses on the fracture segments, D_s and D_n are the shear and normal displacement discontinuities of the fracture segments, A_{ss}^{ij}, A_{sn}^{ij}, A_{ns}^{ij}, and A_{nn}^{ij} are the 2D, plane-strain elastic influencing coefficients between the fracture segments i and j.

To achieve faster computation, the above set of linear equations system is solved using an efficient higher order displacement discontinuity method (HDDM) which is proposed and developed by Shou and Crouch (1995) and demonstrated robustness and efficiency by Li et al. (2021a, 2021b). The efficient HDDM adopts quadratic approximation (Equation (4.7)) of the displacement discontinuities on each fracture-segment patch which is composed of three fracture segments. Substituting Equation (4.7) into Equation (4.6) gives Equation (4.8). This way the method provides higher order approximation without introducing additional computational degrees of freedom.

$$D_i(\xi) = \sum_{j=1}^{3} N_j(\xi) D_i(j), i = x, y \tag{4.7}$$

$$\begin{aligned}
\sigma_s^{i} &= \sum_{j=1}^{N}\begin{bmatrix} A_{ss}^{i(j-1)} & A_{ss}^{ij} & A_{ss}^{i(j+1)} \end{bmatrix}\begin{bmatrix} D_s^{j-1} \\ D_s^{j} \\ D_s^{j+1} \end{bmatrix} + \sum_{j=1}^{N}\begin{bmatrix} A_{sn}^{i(j-1)} & A_{sn}^{ij} & A_{sn}^{i(j+1)} \end{bmatrix}\begin{bmatrix} D_n^{j-1} \\ D_n^{j} \\ D_n^{j+1} \end{bmatrix} \\
p^{i}-\sigma_n^{i} &= \sum_{j=1}^{N}\begin{bmatrix} A_{ns}^{i(j-1)} & A_{ns}^{ij} & A_{ns}^{i(j+1)} \end{bmatrix}\begin{bmatrix} D_s^{j-1} \\ D_s^{j} \\ D_s^{j+1} \end{bmatrix} + \sum_{j=1}^{N}\begin{bmatrix} A_{nn}^{i(j-1)} & A_{nn}^{ij} & A_{nn}^{i(j+1)} \end{bmatrix}\begin{bmatrix} D_n^{j-1} \\ D_n^{j} \\ D_n^{j+1} \end{bmatrix}
\end{aligned} \tag{4.8}$$

The details of computing the influencing coefficients and assembling the matrix A^{ij} is given by Li et al. (2021a, 2021b)

The effectiveness of bedding layers influencing the hydraulic fracture height growth can be quantified through the change of the SIFs of the hydraulic fracture induced by the bedding layers (Kresse and Weng 2019). At the intersection between the hydraulic fracture and the horizontal bedding interfaces, the vertical hydraulic fracture width is influenced by the shear slippage of the beddings and the amount of change in the width is given by:

$$\sum_{j=1}^{N(HF)} A_{nn}^{ij} D_n^{j} = -\sum_{j=1}^{N(BL)} A_{ns}^{ij} D_s^{j} \tag{4.9}$$

where D_s^{j} are the shear displacement discontinuities of the bedding layers and the D_n^{j} is the change in the vertical hydraulic fracture width. Based on the linear elastic fracture mechanics, the change of SIFs of the hydraulic fracture induced by the bedding layers is quantified as:

$$K_I^{change} = -\frac{E^{'}}{4}\sqrt{\frac{\pi}{dl}}D_n^1 \tag{4.10}$$

where $E^{'}$ is the plane-strain modulus and is given by $E^{'} = E/(1-\upsilon^2)$, E and υ are the Young’s Modulus and the Poisson’s Ratio, $\overset{1}{D_n}$ is the change in width of the fracture tip element and dl is the length of the tip element. Therefore, the correction to the effective SIF of the hydraulic fracture is given by:

$$K_I^{eff} = K_I - K_I^{change} \tag{4.11}$$

The effective SIF is then substituted to obtain the equilibrium height with a given pressure.

4.4. A novel hydraulic fracture height model considering the impact of weak bedding planes

The whole simulation workflow is summarized in Figure 4.3. First of all, the target zones above and below the perforation depth are discretized respectively, each upper discretized layer depth represents the upper tip of the vertical hydraulic fracture and lower discretized layer depth represents the lower tip of the fracture, and together they form a hydraulic fracture height tip location pair. For each pair, the SIFs at both upper tip and lower tip are calculated using Equation 3. If any bedding layers are distributed between the upper tip and the lower tip, the “Effect of bedding layer interfaces” subroutine is called and the Equations 4-12 are solved, where the effective SIFs are updated. Then the SIFs are compared with the critical SIFs at both upper and lower tips simultaneously and a perforation pressure is to be found by equating SIFs to critical SIFs. By looping all the tip location pairs, we should have obtained two pressure matrix that governs the height of the vertical hydraulic fracture with any given perforation pressure. With a specific pressure or a series of pressures, we can find the corresponding hydraulic fracture tip locations by calling the "Find height tip locations" subroutine: starting from the closest lower tip location, find the closest upper tip location that makes the given pressure p larger than the computed p^{+}_{stable}, then check whether this pair also stabilizes the lower tip, if yes, the pair is the solution pair and the tip locations are the hydraulic fracture height locations (or interpolation is needed if the solution is between the discretized depths), if not, go to next closest lower tip location and repeat the above process until the stable solution pair is found. If no solution is found, the given pressure is overlarge and either upper bound or lower bound or both bounds are penetrated.

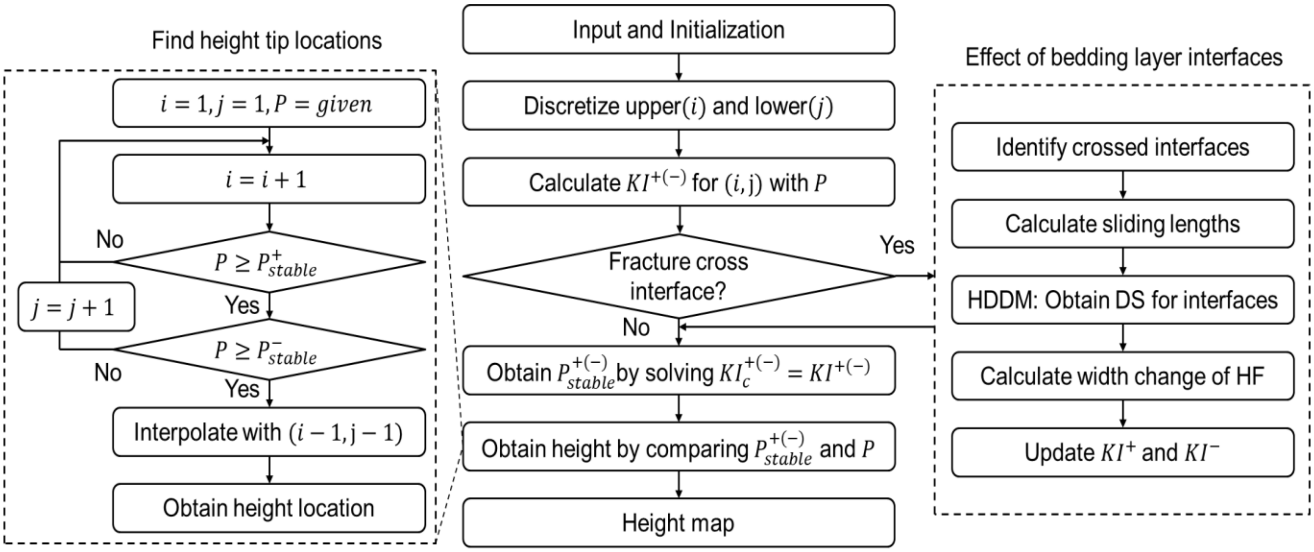

Figure 4.3 Numerical simulation workflow of the new hydraulic fracture height growth model considering the effect of bedding layers. (Reprinted from Li and Wu 2022b)

4.5. Model verification

Our model is validated against Liu and Valko’s (2018) result with a six-layer asymmetric problem. The thickness and the true vertical depth are given by Liu and Valko (2018), the minimum horizontal in-situ stress distribution is depicted here in Figure 4.4. In Figure 4.4a, the black line indicates the stress profile, the red-dash line indicates the perforation depth, and the red dot indicates the perforation point, which is located in the third layer. The mode I fracture toughness K_{Ic} of the rock layers are 2000 $psi\sqrt{inch}$ and are uniform for all layers. The other parameters are recorded in Table 2.1 . No bedding layers are considered. Our results of the hydraulic fracture tip locations against the injection pressure are presented in Figure 4.4b together with Liu and Valko’s results, illustrating that our results are in good agreement with their results. The results are validated against the commercial software MShale and FracPro as mentioned in their paper, and are also cross-validated by Mehrabi et al. (2021).

Table 4.1 Formation data for the verification study. (Reprinted from Li and Wu 2022b)

No. of Layer	Top Depth (ft)	Thickness (ft)	In-Situ Stress (psi)	Fracture Toughness (psi*√inch)	Perforation
1	8990	90	7150	2000	No
2	9080	90	7150	2000	No
3	9170	170	5700	2000	Yes
4	9340	40	7350	2000	No

5	9380	75	5800	2000	No
6	9455	195	8200	2000	No

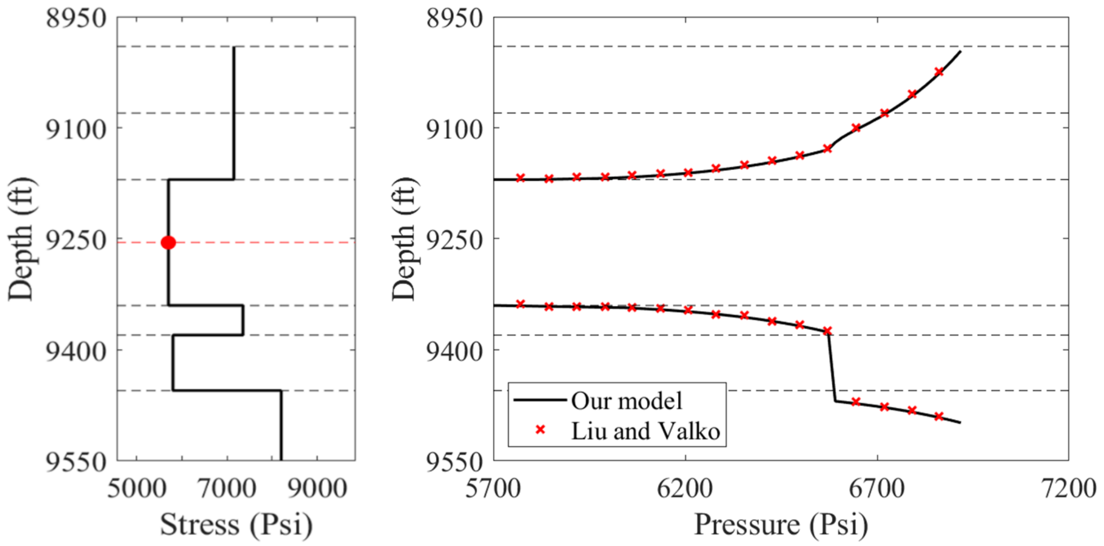

(a) (b)

Figure 4.4 Benchmark of our model against Liu and Valko's model. (a) the minimum horizontal in-situ stress profile as part of the input, (b) the hydraulic fracture tip locations against the injection pressure. (Reprinted from Li and Wu 2022b)

4.6. Field example: case studies in Permian Basin

In this section, the proposed hydraulic fracture height growth model is applied to a field example in Permian basin Wolfcamp formation. As one of the most prolific unconventional plays in the United States, the Permian Basin consists of three main basins, the Midland, Delaware, and Marfa basins. The Wolfcamp formation investigated in this study is located at the Midland Basin. The target interval is several hundred feet below the lower Spraberry and above the Strawn, and the stratigraphic layering is depicted proportionally to the thickness in Figure 4.6a (Ross et al. 2018). The pay zone ranges from the Wolfcamp A1 to the Wolfcamp C1 (totally 7 geological layers) and the well is landed in the Wolfcamp B2. The true vertical depth of each layer top and bottom locations and the thickness are recorded in Table 4.2. The minimum horizontal in-situ stress along the depth is presented in Figure 4.6b, and the mode I fracture toughness K_{Ic} of the rock layers are 2000 $psi\sqrt{inch}$ and are uniform for all layers, as shown in Figure 4.6c. The resolution of the stress profile along the depth is 1 ft and the total length of the interval is 916 ft, i.e., the total number of computational layers are 916. The Young's modulus and Poisson's Ratio are 3.0 MMpsi and 0.27, respectively and are both uniform for all layers. The laminations and bedding layers are observed at the Wolfcamp formation with the lithology ranging from silicon to limestones (Lascelles et al. 2017). The spacing between the bedding layers in thin laminations typically ranges from several feet. The mode II fracture toughness K_{IIc} of the bedding layers for the base case are set to be equal to the mode I fracture toughness of the rock and sensitivity analyses are then performed.

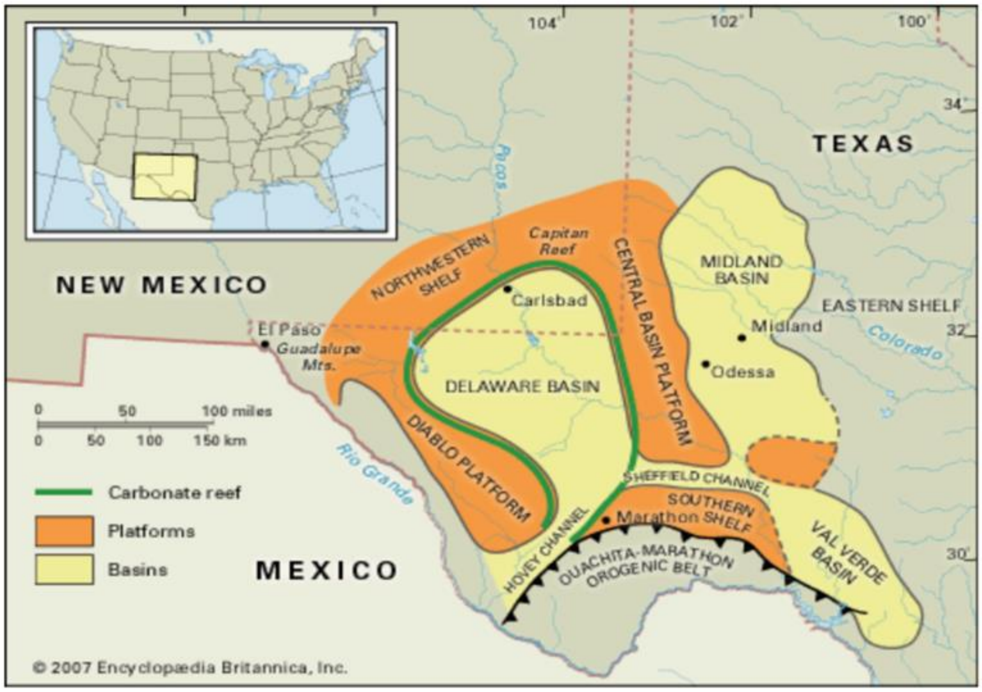

Figure 4.5 Geological description of the Permian basin Wolfcamp Formation. (Reprinted from Li and Wu 2022b)

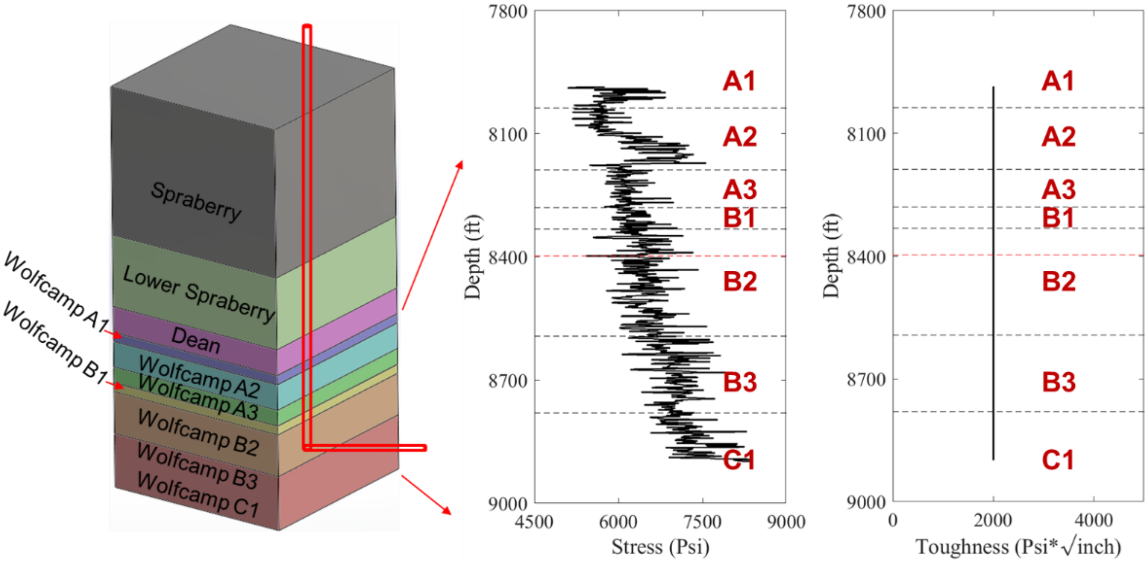

(a) (b) (c)

Figure 4.6 (a) Schematic representation of the Permian Basin stratigraphy (Adopted from Ross et al. 2018), (b) the minimum horizontal stress profile in the

pay zone, the red-dash line indicating the well landing depth, (c) the mode I fracture toughness profile in the pay zone. (Reprinted from Li and Wu 2022b)

Table 4.2 The true vertical depth, thickness, and the mode I fracture toughness of the formation layers. (Reprinted from Li and Wu 2022b)

Layer	Rock Formation	TVD Top (ft)	TVD Bottom (ft)	Thickness (ft)	Toughness (Psi*inch^0.5)
1	Wolfcamp A1	7984	8037	53	2000
2	Wolfcamp A2	8037	8188	151	2000
3	Wolfcamp A3	8188	8280	92	2000
4	Wolfcamp B1	8280	8332	52	2000
5	Wolfcamp B2	8332	8593	261	2000
6	Wolfcamp B3	8593	8780	187	2000
7	Wolfcamp C1	8780	8900	120	2000

Based on the above input information, the hydraulic fracture height growth without considering the effect of the bedding layers against the net injection pressure predicted by our model is presented in Figure 4.7. The well is located in Wolfcamp B2 and the TVD is 8398 ft. The hydraulic fracture tip locations are presented correspondingly, the curve above the perforation point represents the upper tip locations and the curve below the perforation point represents the lower tip locations against the net injection pressure. It is observed from the figure that the fracture height starts to grow when the net pressure gets larger than 800 psi and jumps both upward and downward after the net pressure reaches around 1100 psi. This can be attributed to the fact that the perforation layer is lightly bounded by the stress barriers as depicted in the Figure 4.6b. The hydraulic fracture upper tip penetrates the upper bound firstly when the net pressure reaches 1220 psi, and the lower tip reaches the lower bound when the net pressure reaches 1505 psi.

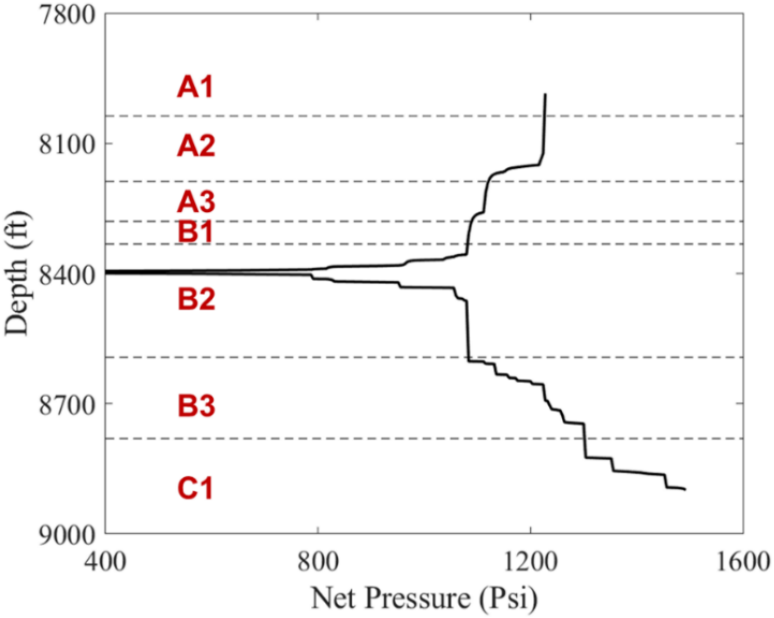

Figure 4.7 Hydraulic fracture height growth without considering the effect of the bedding layers against the net injection pressure. (Reprinted from Li and Wu 2022b)

The hydraulic fracture height growth considering the effect of the bedding layers is presented in Figure 4.8 together with the comparison with the height without the effect of the bedding layers. The spacing of the bedding layers in consideration is 9 ft, i.e., the total number of bedding layers within the whole interval is 100. The mode II fracture toughness K_{IIc} of the bedding layers is 2000 $psi\sqrt{inch}$. As indicated in Figure 4.8, the effectiveness of bedding layers on the hydraulic fracture height growth is obvious: given the same net injection pressure, the fracture height considering the effect of bedding layers is always smaller than that without the bedding layers; and similarly, to reach a same height, the case considering the effect of bedding layers requires larger net injection pressure. For most cases of the given net pressure, the difference between these two heights is generally less than 20%. However, in cases where the net pressure is equal to 1100 psi, the difference between these two heights is significant since the height without bedding layers already breakthrough the local barriers to the next layers while the height with effect of the bedding layers is still bounded by local barriers.

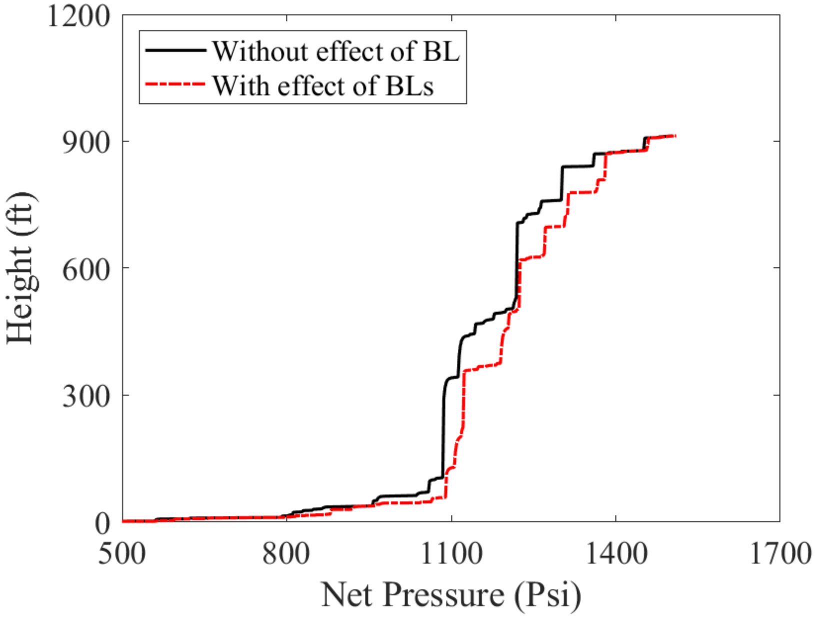

Figure 4.8 Comparison between the hydraulic fracture height with and without the effect of the bedding layers. (Reprinted from Li and Wu 2022b)

More details of the hydraulic fracture height growth and the corresponding bedding layers shear slippage are given in Figure 4.9 and Figure 4.10. Figure 4.9a shows the hydraulic fracture height without effect of bedding layers and Figure 4.9b shows the hydraulic fracture height and the corresponding bedding layers shear slippage length during the height propagation when the net pressure is 1160 psi. Instead of visualizing all

100 bedding layers which is a mass of dash lines, only parts of the bedding layers with spacing around 30 ft are visualized to keep the clarity of the figures. The hydraulic fracture height in Figure 4.9a is 474 ft while the height in Figure 4.9b is decreased to 382 ft, indicating that the height is reduced by 20% by considering the effect of the bedding layers. This is due to the fluid leaking off from the hydraulic fracture into the bedding layers and the energy loss during the shear slippage of the bedding layers. Similar results are also observed when the net pressure is 1300 psi, as shown in Figure 4.10a and Figure 4.10b. The fracture height without the effect of the bedding layers in Figure 4.10a is 840 ft while the height considering bedding layers in Figure 4.10b is 722 ft, indicating a 14% decrease. It is worthwhile to mention that the hydraulic fracture in Figure 4.10a has already reached the upper bound, as indicated in Figure 4.11c.

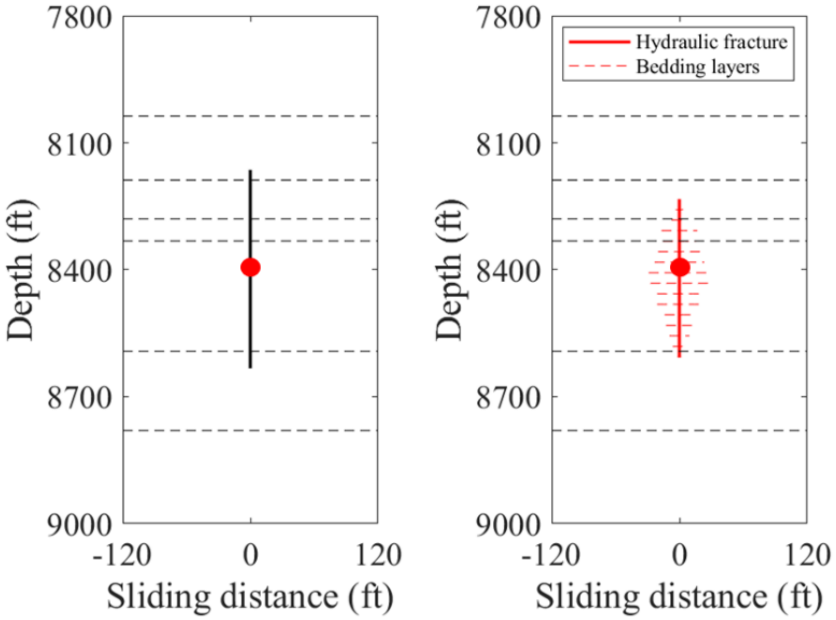

(a) (b)

Figure 4.9 Hydraulic fracture height and the bedding layer shear slippage length when net pressure is 1160 psi. (a) Hydraulic fracture height without the effect of

bedding layers, (b) Hydraulic fracture height and the bedding layer sliding length. (Reprinted from Li and Wu 2022b)

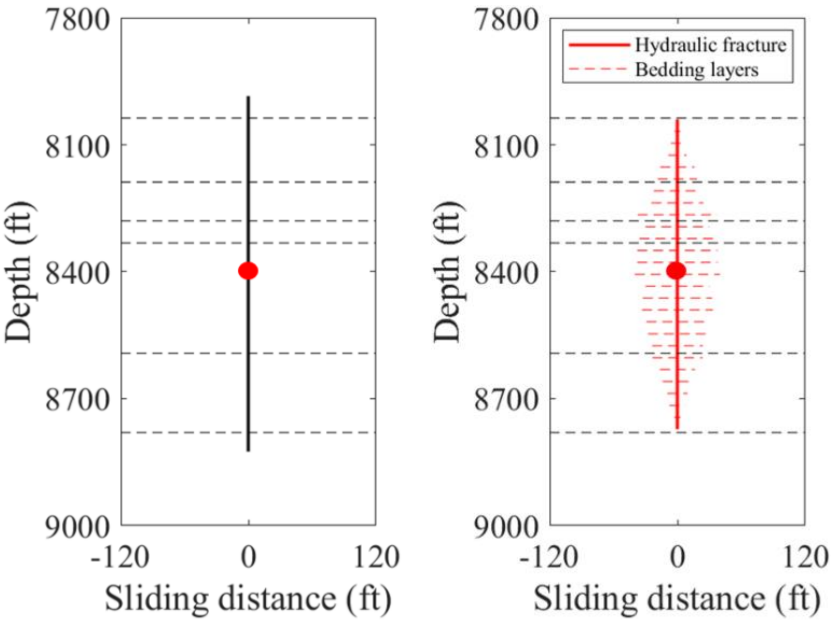

(a) (b)

Figure 4.10 Hydraulic fracture height and the bedding layer shear slippage length when net pressure is 1300 psi. (a) Hydraulic fracture height without the effect of bedding layers, (b) Hydraulic fracture height and the bedding layer sliding length. (Reprinted from Li and Wu 2022b)

Figure 4.11 displays the full hydraulic fracture profile including the hydraulic fracture height without effect of bedding layers (Figure 4.11a), and the hydraulic fracture height together with the bedding layers sliding length (Figure 4.11b), and the comparison of the hydraulic fracture tip locations between the case with and without the effect of bedding layers (Figure 4.11c). As indicated in Figure 4.11c, the hydraulic fracture upper tip reaching to the upper bound requires much smaller net injection pressure if no bedding layers are considered. As can be seen in Figure 4.11b, lateral sliding of the bedding layers occurs and has increased the fluid loss in the vertical hydraulic fracture as well as the energy loss. However, the net pressure needed to penetrate the lower bound is almost the same with and without considering the effect of bedding layers, this might be because the in-situ stress increases in the lower layers mitigate the effect of the bedding layers.

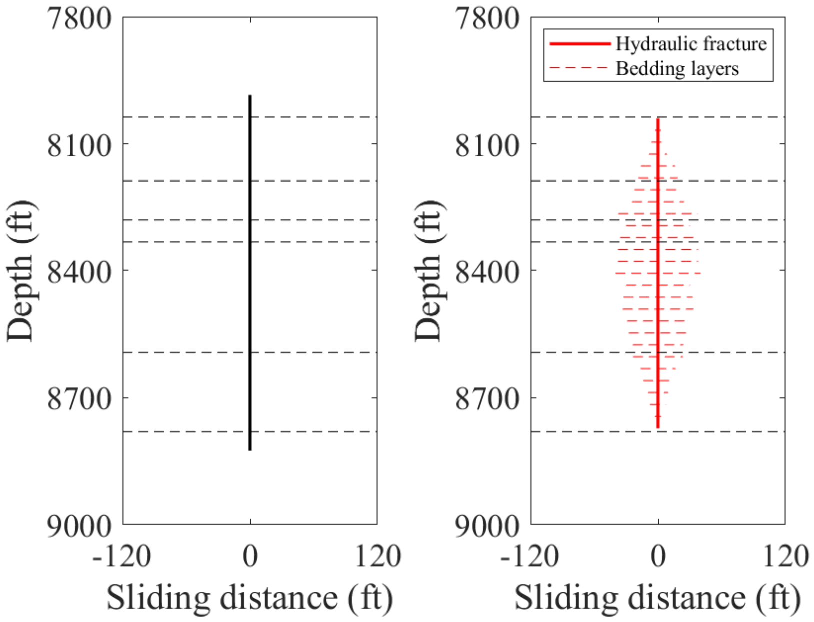

(a) (b)

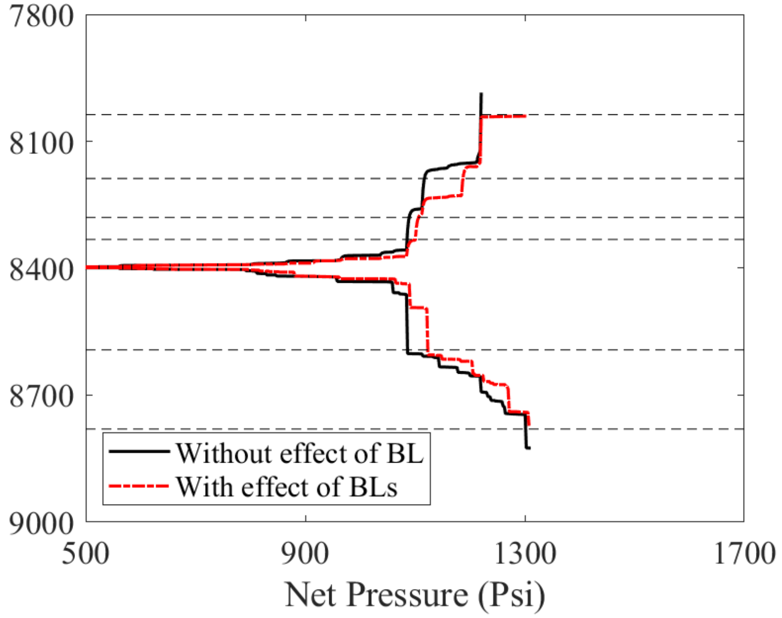

(c)

Figure 4.11 Full hydraulic fracture profile. (a) hydraulic fracture height without effect of bedding layers, (b) hydraulic fracture height and the bedding layers sliding length, (c) the comparison of the hydraulic fracture tip locations between the case with and without the effect of bedding layers. (Reprinted from Li and Wu 2022b)

4.6.1. Effect of density of bedding planes

The average spacing between the bedding layers in the thin laminations typically ranges from several inches to several feet. In this section, the effect of the average spacing between the bedding layers, which is referred to the “bedding layer density”, is investigated. Two more numerical cases with the bedding layers spacing 4.5 ft and 3 ft are simulated. The rest of the parameters are maintained the same as the previous 9-ft case. The results are presented in comparison with the no-bedding-layer case. Figure 4.12 shows the full hydraulic fracture height evolution map against the net injection pressure of the four cases: without the effect of bedding layers, with the bedding layer spacing 9 ft, with the bedding layer spacing 4.5 ft, and with the bedding layer spacing 3 ft. Figure 4.13 shows the corresponding hydraulic fracture tip locations. These two figures lead to the following findings: when the density of the bedding layer increases, the effect of the bedding layers on the hydraulic fracture height gets more significant and the hydraulic fracture height under the same net injection pressure is decreased; the net pressure required to penetrate both upper bound and lower bound is increased as the increase of the bedding layer density. This is because denser bedding layers have larger impact on the effective fracture toughness of the hydraulic fracture and more energy is required to break through the rocks, therefore slowing down the propagation of the hydraulic fracture height.

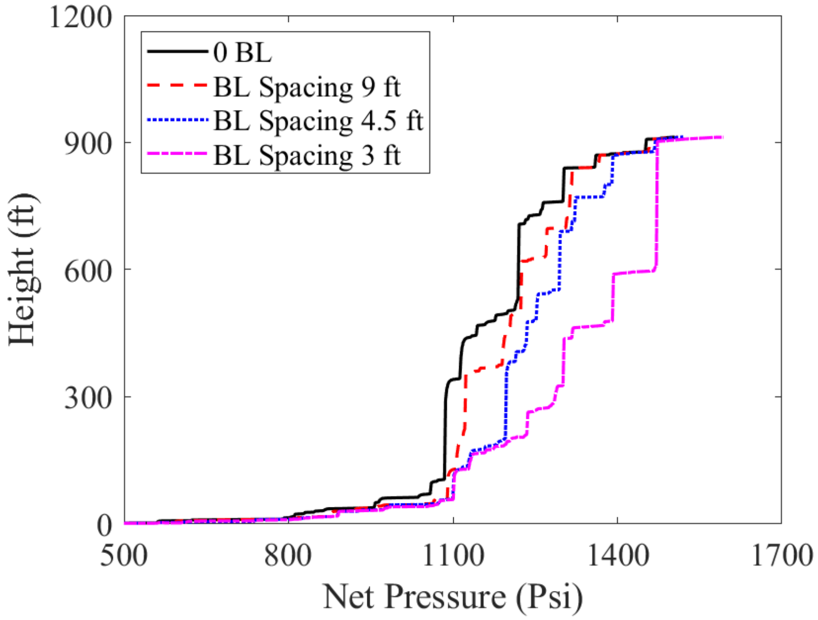

Figure 4.12 Full hydraulic fracture height evolution map against the net injection pressure. (Reprinted from Li and Wu 2022b)

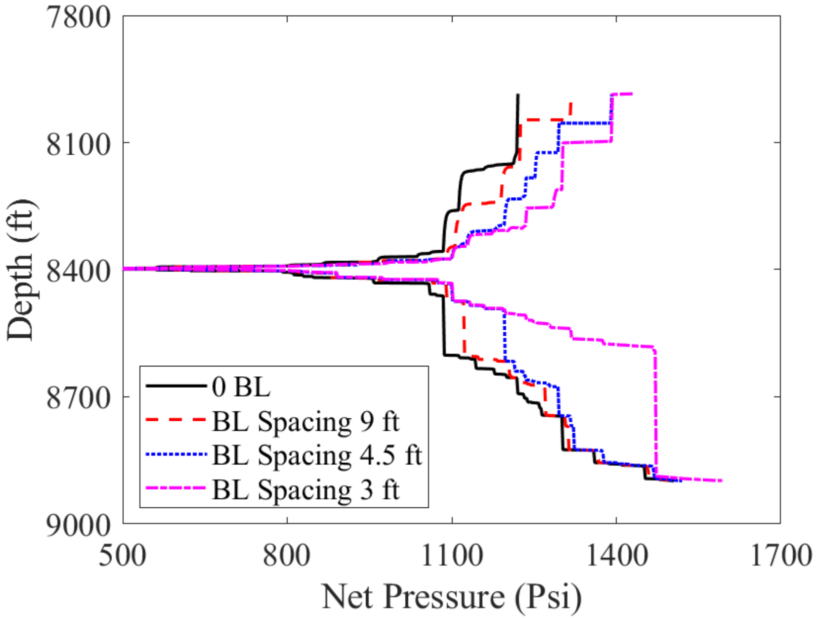

Figure 4.13 Hydraulic fracture height tip evolution against the net injection pressure. (Reprinted from Li and Wu 2022b)

Figure 4.14 presents the hydraulic fracture height along with shear sliding distance of the horizontal bedding layers at the net injection pressure 1300 psi of the four cases. The comparison between the slippage of the visualized bedding layers shows the effectiveness of the bedding layers and further demonstrate the reason behind the hydraulic fracture height drop caused by the bedding layers. The hydraulic fracture height without effect of bedding layers (Figure 4.14a) is 840 ft, and the hydraulic fracture height with effect of bedding layers at the spacing of 9 ft, 4.5 ft, and 3 ft are 722 ft, 692 ft, and 326 ft, respectively. With the effect of bedding layers, the hydraulic fracture height has dropped by 14%, 18%, 61% with regard to different densities. As indicated in Figure 4.14b, Figure 4.14c, and Figure 4.14d, in closer spacing case, more shear slippage is observed, and the hydraulic fracture height is contained in a shorter zone with the same net pressure since larger part of the energy is consumed in the bedding layers during the hydraulic fracture propagation.

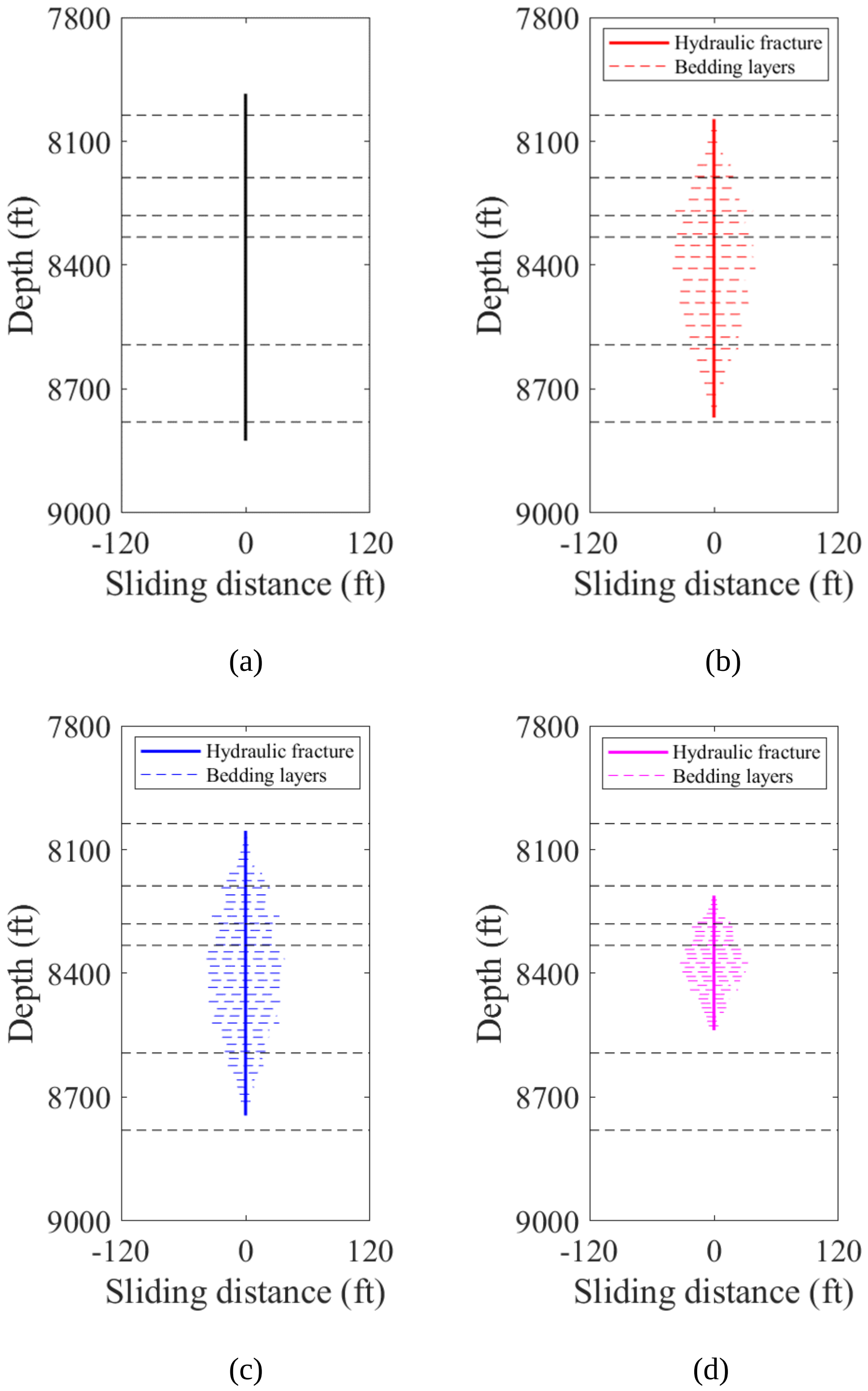

(a)

(b)

(c)

(d)

Figure 4.14 Hydraulic fracture height and the bedding layer shear slippage length when the net pressure is 1300 psi. (a) case without bedding layer, (b) bedding layer spacing 9 ft, (c) bedding layer spacing 4.5 ft, (d) bedding layer spacing 3 ft. (Reprinted from Li and Wu 2022b)

4.6.2. Effect of fracture toughness of bedding planes

The mode II fracture toughness of the bedding layers is another critical factor that affect the shear slippage of the bedding layers and the consequent effectiveness on the hydraulic fracture height growth. Accurate measurement of the mode II fracture toughness can be challenging due to complex downhole conditions and heterogeneity. This section investigates the effect of the mode II fracture toughness of the bedding layers on the hydraulic fracture height. Three cases with the mode II fracture toughness (2000, 5000, and 10000 $psi\sqrt{inch}$) are presented in comparison with the case without the bedding layers. Figure 4.15 and Figure 4.16 present the hydraulic fracture full height and the tip location evolution against the net injection pressure. From the two figures it is observed that larger magnitude of the mode II fracture toughness of the bedding layers puts more resistance on the hydraulic fracture height propagation. Both upper and lower tips propagation of the hydraulic fracture are slowed down as the increase of the fracture toughness of the bedding layers. Additionally, the net pressure required to penetrate the pay zone is increased with larger fracture toughness.

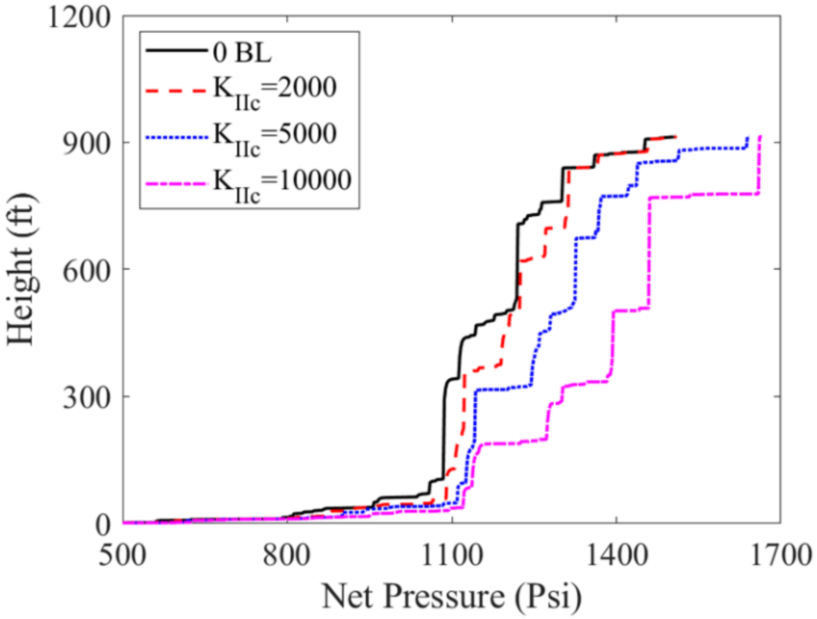

Figure 4.15 Full hydraulic fracture height evolution map against the net injection pressure. (Reprinted from Li and Wu 2022b)

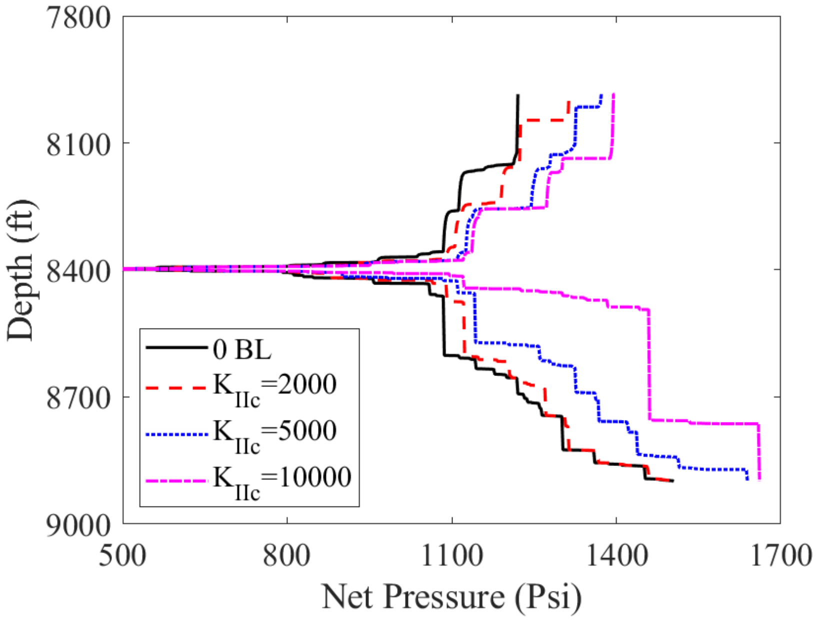

Figure 4.16 Hydraulic fracture height tip evolution against the net injection pressure. (Reprinted from Li and Wu 2022b)

The change of the shear slippage distance of the bedding layers by different magnitude of the mode II fracture toughness K_{IIc}^{intf} is visualized when net pressure is 1300 psi and presented in Figure 4.17. In this case, the model I fracture toughness of the rock properties is still 2000 $psi\sqrt{inch}$. For a large mode II fracture toughness, the horizontal bedding planes are still able to have shear failure due to stress conditions. As shown in the figure, the hydraulic fracture height without effect of bedding layers (Figure 4.17) is 840 ft, and the hydraulic fracture height with effect of bedding layers (2000, 5000, 10000 $psi\sqrt{inch}$) are 722 ft, 504 ft, and 324 ft, respectively. With the effect of bedding layers, the hydraulic fracture height has dropped by 14%, 40%, 61% with regard to different fracture toughness. As indicated in Figure 4.17b, Figure 4.17c, and Figure 4.17d, larger shear fracture toughness results in larger maximum shear slippage length of the bedding layers, and therefore larger energy loss in the bedding layer slippage, which reduces the fracture height significantly.

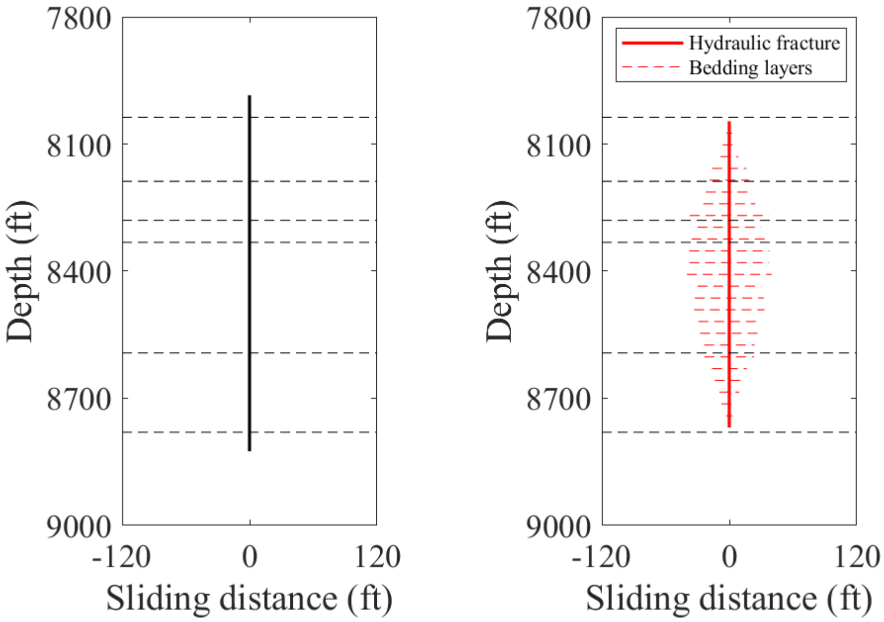

(a) (b)

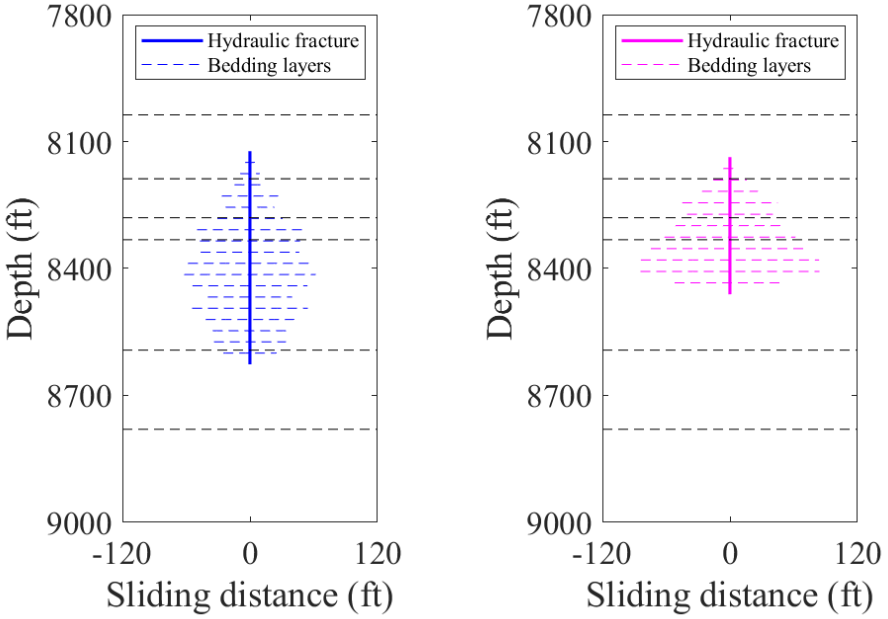

(c) (d)

Figure 4.17 Hydraulic fracture height and the bedding layer shear slippage length when the net pressure is 1300 psi. (a) case without bedding layer, (b) bedding layer with $K_{IIc}^{intf} = 2000\ psi\sqrt{inch}$, (c) bedding layer with $K_{IIc}^{intf} = 2000\ psi\sqrt{inch}$, (d) bedding layer with $K_{IIc}^{intf} = 2000\ psi\sqrt{inch}$.(Reprinted from Li and Wu 2022b)

4.6.3. Effect of landing depth

This section investigates the effect of the landing depth on the injection pressure and the hydraulic fracture height growth. Four landing depths located in Wolfcamp A3, B1, B2, and B3 are simulated, with B2 the base case. The hydraulic fracture height evolution against the net injection pressure is presented in Figure 4.18b. All four cases show completely different growth profiles but follow the similar trend, and they have the similar turning point when the hydraulic fracture height is around 400 ft and around 800 ft. This is because that local stress barriers at the top of A3 and at the middle of B3 can be observed from the stress profile (Figure 4.18a). The net pressure required to penetrate the whole pay zone for B3 is much smaller than that of A3 since the B3 is the high-stress layer and the A3 is the relatively low-stress layer. In low-stress layer, larger net pressure is required to penetrate the high-stress layer and vice versa.

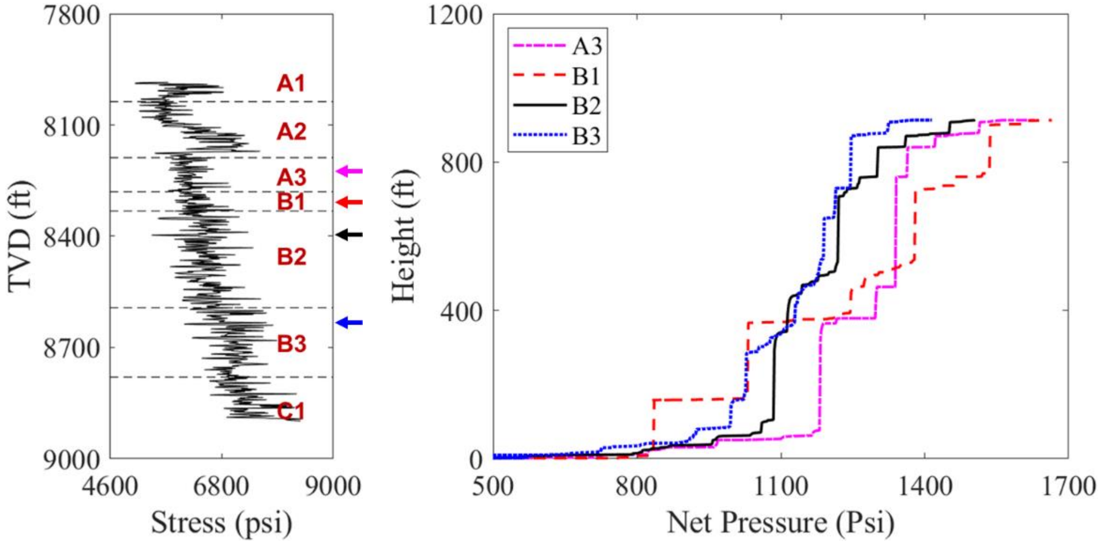

(a) (b)

Figure 4.18 Hydraulic fracture height growth against the net pressure by different landing depth. (a) the stress profile with arrows indicating the landing depth, (b) hydraulic fracture height map. (Reprinted from Li and Wu 2022b)

Figure 4.19 records the fracture height growth along with the bedding layer shear slippage of these four different perforation depths at the net pressure of 1250 psi. The hydraulic fracture heights of the four cases are 379 ft, 460 ft, 719 ft, and 870 ft, respectively. The in-situ stress in the deeper layer, for example B3, is larger than A3 and given the same net pressure, the hydraulic fracture height will be larger. Except from the full height, the tip locations can also be different from each other with different perforation depths. The fracture height growing upward and downward is most likely asymmetric (as indicated in Figs. 20a, 20b, and 20d). Through the simulation we are able to perform the well landing depth optimization, including locating the best perforation depth that keeps the hydraulic fracture penetrate the pay zone simultaneously at upper and lower bounds. In general, the well landed in a high-stress layer requires smaller net pressure for fracture height growth and larger net pressure if landed in a low-stress layer.

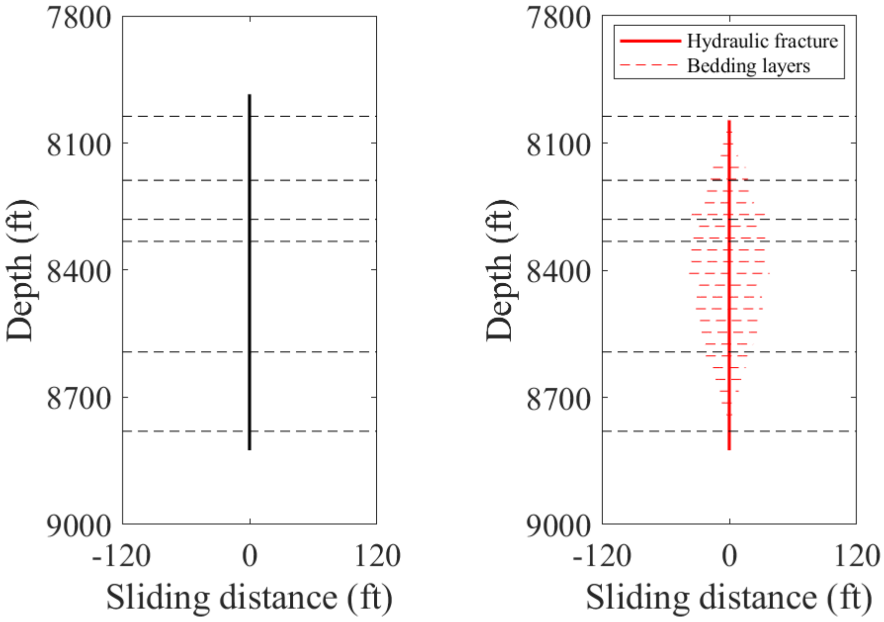

(a) (b)

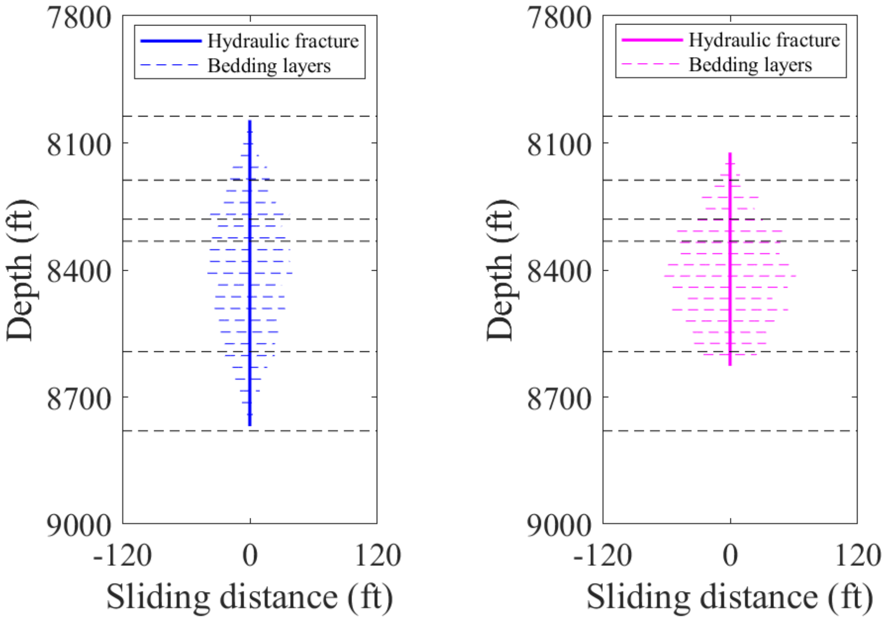

(c) (d)

Figure 4.19 Hydraulic fracture height and the bedding layer shear slippage length when the net pressure is 1250 psi. (a) perforation at A3, (b) perforation at B1, (c) perforation at B2, (d) perforation at B3. (Reprinted from Li and Wu 2022b)

4.6.4. Effect of stress variation

It has been recognized and evidenced by numerous field observations, experimental efforts, and numerical studies that the minimum horizontal in-situ stress difference between layers plays a dominant role in the hydraulic fracture height containment in most situations. The bedding layers are more likely to show significance in low-stress-variation formations. This section investigates the influence of the in-situ stress variation and the bedding layers. Figure 4.20 show three different stress profiles: Figure 4.20b is the stress profile used in the base case and is originally from the field, the red dash curve is the interpolated trend line of the stress along the depth. Figure 4.20a is the low-stress-variation case where we maintain the trend line (the red dash line) the same as the base case but decrease the distance from the data points to the trend line by half. Figure 4.20c is the high-stress-variation case where we maintain the trend line (the red dash line) the same as the base case but double the distance from the data points to the trend line. The hydraulic fracture height growth with and without the effect of the bedding layers are compared and presented in Figure 4.21. The bedding layer density is 9 ft and the mode II fracture toughness is 2000 $psi\sqrt{inch}$.

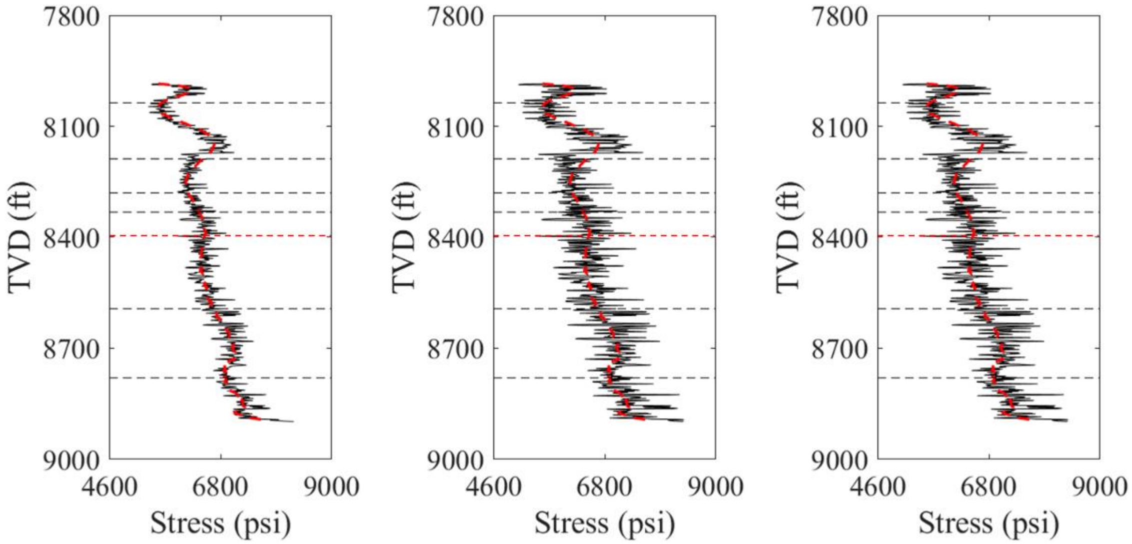

Figure 4.20 Minimum horizontal in-situ stress profile in the pay zone. (a) low-stress-variation case, (b) base case, (c) high-stress-variation case. (Reprinted from Li and Wu 2022b)

As shown in the Figure 4.21, the hydraulic fracture height maps are obviously distinguished into three groups by the stress-variation magnitude, indicating that the stress difference is playing a dominant role in governing the hydraulic fracture height growth. The black lines (solid and dash) represent the low-stress-variation case, the red lines represent the base case, and the blue lines represent the high-stress-variation case. It is also observed that all the three comparison of the height growth with and without the bedding layers have observable difference, with the largest difference observed in the low-stress-variation case and smallest difference observed in the high-stress-variation case. To reach the same hydraulic fracture height, as the comparison between the black-solid and black-dash lines indicates, the net pressure required has increased by more than 40% if considering the effect of bedding layers in low-stress-variation case; while in the base case as indicated by the red-solid and red-dash lines, the net pressure is generally increased by around 10%; while in the high-stress-variation case as indicated by the blue-solid and blue-dash lines, the net pressure is generally increased by less than 5%. This can be concluded that the effect of bedding layers on the hydraulic fracture height containment is significantly more important in the low-stress-variation formation than that in the high-stress-variation formation, which has a good agreement with both the experimental results (Anderson 1981; Teufel and Clark 1984) and the field observations (Warpinski et al. 1981; Daneshy et al. 2004; Daneshy 2009).

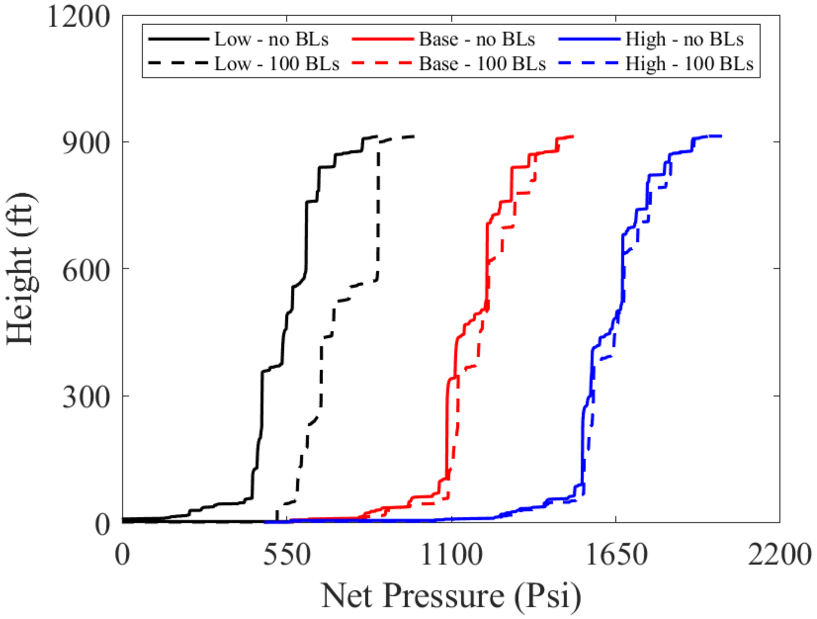

Figure 4.21 Comparison of the full hydraulic fracture growth map between cases with and without the effect of bedding layers under different stress-variation cases. (Reprinted from Li and Wu 2022b)

4.7. Conclusions

In this chapter, a non-intrusive hydraulic fracture height growth model was developed considering the combined effect of geo-mechanical properties and bedding interfaces. The hydraulic fracture height containment by the geo-mechanical properties are controlled by the linear elastic fracture mechanics simultaneously at both upper and lower fracture tips, meanwhile, the impacts of the bedding interfaces are rigorously quantified through coupled fluid flow and rock mechanical modeling. The energy loss during the shear slippage propagation in the close-spacing bedding interfaces induced by the hydraulic fracture obviously slows down the height propagation of the vertical fracture. The simulation shows that the minimum in-situ stress difference between different formation layers plays a dominant part in containing the hydraulic fracture height with few bedding interfaces. However, the fracture height propagation is considerably hindered with existence of multiple close-spacing bedding interfaces. In formations with low in-situ stress variation between layers, the weak horizontal bedding interfaces could play a significant role in the hydraulic fracture height growth and containment. The non-intrusive model would be then incorporated in any pseudo-3D hydraulic fracture propagation simulator in the following chapter and makes it possible for pseudo-3D hydraulic fracture simulator to quantitatively consider the combined effect of geo-mechanical properties and weak bedding interfaces on the hydraulic fracture height growth and containment.

5. HYDRAULIC FRACTURE PROPAGATION CONSIDERING THE EFFECT OF WEAK BEDDING PLANES*

5.1. Introduction

Weak interfaces are widely distributed in the unconventional reservoirs. Both field observations and the laboratory experiments have demonstrated that hydraulic fracture propagation can be affected by the weak interfaces. Numerical studies have been performed to investigate the interaction between the weak interfaces and the hydraulic fracture, but few hydraulic fracture simulators have incorporated the mechanism of the weak interfaces in the hydraulic fracture propagation. This chapter presents an efficient comprehensive hydraulic fracture height growth model incorporating in a hydraulic fracture simulator based on a simplified 3D displacement discontinuity method and investigates the impact of the weak interfaces on the hydraulic fracture geometry and the width distribution.

The comprehensive hydraulic fracture height growth model considers not only the conventional impact factors that controls the fracture height, but also the influence of the horizontal weak interfaces. The interaction between the weak interfaces and the hydraulic fracture is modeled by an efficient 2D higher order displacement discontinuity method and the effectiveness on the hydraulic fracture height is quantified by correcting the stress intensity factors at the hydraulic fracture tips. This model is non-intrusive and is

---

* Part of this chapter is reprinted with permission from "Impact of Horizontal Weak Interfaces on the Hydraulic Fracturing: from Height Growth to Lateral Propagation" by Li, J. and Wu, K., 2022, SPE/AAPG/SEG Unconventional Resources Technology Conference. Copyright [2022] by Society of Petroleum Engineers.

incorporated into an in-house cell-based P3D hydraulic fracture simulator, which uses plane strain deformation in each vertical cross-section coupled with a 2D fluid flow.

Numerical examples are performed based on a Permian Basin Wolfcamp shale formation to study the impact of the weak interfaces on the fracture propagation and the final geometry. Results show that the weak interfaces have considerable impact on the fracture height, lateral length, and width distribution. With the existence of the weak interfaces, the hydraulic fracture height is shortened vertically, which results in a longer fracture lateral length, together with a reduction of the overall width values. Sensitivity analysis shows that the spacing between the weak interfaces and interfacial shear toughness have considerable impact on the fracture geometry and width values. In multi-fracture propagation case, the impact of the weak interfaces on the outer fractures results in a reduction in average height and overall width distribution, and an increase of the lateral length. For inner fractures, the impact of weak interfaces varies by the cluster spacing.

The proposed workflow effectively captures the mechanism of the horizontal weak interfaces on the hydraulic fracture height growth and the lateral propagation. The numerical studies provide more understanding on the fracture propagation in the laminated shale reservoirs. The new P3D hydraulic fracture simulator can be used as an effective tool for fracturing job design in shale formations.

5.2. Fracture height growth module

The key physical problems underlying the fluid-driven hydraulic fracture propagation includes rock deformation, fluid flow in the fractures, and fluid/proppant distribution among clusters, which are tightly coupled with each other. For a shale formation that consists of horizontal weak interfaces and potentially shear slippage, the rock deformation problem becomes fully 3D and generally requires a fully 3D fracture propagation model, which is over computationally intensive. An alternative way is to develop a comprehensive hydraulic fracture height module that captures the mechanism of the horizontal interface shear slippage and incorporate the height module in the P3D model.

The P3D model assumes that the vertical section of the hydraulic fracture is decoupled in the sense that the mechanical deformation of each vertical section is independent of its neighbors and satisfies the plane strain conditions (Mack and Warpinsky, 2000; Adachi et al., 2007). Another assumption is that the pressure gradient in the vertical direction due to the fluid flow is negligible and hence the fluid pressure in the vertical direction is hydrostatic. Based on these assumptions, a stable hydraulic fracture vertical tip positions and the corresponding width profile can be determined by matching the stress intensity factors at the fracture upper and lower tips to the fracture toughness in the layers that contain the fracture upper and lower tips simultaneously. In a multi-layered formation where the horizontal in-situ stress is piece-wise constant, the relations between the stress intensity factors and the fracture tips as well as fracture width are given by Mack and Warpinskin (2000):

$$\begin{aligned} K_I^{upper} &= \sqrt{\frac{\pi h_f}{2}}\left[\rho g\left(h_{perf}-\frac{3h_f}{4}\right)+p_{perf}-\sigma_n\right] \\ &+\sqrt{\frac{2}{\pi h_f}}\sum_{i=1}^{n-1}\left(\sigma_{i+1}-\sigma_i\right)\left[\frac{h_f}{2}\cos^{-1}\left(\frac{h_f-2h_i}{h_f}\right)-\sqrt{h_f(h_f-h_i)}\right] \end{aligned} \tag{5.1}$$

$$\begin{aligned} K_I^{lower} &= \sqrt{\frac{\pi h_f}{2}}\left[\rho g\left(h_{perf}-\frac{h_f}{4}\right)+p_{perf}-\sigma_n\right] \\ &+\sqrt{\frac{2}{\pi h_f}}\sum_{i=1}^{n-1}\left(\sigma_{i+1}-\sigma_i\right)\left[\frac{h_f}{2}\cos^{-1}\left(\frac{h_f-2h_i}{h_f}\right)+\sqrt{h_f(h_f-h_i)}\right] \end{aligned} \tag{5.2}$$

and,

$$\begin{aligned} w(z) &= \frac{4}{E'}\left[\rho g\left(h_{perf}-\frac{h_f}{4}-\frac{z}{2}\right)+p_{perf}-\sigma_n\right]\sqrt{z(h_f-z)} \\ &+\frac{4}{\pi E'}\sum_{i=1}^{n-1}\left(\sigma_{i+1}-\sigma_i\right)\left[(h_i-z)\cosh^{-1}\frac{z\left(\frac{h_f-2h_i}{h_f}\right)+h_i}{\left|h_i-z\right|}+\sqrt{z(h_f-z)}\cos^{-1}\left(\frac{h_f-2h_i}{h_f}\right)\right] \end{aligned} \tag{5.3}$$

where E' is the plane-strain elastic modulus of the rock, h_{perf} is the perforation depth measured from the fracture lower tip, p_{perf} is the fluid pressure at the perforation depth, σ_i and h_i are the minimum in-situ stress and the distance from the i th layer (counted from upper tip) to the fracture lower tip.

At the equilibrium state, the equilibrium tip status of the interface shear slippage can be obtained by assuming that the stress intensity factors are equal to the critical shear fracture toughness (Chuprakov and Prioul, 2005). Applying the fracture straightening concept (Weng et al. 2018), the stress intensity factor can be expressed by:

$$K_I^{str} = \sqrt{\frac{1}{\pi h_f^{str}}} \int_{-h_f^{str}}^{h_f^{str}-d_s} \left| p(y) - \sigma(y) \right| \sqrt{\frac{h_f^{str}+y}{h_f^{str}-y}} dy + \sqrt{\frac{1}{\pi h_f^{str}}} \int_{h_f^{str}-d_s}^{h_f^{str}} \left| p_{str} - \sigma_v \right| \sqrt{\frac{h_f^{str}+y}{h_f^{str}-y}} dy \tag{5.4}$$

where h_f^{str} is the effective straightened hydraulic fracture half height, d_s is the distance from the horizontal interfacial shear slippage tip to the hydraulic fracture, i.e., half of total shearing length, σ_v is the vertical in-situ stress acting on the weak interfaces.

The opening and the shear displacement discontinuities of the horizontal interfaces can be calculated through an elasticity solution for the stress and displacements relationship which is expressed by (Shou, 1993):

$$\begin{aligned} &\sigma_{jk}(\omega) = \int_S E_{ijk}(\omega, \xi) \Delta u_i(\xi) dS(\xi) \\ &\Delta u_i = u_i^- - u_i^+ \end{aligned} \tag{5.5}$$

where $\sigma_{jk}(\omega)$ and $\Delta u_i(\xi)$ represent the stress components and the displacement components at a point ω, respectively, $E_{ijk}(\omega, \xi)$ is the tensor field that represents the influences of a concentrated force at point ω on displacements at point ξ. Given stress conditions, the displacement components can be calculated using the displacement discontinuity methods.

Although the DDM has the advantages of being both efficient and accurate in handling the rock deformation problems, it has some shortcomings in dealing with closely-spaced horizontal interfaces in laminated shale formations (Li et al. 2021). Dozens of the horizontal interfaces are closely distributed along the vertical hydraulic fracture and the stress shadow effect requires that fine computation gridding must be used to obtain accurate solution, which costs intensive computational time. An efficient 2D higher order displacement discontinuity method (HDDM) with joint elements proposed by Li et al. (2021) provides a reliable solution to the closely-spaced fractured problems. The efficient HDDM adopts quadratic interpolation of the displacement discontinuities on each fracture-segment patch which is composed of three fracture segments. In this way, the discretized form of the Equation (5.5) is given by Equation (5.6). The derivation details of the method are referred to Shou (1993), the verifications of the method are referred to Behnia et al. (2015) and Li et al. (2021).

$$\begin{aligned}
{}^{i}\sigma_s &= \sum_{j=1}^{N} \begin{bmatrix} {}^{i(j-1)}A_{ss} & {}^{ij}A_{ss} & {}^{i(j+1)}A_{ss} \end{bmatrix} \begin{bmatrix} {}^{j-1}D_s \\ {}^{j}D_s \\ {}^{j+1}D_s \end{bmatrix} + \sum_{j=1}^{N} \begin{bmatrix} {}^{i(j-1)}A_{sn} & {}^{ij}A_{sn} & {}^{i(j+1)}A_{sn} \end{bmatrix} \begin{bmatrix} {}^{j-1}D_n \\ {}^{j}D_n \\ {}^{j+1}D_n \end{bmatrix} \\
{}^{i}p - {}^{i}\sigma_n &= \sum_{j=1}^{N} \begin{bmatrix} {}^{i(j-1)}A_{ns} & {}^{ij}A_{ns} & {}^{i(j+1)}A_{ns} \end{bmatrix} \begin{bmatrix} {}^{j-1}D_s \\ {}^{j}D_s \\ {}^{j+1}D_s \end{bmatrix} + \sum_{j=1}^{N} \begin{bmatrix} {}^{i(j-1)}A_{nn} & {}^{ij}A_{nn} & {}^{i(j+1)}A_{nn} \end{bmatrix} \begin{bmatrix} {}^{j-1}D_n \\ {}^{j}D_n \\ {}^{j+1}D_n \end{bmatrix}
\end{aligned} \tag{5.6}$$

The quantitative impact of horizontal interfaces on the hydraulic fracture height growth can be modeled through the change of the stress intensity factors of the hydraulic fracture tip locations (Kresse and Weng 2019). Upon interaction, the fracturing-induced shear slippage in the horizontal interfaces results in a reduction of the vertical hydraulic fracture width at the intersection point, which consequently changes the stress intensity factors of the hydraulic fracture. Based on the linear elastic fracture mechanics, the change of the stress intensity factors is given by Equation (5.7):

$$K_I^{change} = -\frac{E^{'}}{4}\sqrt{\frac{\pi}{dl}}D_n^1 \tag{5.7}$$

where D_n^1 is the change in width of the fracture tip element calculated from Equation (5.8) , dl is the length of the tip element

$$\sum_{j=1}^{N(HF)} A_{nn}^{ij} D_n^{j} = -\sum_{j=1}^{N(BL)} A_{ns}^{ij} D_s^{j} \tag{5.8}$$

The effective stress intensity factors are therefore obtained by subtracting the changes induced by the horizontal shear slippage.

The new effective stress intensity factors are used to compare with Equation (5.1) and Equation (5.2) to determine the equilibrium hydraulic fracture tip locations. In the target zone, the intervals above and below the perforation depth are discretized respectively, each upper discretized layer depth represents the potential upper tip of the vertical hydraulic fracture and lower discretized layer depth represents the potential lower tip of the fracture, and together they form a hydraulic fracture height tip location pair. For a given pressure, starting from the nearest lower/upper tip location, stress intensity factor or the effective stress intensity factor (when the vertical hydraulic fracture crosses a horizontal weak interface) is computed based on the linear elastic fracture mechanics. By comparing the stress intensity factors at both upper and lower tips with the fracture toughness of the layers where the fracture tips are located, the equilibrium hydraulic fracture tip locations can be found when these two pairs of two parameters are equal simultaneously.

5.3. Incorporation of the new hydraulic fracture height module into P3D fracture propagation simulator

The above hydraulic fracture height growth module is incorporated into a hydraulic fracture propagation model developed by Wu (2014). The model is based on a Simplified Three-Dimensional Displacement Discontinuity Method (S3D DDM) and is able to simulate complex hydraulic fracture propagation in unconventional reservoirs. The model couples linear-elastic rock deformation with non-linear fluid flow in fractures and the horizontal wellbore (Wu and Olson 2015), which captures the key physical processes during multiple-fracture propagation including the fracture opening, propagation and stress-shadow effects.

The elastic rock deformation equations are solved by the S3D DDM. A 3D correction factor derived by Olson (2004) is used to account for the 3D fracture geometry. Consider a typical discretized fracture element with normal and shear stress boundary conditions specified, we can determine the normal and shear displacement discontinuities, respectively, at each of the total fracture elements by solving a linear system of equations given by:

$$\begin{aligned} \sigma_s^i &= \sum_{j=1}^{N} \left(G^{ij} A_{ss}^{ij} D_s^j + G^{ij} A_{sn}^{ij} D_n^j \right) \\ \sigma_n^i &= \sum_{j=1}^{N} \left(G^{ij} A_{ns}^{ij} D_s^j + G^{ij} A_{nn}^{ij} D_n^j \right) \end{aligned} \tag{5.9}$$

where σ_s and σ_n are the shear and normal stresses on the fracture segments, D_s and D_n are the shear and normal displacement discontinuities of the fracture segments, A_{ss}^{ij}, A_{sn}^{ij}, A_{ns}^{ij}, and A_{nn}^{ij} are the plane-strain elastic influencing coefficients between the fracture segments i and j. A detailed derivation of A is referred to Crouch and Starfield (1983). G^{ij} is the 3D correction factor which is referred to Olson (2014).

Fluid flow in the fracture propagation model consists of two parts which are fluid flow in the fracture segments and the fluid flow in the horizontal wellbore between perforation locations. Fluid flow in the fracture segments is described by the Navier-Stokes equations of fluid mechanics (Schlichting 1968). The 3D equations can be simplified by assuming that the pressure gradient along the fracture width is uniform. To improve the convergence stability without losing too much accuracy, the flow-rate gradient along the fracture is ignored. Fluid flow in the wellbore is analogous to the electric current flow through an electrical circuit network. Kirchhoff's first and second laws are applied to determine the dynamic flow rate distribution of multiple fractures (Siriwardane and Layne 1991). According to Kirchhoff's second law, the pressure in the wellbore heel is the summation of the pressure drop due to the wellbore friction, pressure drop due to the perforation friction, and the pressure in the first element of the fracture segment (Elbel et al. 1992). For the whole computational fluid-flow system, the material balance is satisfied when the total volume of the fluid pumped during the injection time is equal to the summation of the fluid volume in the fracture segments and the fluid volume leaking into the neighboring rock medium. The fluid leaking off is calculated by the Carter leakoff model (Carter 1957).

The fluid flow and the rock deformation parts are tightly coupled with each other since both the pressure distribution and the fracture displacement discontinuities are unknowns to be solved in both parts of equations. The Picard coupling (Li 1991; Adachi et al. 2007) is adopted to numerically couple the rock deformation and fluid flow at each updated timestep. The rock deformation is solved by the S3D DDM solution and the fluid flow equations are solved by the finite-difference method on a fixed grid of boundary elements. More details are referred to Wu (2014).

5.4. Model validation

The validation of the hydraulic fracture height growth module is provided in section 4.5 of Chapter 4. The model is validated against Liu and Valko's (2018) result with a six-layer asymmetric problem. The thickness and the true vertical depth are given by Liu and Valko (2018), the minimum horizontal in-situ stress distribution is depicted here in Figure 4.6a. Our results of the hydraulic fracture tip locations against the injection pressure are presented in Figure 4.6b together with Liu and Valko's results, illustrating that our results are in good agreement with their results. The results are validated against the commercial software MShale and FracPro as mentioned in their paper, and are also cross-validated by Mehrabi et al. (2021).

The verifications of the hydraulic fracture propagation model were provided against the analytical PKN and KGD solutions and the numerical Unconventional Fracture Model (UFM). A good match of fracture width, fracture half length, and fracture pressure was observed between our model and the published models (Wu 2014; Wu and Olson 2015).

5.5. Impact of weak bedding planes on single fracture propagation geometry

The proposed hydraulic fracturing propagation model considering the horizontal weak interfaces is applied in a laminated shale formation in Permian Basin to investigate the impact of the weak interfaces on the hydraulic fracture geometries. Permian Basin consists of three main basins, the Midland, Delaware, and Marfa basins. The Wolfcamp formation investigated in this study is located at the Midland Basin. Figure 5.1a depicts the geological stratigraphy of the Midland basin and the location of the Wolfcamp formations. The target interval is Wolfcamp B upper, which is most prolific formation. The total height along the vertical direction of the target zone is 67 m. The minimum horizontal in-situ stress along the depth in the target interval is presented in Figure 5.1b. The resolution is 1m/layer and the total number of layers is 67. The perforation depth is 2558m. The other geomechanics and fluid flow input parameters are summarized in Table 5.1.

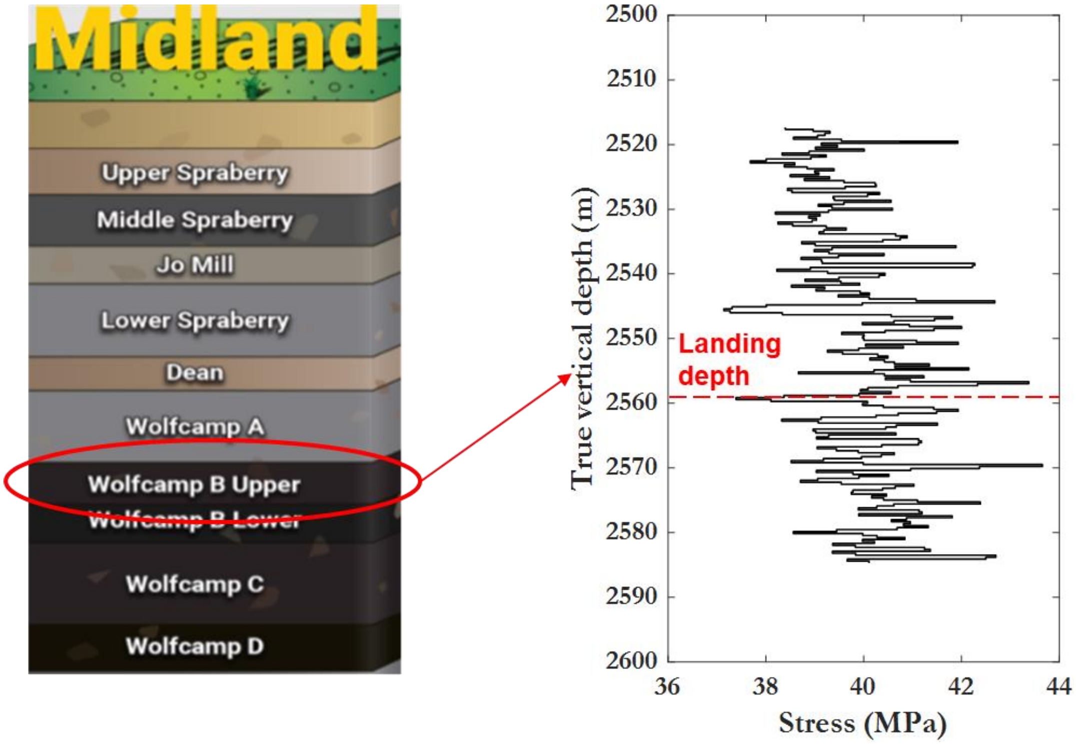

(a) (b)

Figure 5.1 (a) Schematic representation of the Midland Basin stratigraphy, (b) the minimum horizontal stress profile in the pay zone, the red-dash line indicating the well landing depth. (Reprinted from Li and Wu 2022a)

Table 5.1 Summary of input parameters for base case. (Reprinted from Li and Wu 2022a)

Young’s Modulus	40 GPa
Poisson’s Ratio	0.29
Injection rate	10 m^3/min
Injection time	90 min
Fluid viscosity	0.004 $Pa \cdot s$
Fluid density	1020 Kg/m^3
Fluid leakoff coefficient	0.0004 $m/sec^{0.5}$
Perforation diameter	0.0126 m
Mode I fracture toughness	2.198 $MPa \cdot \sqrt{m}$
Mode II fracture toughness	2.198 $MPa \cdot \sqrt{m}$
Interface fracture toughness	2.198 $MPa \cdot \sqrt{m}$
Spacing between interfaces	1 m
Overburden stress	47 MPa

In the base case, a single hydraulic fracture propagation in the Wolfcamp B formation is simulated using the proposed model. The spacing between the active horizontal weak interfaces is 1 m, indicating that totally 67 horizontal interfaces are evenly distributed in the target zone. After 90 mins injection, the final hydraulic fracture geometries and the width distributions without and with the impact of horizontal weak interfaces are presented in Figure 5.2 and Figure 5.3, respectively. The x-axis indicates the hydraulic fracture lateral length, the y-axis indicates the hydraulic fracture height, and the color of the fracture indicate the width values, which is marked by the color bar. As shown in Figure 5.2, without the impact of the weak interfaces the hydraulic fracture height reaches both the upper and lower limits of the target interval at the perforation location, resulting the maximum hydraulic fracture height 67 m. The fracture height along the lateral direction of the fracture trajectory is decreasing due to a decrease of pressure distribution. The average hydraulic fracture height is 41 m and the half length of the fracture is 96 m. A typical elliptical shape of the hydraulic fracture can be clearly observed, with maximum fracture width distributed in the center of the fracture and the minimum fracture width on the edges of the shape.

Considering the impact of the horizontal weak interfaces as shown in Figure 5.3, the hydraulic fracture shape is affected to be more likely the rectangular shape. It is observed that the hydraulic fracture does not reach the upper tip of the interval and the maximum hydraulic fracture height is reduced to 57 m. It is also indicated that the hydraulic fracture tends to grow downwards instead of upwards since longer fracture length reaches the bottom tip of the target zone. The average hydraulic fracture height is reduced from 41 m to 35 m, which is 14% reduction. The containment of the fracture in the vertical direction is because of the reduction of the stress intensity factors at the fracture tips caused by the shear slippage of the horizontal weak interfaces. In contrast, as a result of the containment in the vertical direction, the hydraulic fracture tends to propagate more likely in the lateral direction. The fracture half length has increased by 17%, from 96 m to 112 m. By comparing the width distribution from Figure 5.2 and Figure 5.3, it is found that overall hydraulic fracture width is decreased due to the existence of the weak interfaces, this observation matches the findings from Zhang and Jeffery (2006) and Kress and Weng (2019).

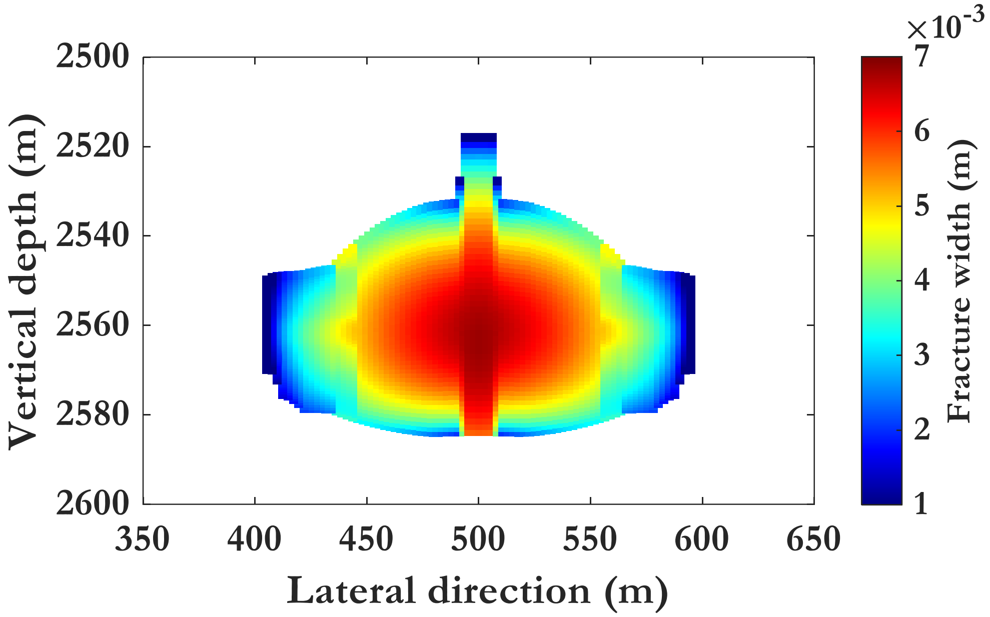

Figure 5.2 Hydraulic fracture geometry and width distribution after 90 mins injection without the impact of horizontal weak interfaces. (Reprinted from Li and Wu 2022a)

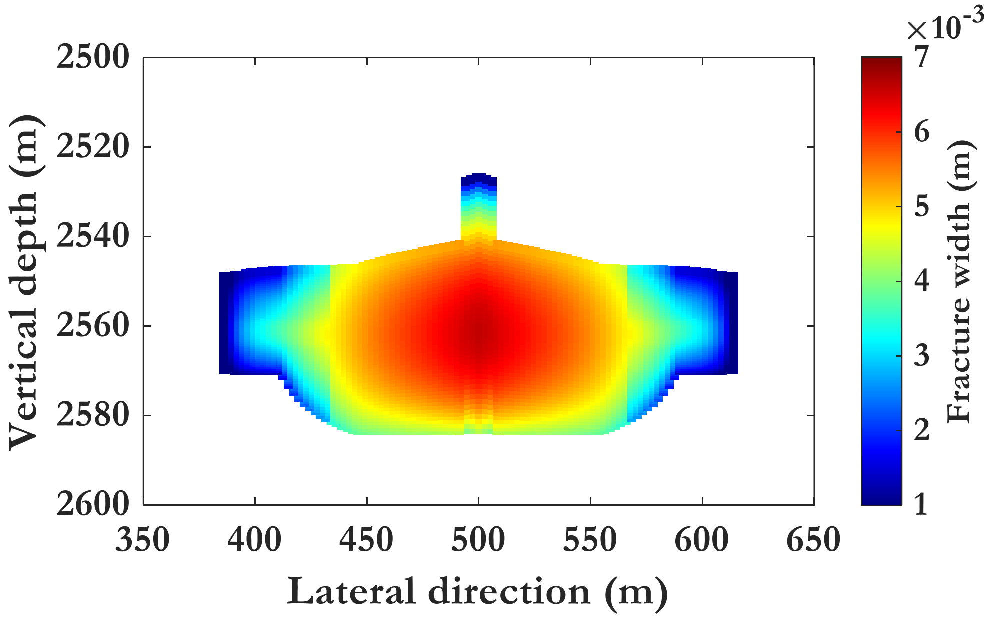

Figure 5.3 Hydraulic fracture geometry and width distribution after 90 mins injection with the impact of horizontal weak interfaces. (Reprinted from Li and Wu 2022a)

5.5.1. Sensitivity analysis: density of weak interfaces

In laminated shale formations, numerous horizontal interfaces can be observed within a single thin layer and the spacing between the interfaces can range from inches to a few meters. In this section we perform the sensitivity analysis on the density of the horizontal weak interfaces. Except from the base case where the spacing between the interfaces is 1 m, another two cases are simulated with the same other parameters but spacing set as 0.5 m and 1 m, respectively. The hydraulic fracture geometries and the width distributions of the base cases and the two additional cases are presented in Figure 5.4.

Several observations and implications can be obtained by comparing the group of fractures in Figure 5.4 and Figure 5.2 and 5.3. First of all, the maximum hydraulic fracture height (at the center of the fracture) and the overall average fracture height is decreasing as the decrease of the spacing between the horizontal interfaces. In Figure 5.2 and Figure 5.4b, fractures are still able to reach the bottom tip of the target zone, but fail to reach the upper tip due to the containment by the horizontal interfaces. Compared to the base case without considering the impact of weak interface in Figure 5.2, the overall average hydraulic fracture heights of cases Figure 5.4a, 5.3, and 5.4b, whose weak interface spacing is 2 m, 1 m, and 0.5 m, respectively, have decreased from 42 m to 38 m, 35 m, and 31 m, respectively. On the contrary, the hydraulic fracture half lengths of the three cases in Figure 5.4a, 5.3, and 5.4b have increased from 96 m to 105 m, 112 m, and 124 m, respectively, due to the decreasing spacing between the horizontal weak interfaces. The detailed changes of the maximum hydraulic fracture height, average fracture height, and the hydraulic fracture half length are recorded in Table 5.2. The general shape of the hydraulic fracture is transiting from an "elliptical shape" to the "rectangular shape". It is predictable that in highly-laminated formations where the spacing between the interfaces is as small as inches, the hydraulic fracture height might be terminated and contained within a limited zone. These findings demonstrated the significant impact of the horizontal weak interfaces on the hydraulic fracture geometry and show agreement with some field observations as well as numerical studies that hydraulic fracture height is more contained in specific layers in laminated layers (Gu et al. 2008; Fisher and Warpinski 2012; Weng et al. 2018).

Table 5.2 Impact of the bedding planes on the hydraulic fracture maximum height, average height, and the hydraulic fracture half length under different density. (Reprinted from Li and Wu 2022a)

Bedding plane density	Max height (m)	Average height (m)	Half length (m)
No bedding plane (base case)	67.06	41.91	96
0.5 bedding planes/meter	66.54	38.26 (-8.7%)	105.6 (+10.0%)
1 bedding plane /meter	57.64	35.15 (-16%)	112.8 (+17.5%)
2 bedding planes/meter	46.11	31.00 (-26%)	124.8 (+30%)

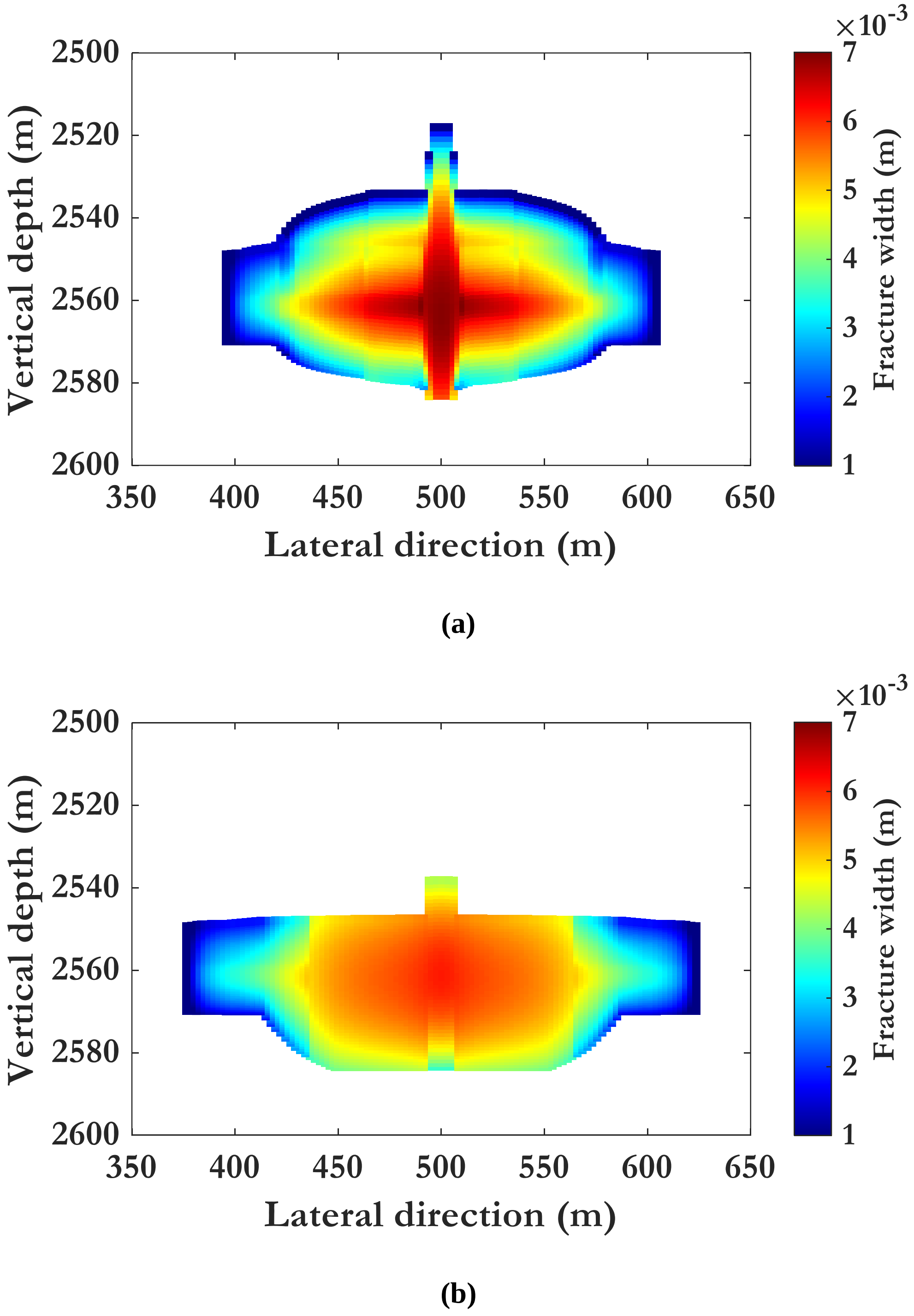

Figure 5.4 Hydraulic fracture shape and width distribution under the impact of different densities of weak interfaces: (a) weak interfaces spacing: 2 m (totally 33 interfaces in the whole interval), (b) weak interfaces spacing: 0.5 m (totally 132 interfaces in the whole interval). (Reprinted from Li and Wu 2022a)

5.5.2. Sensitivity analysis: fracture toughness of weak interfaces

The shear fracture toughness of the weak interfaces is another one of the important influencing factors that are difficult to accurately measure. In this section, a wide range of the shear fracture toughness of the horizontal interfaces is tested using our model to investigate its sensitivity on the hydraulic fracture propagation. Three cases with interfacial spacing at 1 m and with the shear fracture toughness 1.099, 2.198, and 4.395 $MPa \cdot \sqrt{m}$, respectively are simulated to compare the case without considering the horizontal interfaces.

Figure 5.5 demonstrates the comparison of the fracture shape and the fracture width under the impact of different weak interfaces' shear fracture toughness. Compared to the base case Figure 5.2 without the impact of the horizontal weak interface, Figure 5.5a, 5.3, and 5.5b, which represent the fracture geometries with the shear fracture toughness 1.099, 2.198, and 4.395 $MPa \cdot \sqrt{m}$, respective, all show the similar changes in the fracture geometries, i.e., a decrease in the overall average height, an increase in the hydraulic fracture half length, and a more rectangular hydraulic fracture shape. Specifically, the average hydraulic fracture height of Figure 5.5a, 5.3, and 5.5b has reduced from 41 m to 37 m, 35 m, and 33 m, respectively, and the hydraulic fracture half length of the three cases has increased from 96 m to 110 m, 112 m, and 117 m, respectively. The detailed changes of the maximum hydraulic fracture height, average fracture height, and hydraulic fracture half length are recorded in Table 5.3. It is concluded that larger shear fracture toughness results in a more contained hydraulic fracture height but a larger hydraulic fracture half length. The reason is that under equilibrium status, larger shear fracture toughness results in a larger shear slippage length in the horizontal interface, hence adding more impact on the reduction of the effective stress intensity factor of the vertical hydraulic fracture. Compared to the changes of the fracture geometries due to the increasing of the interface density, we find that the changes due to the increasing of the interface fracture toughness is less intensive.

Table 5.3 Impact of the bedding planes on the hydraulic fracture maximum height, average height, and the hydraulic fracture half length under different shear toughness. (Reprinted from Li and Wu 2022a)

Bedding plane toughness	Max height (m)	Average height (m)	Half length (m)
No bedding plane (base case)	67.06	41.91	96
KIIc = 0.5 KIc	64.37	37.34 (-10.9%)	110.4 (+14.6%)
KIIc = KIc	57.64	35.15 (-16%)	112.8 (+17.5%)
KIIc = 2 KIc	50.69	33.24 (-20%)	117.6 (+22.5%)

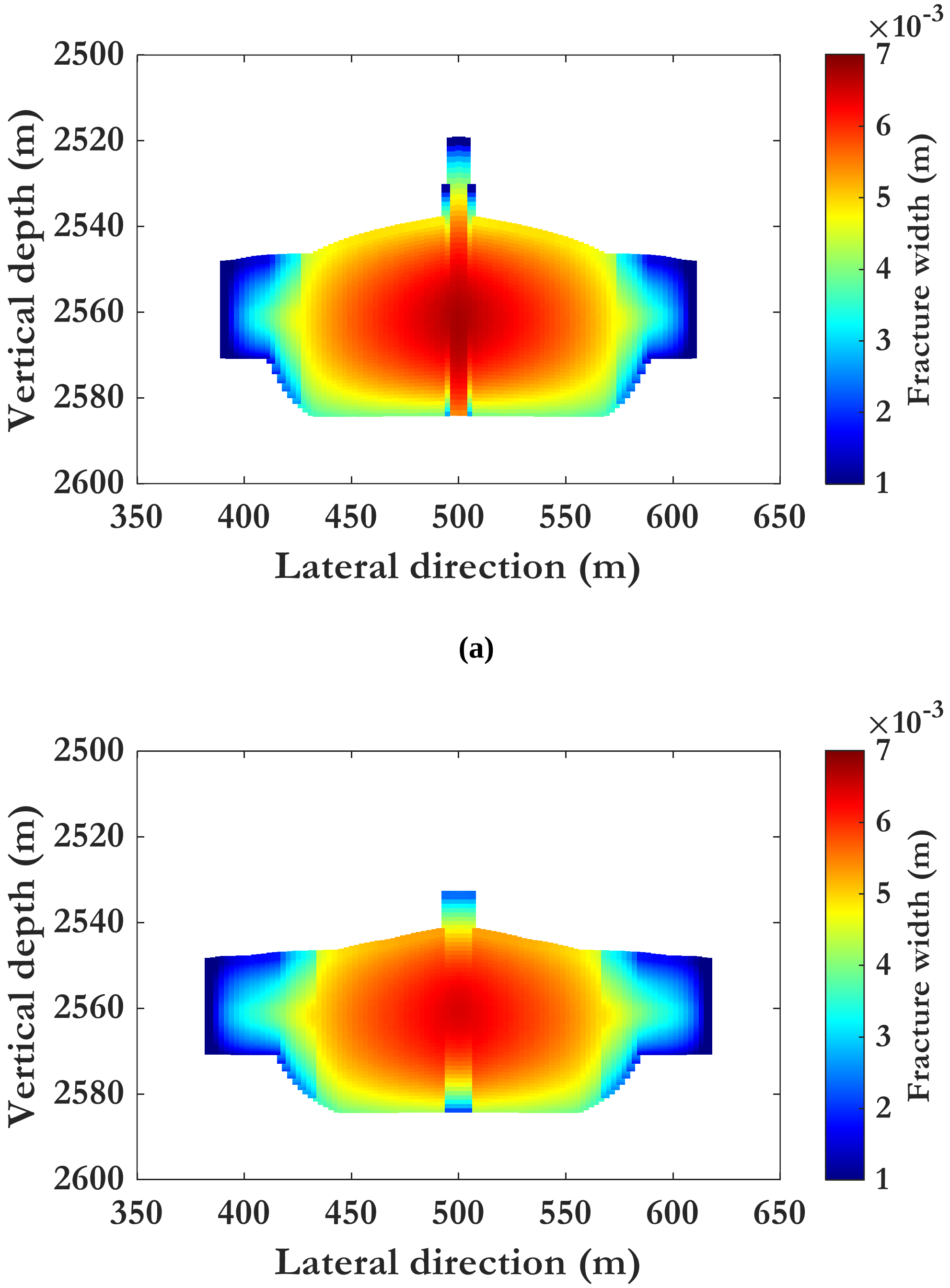

(a)

(b)

Figure 5.5 Hydraulic fracture shape and width distribution under the impact of different fracture toughness of weak interfaces: (a) interfaces with spacing 1 m and with K_{IIc} = 1.099 $MPa \cdot \sqrt{m}$, (b) interfaces with spacing 1 m and with K_{IIc} = 4.395 $MPa \cdot \sqrt{m}$.(Reprinted from Li and Wu 2022a)

5.6. Impact of weak bedding planes on multi-fracture propagation geometry

In this section, five clusters simultaneous propagation is simulated using our proposed model. The geomechanics and fluid flow parameters are the same as the single fracture scenario which is summarized in Table 5.4. The cluster spacing is 10 meters. After 90 mins injection, the final hydraulic fracture geometries and the width distributions without and with the impact of horizontal weak interfaces are presented in Figure 5.6 and Figure 5.7, respectively.

Table 5.4 Summary of input parameters for multi-fracture case. (Reprinted from Li and Wu 2022a)

Injection rate	15 m^3/min
Injection time	90 min
Fluid viscosity	0.004 $Pa \cdot s$
Fluid density	1020 Kg/m^3
Fluid leakoff coefficient	0.0003 $m/sec^{0.5}$
Perforation diameter	0.0096 m
Mode I fracture toughness	2.198 $MPa \cdot \sqrt{m}$
Mode II fracture toughness	2.198 $MPa \cdot \sqrt{m}$
Interface fracture toughness	2.198 $MPa \cdot \sqrt{m}$
Spacing between interfaces	1 m
Overburden stress	47 MPa
Cluster spacing	10 m

Figure 5.6 represents the fracture geometry and the width distribution without considering the interfaces. As shown in the figure, outer fractures (fracture 1 and fracture 5) have the largest half length, while middle fractures (fracture 2 and fracture 4) and innermost fracture (fracture 3) are contained because of the stress shadow effect. Moreover, the width values in the inner and middle fractures are much smaller compared to the outer fractures. This can restrict the region for proppant transport where the fracture width is too small to allow proppant particles to pass through, resulting in some unpropped portions of a fracture. The width values in the outer fractures are larger because they turn their propagation direction outward and experience less stress shadow effects. Figure 5.7 shows the fracture geometry and the width distribution with the impact of the interfaces. Similar phenomena are observed that outer fractures have much larger half length and width values. However, the geometry and the width distribution of each individual fracture have changed due to the impact of the weak interfaces. Generally, all fractures experience an increase of the half length and a decrease of the maximum height. All fractures fail to reach the upper limit of the target zone. In terms of the average fracture height and the width values, outer fractures and inner (middle and innermost) fractures display different patterns.

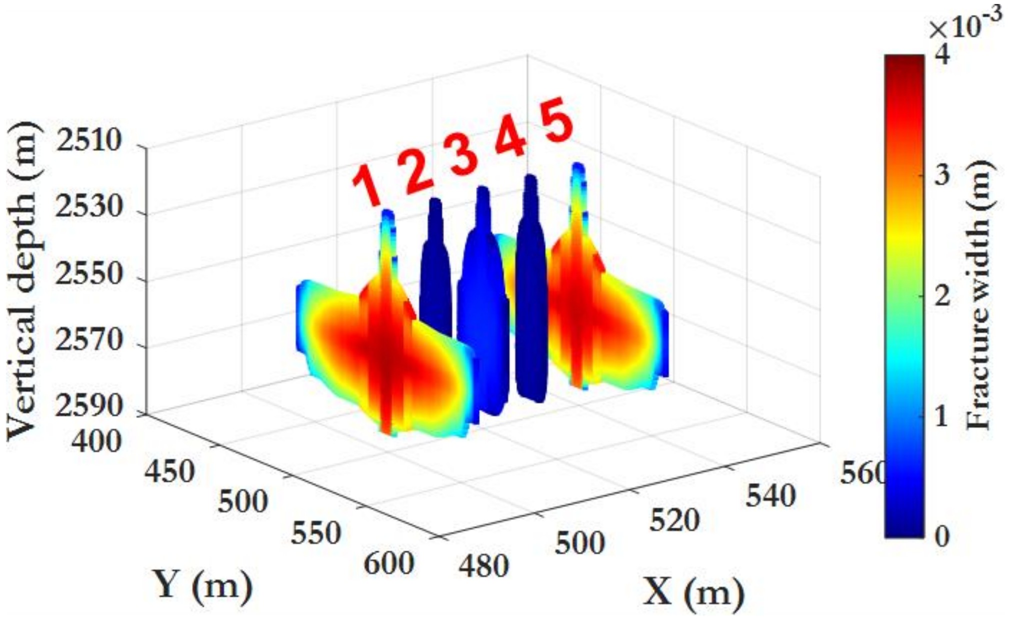

Figure 5.6 Hydraulic fracture shape and width distribution without the impact of horizontal interface. (Reprinted from Li and Wu 2022a)

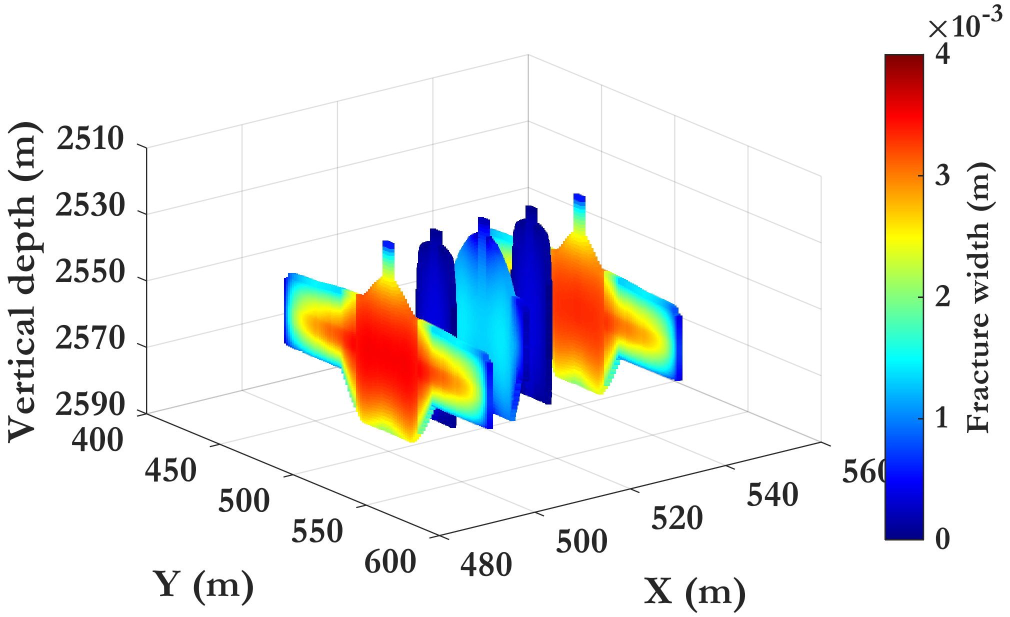

Figure 5.7 Hydraulic fracture shape and width distribution with the impact of horizontal interfaces with 1 m spacing. (Reprinted from Li and Wu 2022a)

To clearly illustrate the impact of the weak interfaces on the fracture height and the width distribution of the fractures, we show the final fracture geometry and the width distribution of each fracture separately in Figure 5.8, 5.9, and 5.10. Figure 5.8 illustrates the comparison of outer fractures (fracture 1 and 5) shape and the width distribution between the cases without and with the impact of weak interfaces. It is observed that the existence of the weak interfaces results in a reduction of the average height from 33 m to 29 m, by 12%. Meanwhile, a decrease of overall width values is observed. However, completely different rhythms are observed in Figure 5.9, the comparison of the middle fractures (fracture 2 and 4). Figure 5.9 indicates that both the average hydraulic fracture height and the width values are increased. The average height has increased from 37 m to 41 m, and the maximum width at the fracture center has increased more than ten times. This is because of the reduced outer fracture height resulting in less stress shadow effects on the middle ones. The comparison for the innermost fracture (fracture 3) geometries is shown in Figure 5.10, where the average hydraulic fracture height is almost unchanged (a slight increase from 38.5 m to 39 m), but the overall fracture width values are considerably increased.

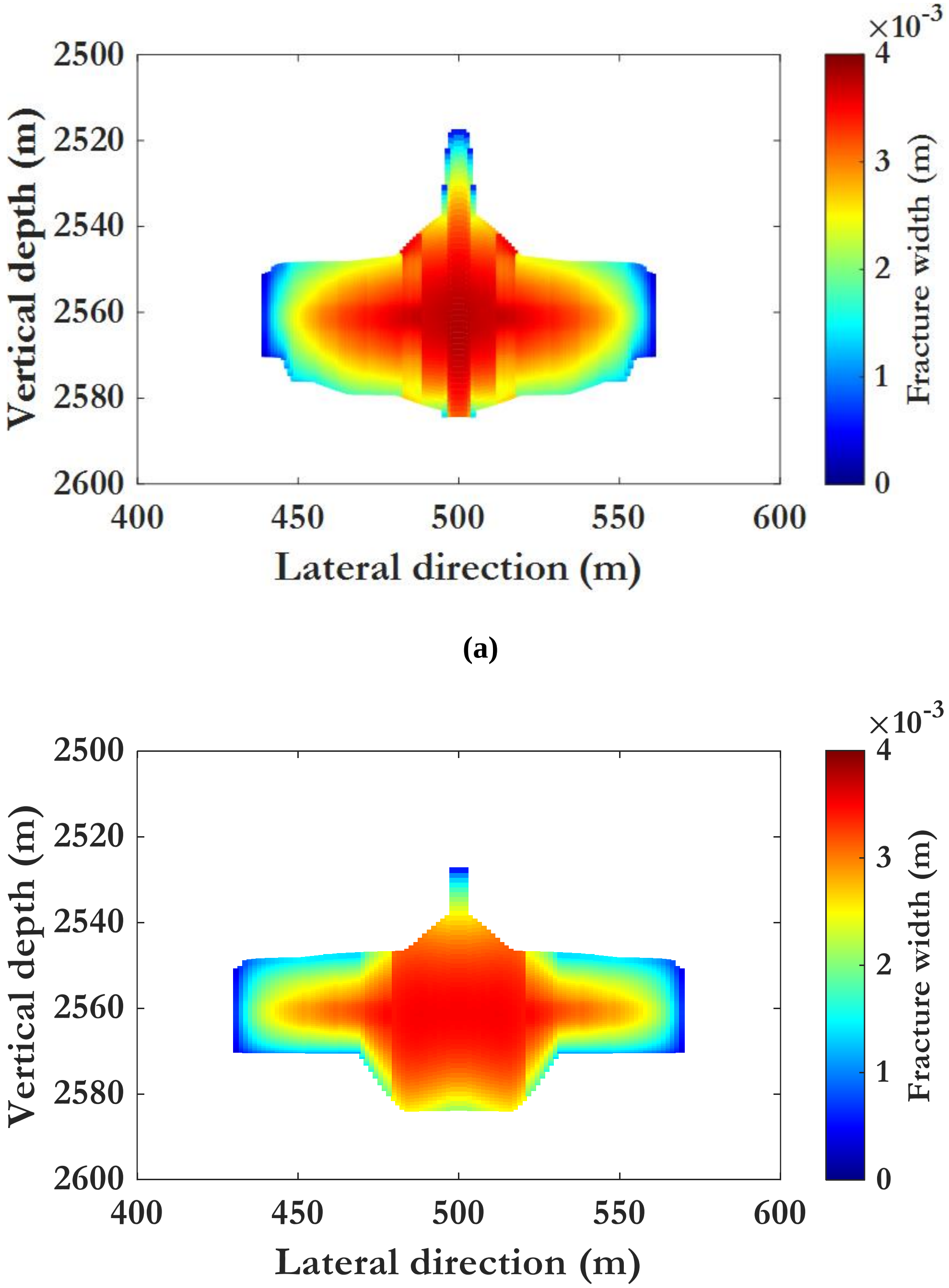

(a)

(b)

Figure 5.8 Outer fractures (fracture 1 or 5) shape and width distribution under (a) no weak interfaces, (b) the impact of weak interfaces with 1 m spacing. (Reprinted from Li and Wu 2022a)

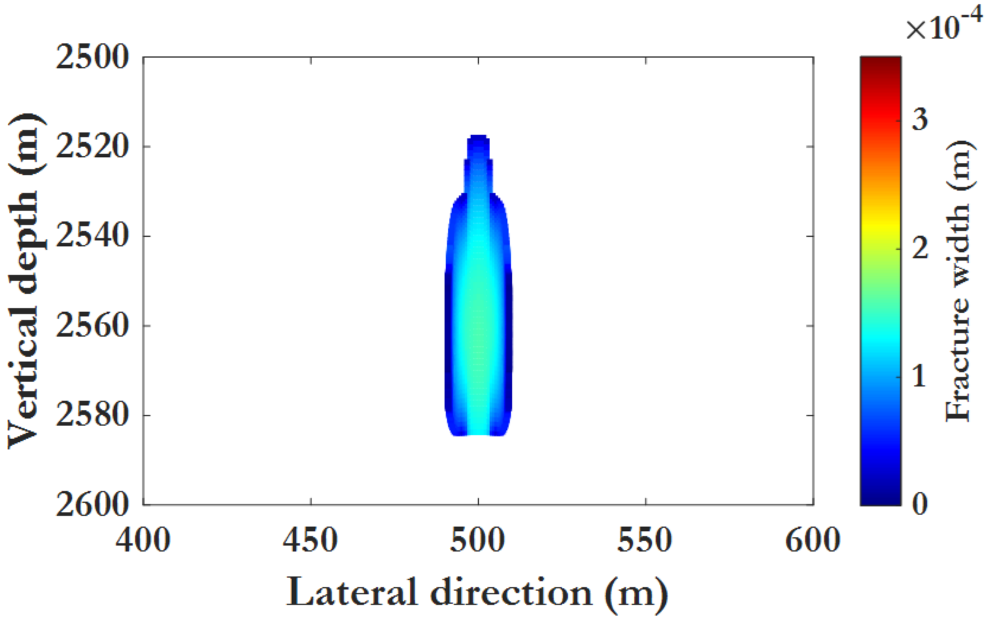

(a)

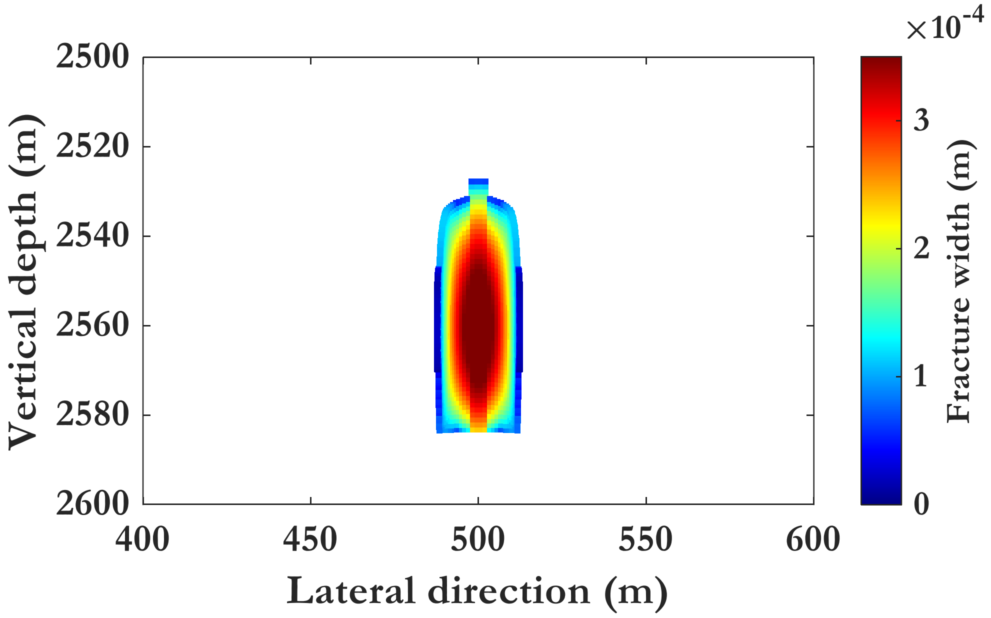

(b)

Figure 5.9 Middle fractures (fracture 2 or 4) shape and width distribution under (a) no weak interfaces, (b) the impact of weak interfaces with 1 m spacing. (Reprinted from Li and Wu 2022a)

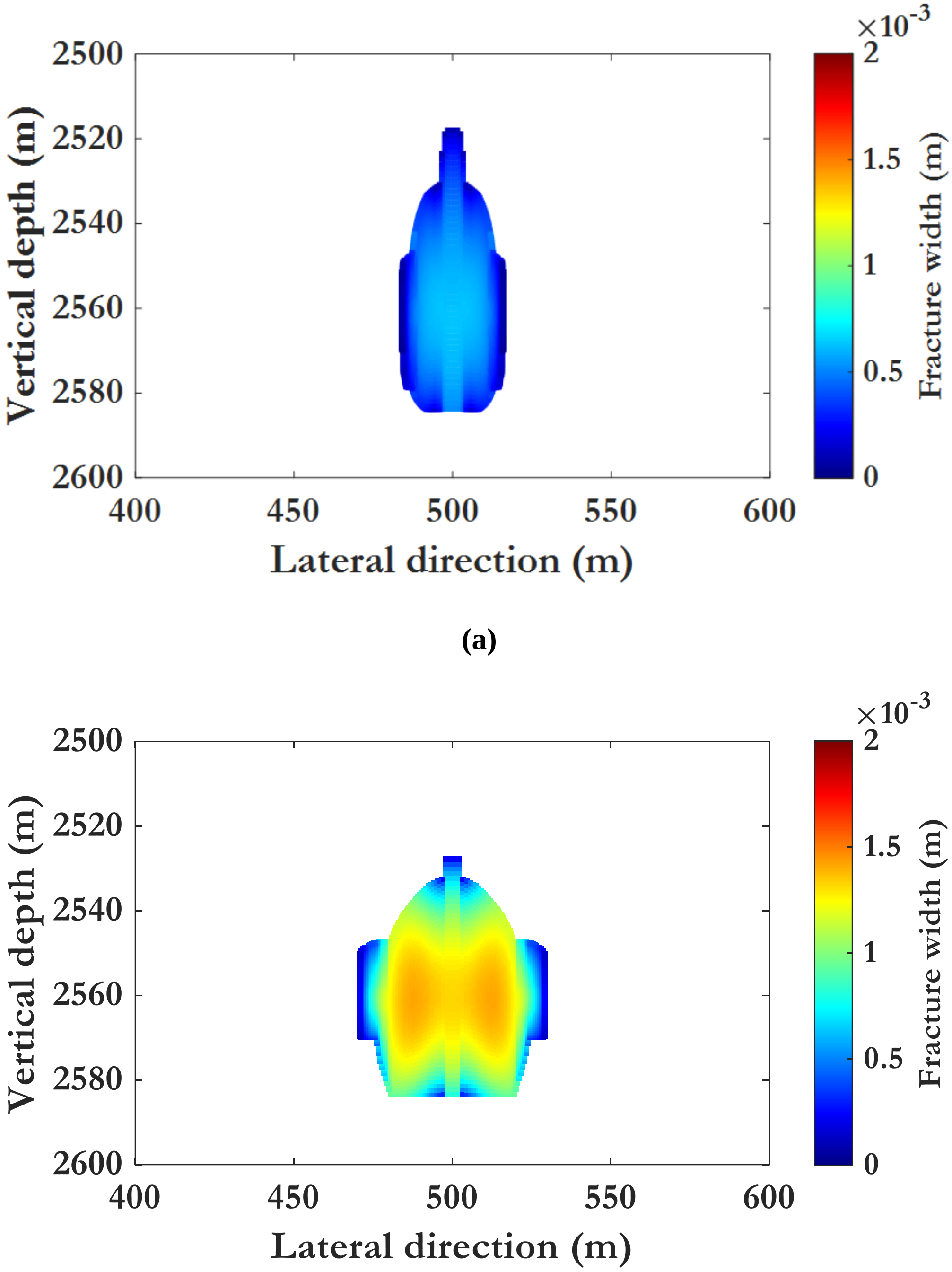

(a)

(b)

Figure 5.10 Innermost fracture (fracture 3) shape and width distribution under (a) no weak interfaces, (b) the impact of weak interfaces with 1 m spacing. (Reprinted from Li and Wu 2022a)

The impact of the horizontal weak interfaces on the multi-fracture simultaneous propagation can be summarized as follows: the height of the outer fractures (fracture 1 and 5) is reduced because of the change of the stress intensity factors caused by the shear slippage of the weak interfaces, consequently, the outer fractures tend to propagate laterally which results in a larger half length. Meanwhile, the inner fractures (fracture 2, 3, and 4) benefit from the reduced height of the outer fractures which weakens the stress shadow effects. Although the fracture maximum heights for inner fractures are decreased at the center and cannot reach the upper limit of the target zone, the overall average heights are increased. Moreover, all inner fractures experience the increase of not only the fracture half length, but the overall width values.

A detailed comparison of the hydraulic fracture half length growth versus the injection time between no-interface case and with-interface case for each individual fracture is demonstrated in Figure 5.11. The outer fractures 1 and 5 are symmetrical to each other and so as the middle fractures 2 and 4. Therefore only fracture 1, 2, and 3 are presented. All fractures experience an increase of the fracture half length due to the impact of the weak interfaces. However, the increase rate varies from outer fracture to the innermost fracture, this is because the competition between the reduced “stress shadowing effect” caused by the outer fractures, and the “effect of the horizontal bedding planes”. The outer fracture half length has increased by 12%, from 61 m to 69 m. The middle fracture half length increases by 20%, from 10 m to 12 m. The innermost fracture half length increases by 80%, from 16 m to 29 m. The innermost fracture is the most benefited segment due to the existence of the weak interfaces.

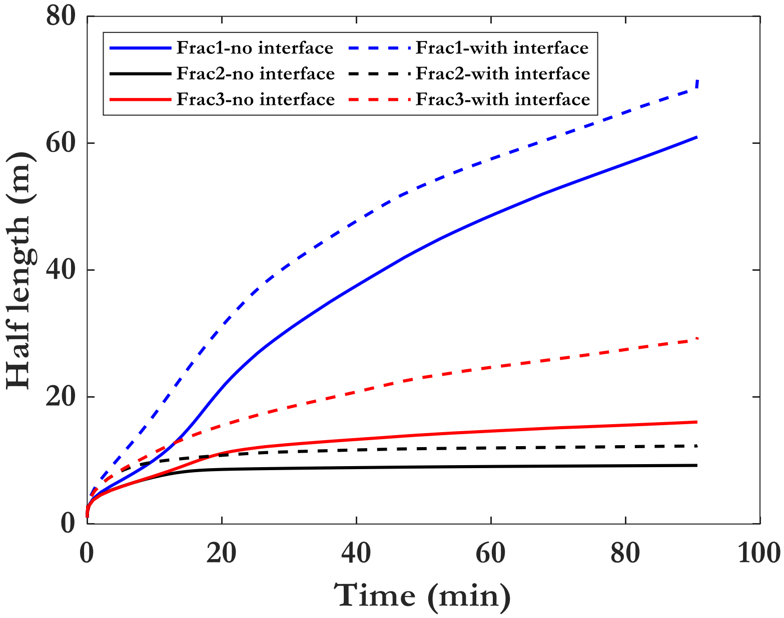

Figure 5.11 Hydraulic fracture half length growth versus injection time for outer fracture (fracture 1, blue), middle fracture (fracture 2, black), and innermost fracture (fracture 3, red) with (dash lines) and without (solid lines) the impact of weak interfaces. (Reprinted from Li and Wu 2022a)

5.6.1. Sensitivity analysis: density of weak interfaces

In this section we perform the sensitivity analysis on the density of the horizontal weak interfaces for multiple-fracture case. Similar to the single fracture case, except from the base case where the spacing between the interfaces is 1 m, another two cases are simulated with the same other parameters but spacing set as 0.5 m and 1 m, respectively. The hydraulic fracture geometries and the width distributions of the base cases and the two additional cases are presented in Figure 5.12.

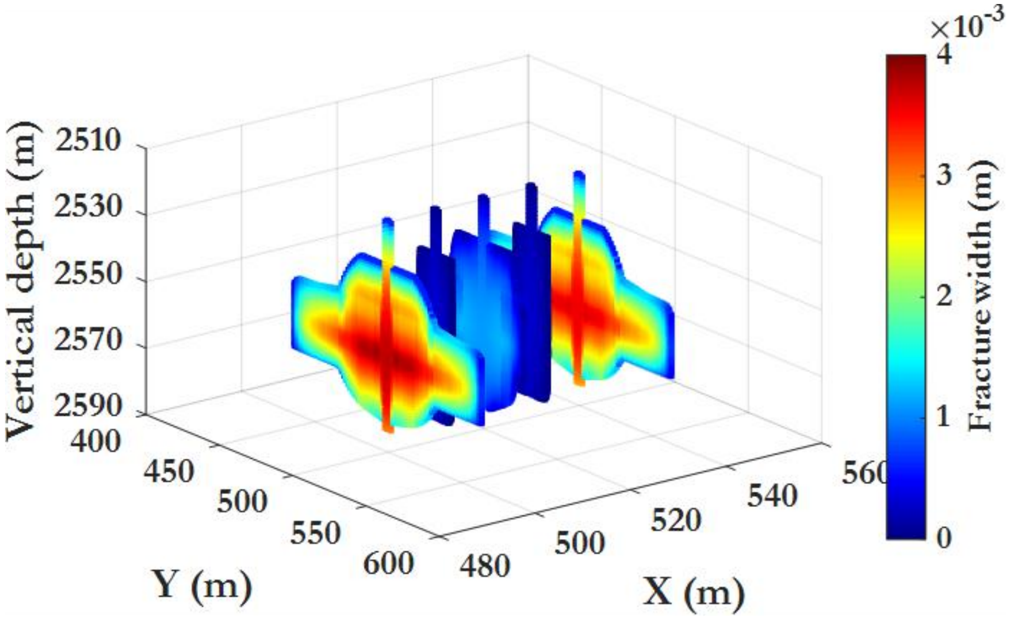

(a)

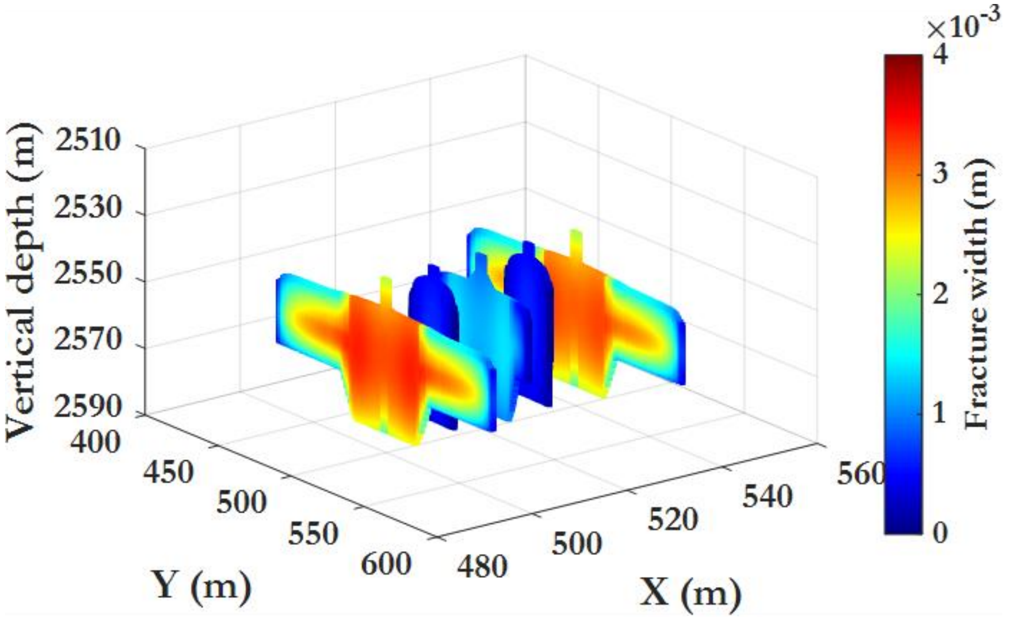

(b)

Figure 5.12 Multi-fracture case hydraulic fracture shape and width distribution under the impact of different densities of weak interfaces: (a) weak interfaces

spacing: 2 m (totally 33 interfaces in the whole interval), (b) weak interfaces spacing: 0.5 m (totally 132 interfaces in the whole interval). (Reprinted from Li and Wu 2022a)

By comparing Figure 5.12a and 5.12b with Figure 5.4a and 5.4b, similar observations of the trends and conclusions can be obtained as that obtained from the single fracture case. The general shape of the hydraulic fracture is transiting from an “elliptical shape” to the “rectangular shape”. Denser horizontal bedding interfaces act more impact on the reduction of the hydraulic fracture height and consequent increase of the hydraulic fracture half length.

5.6.2. Sensitivity analysis: cluster spacing

A similar five-fracture simultaneous propagation scheme with 15 m cluster spacing is simulated in this section to investigate the impact of the horizontal weak interfaces at different fracture spacing. The hydraulic fracture shape and the width distribution of the cases without and with the impact of weak interfaces are presented in Figure 5.13 and Figure 5.14, respectively. It is illustrated in Figure 5.13 that a considerable decrease of the overall width values is observed in outer fractures (fracture 1 and 5) while a significant increase is observed in the middle fractures (fracture 2 and 4). Meanwhile, the half length of all the fractures have increased, which is the same trend as observed in the 10 m spacing cases. However, the average hydraulic fracture heights for all fractures suffer from a reduction due to the existence of the horizontal weak interfaces, which demonstrates different rhythms from the 10 m spacing cases.

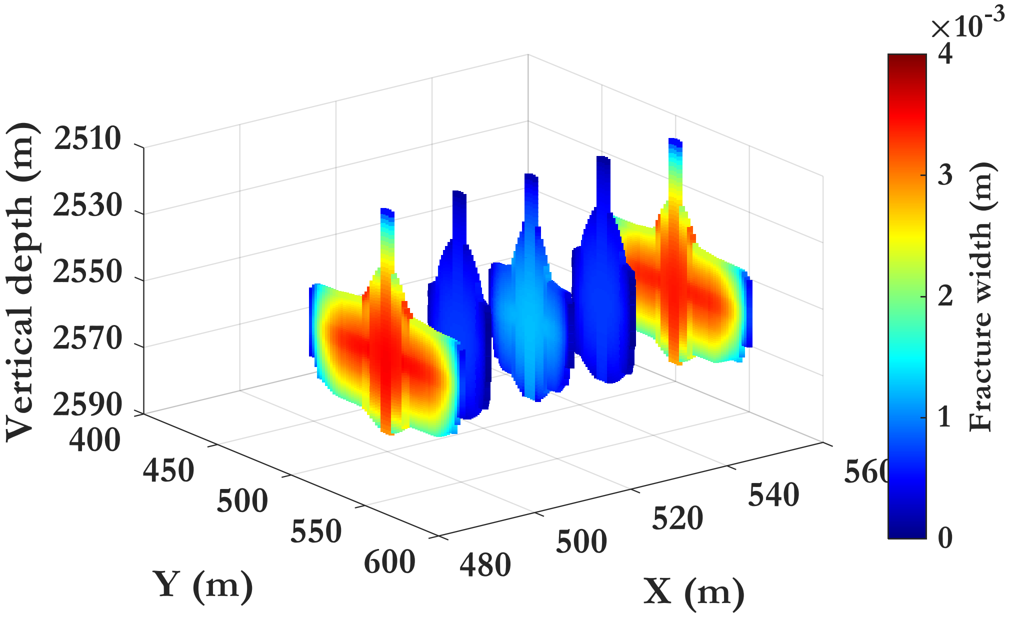

Figure 5.13 Hydraulic fracture shape and width distribution without the impact of horizontal interface. (fracture spacing = 15 m) (Reprinted from Li and Wu 2022a)

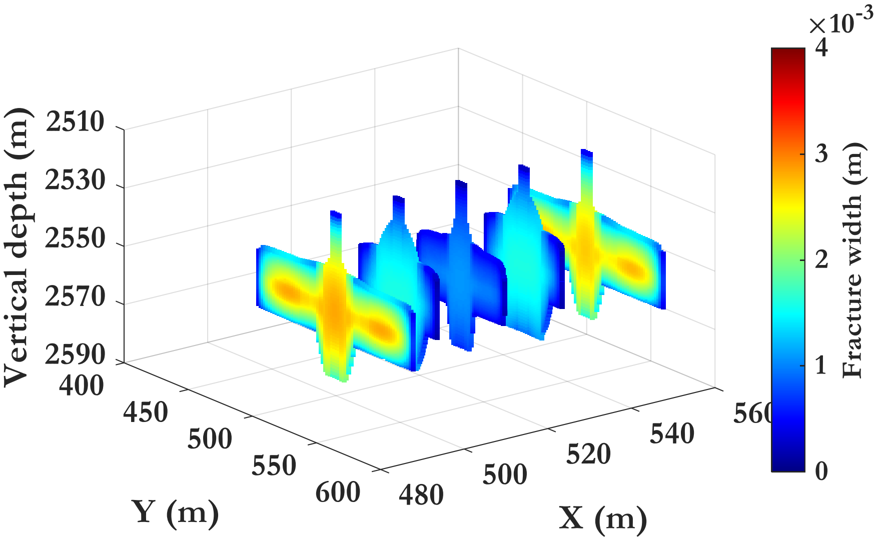

Figure 5.14 Hydraulic fracture shape and width distribution with the impact of horizontal interface. (fracture spacing = 15 m) (Reprinted from Li and Wu 2022a)

The comparison of the final geometries and the width distributions of the inner fractures (middle fractures 2 and 4, and innermost fracture 3) without and with the weak interfaces are presented in Figure 5.14 and Figure 5.15. It is indicated in Figure 5.14 that the average hydraulic fracture height under the impact of the weak interfaces is reduced by 11%, from 35 m to 31 m, which is opposite from the trend demonstrated in the 10 m spacing case. Figure 5.15 shows that the average fracture height of the innermost fracture under the impact of the weak interfaces is reduced by 24%, from 33 m to 25 m, which is also different what is observed in the 10 m spacing case.

Another difference from the 10 m spacing case is observed that the fracture width values in Figure 5.15 are decreased due to the impact of the weak interfaces. These two sets of numbers from different-spacing cases indicate that although the inner fractures benefit from the reduction of the outer fracture’s average height, the change of the geometries under different fracture spacings are quite different. With the existence of the weak interfaces, the half lengths of the inner fractures have increased, while the average height and the width values of the inner fractures vary from the innermost one to the middle ones. From Figure 5.13, we can observe that the differences between each fracture are smaller than the differences between the fractures shown in Figure 5.12. A detailed comparison is presented in Figure 5.17. This is an indication that the impact of the horizontal weak interfaces tends to make the fractures more contained in the height direction and more uniform in the lateral length, which is a good agreement with previous findings (Cooke and Underwood 2001; Rutledge et al. 2016; Diaz et al. 2018).

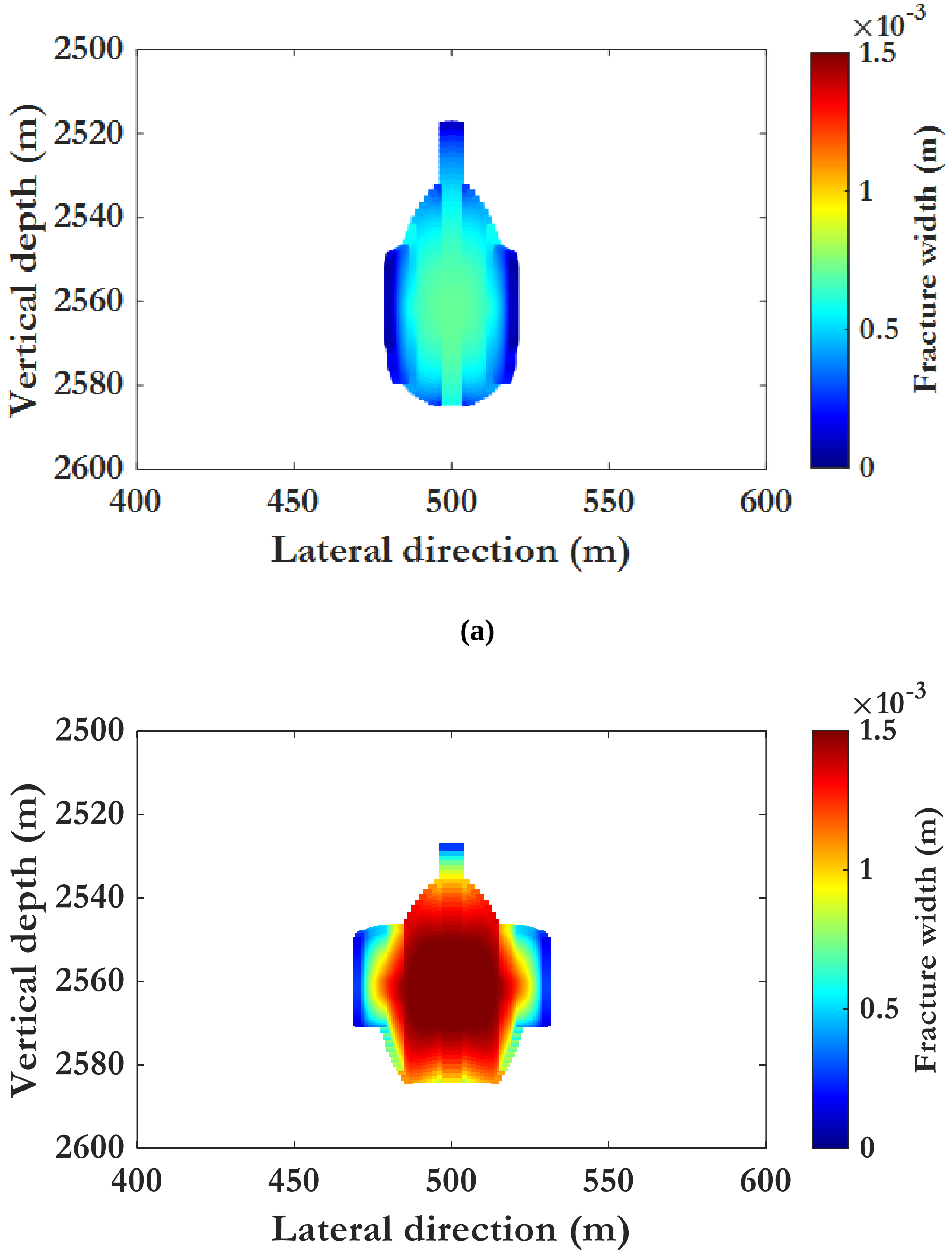

(a)

(b)

Figure 5.15 Middle fractures (fracture 2 or 4) shape and width distribution under (a) no weak interfaces, (b) the impact of weak interfaces with 1 m spacing. (fracture spacing = 15m) (Reprinted from Li and Wu 2022a)

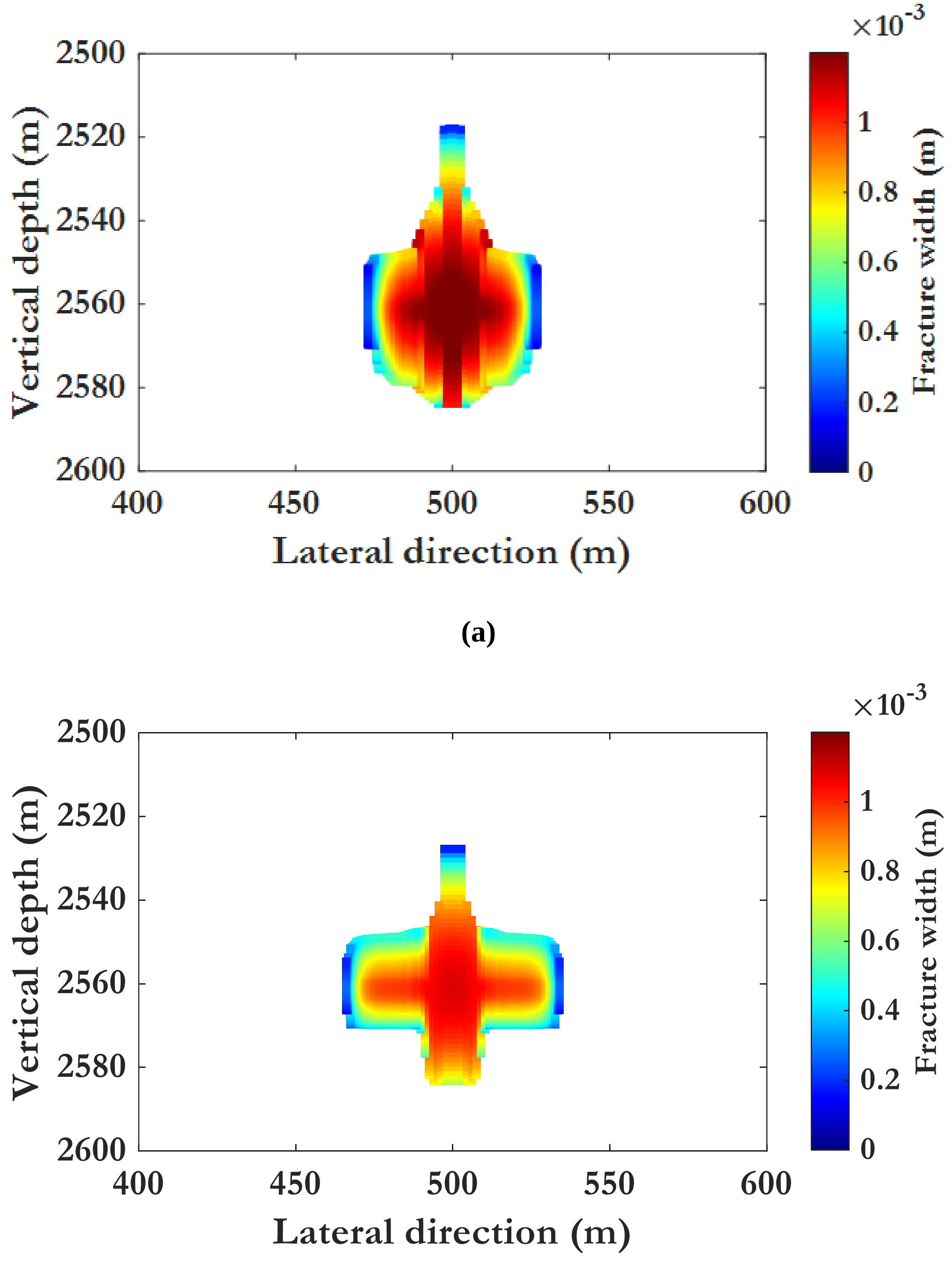

(a)

(b)

Figure 5.16 Innermost fracture (fracture 3) shape and width distribution under (a) no weak interfaces, (b) the impact of weak interfaces with 1 m spacing. (fracture spacing = 15m)

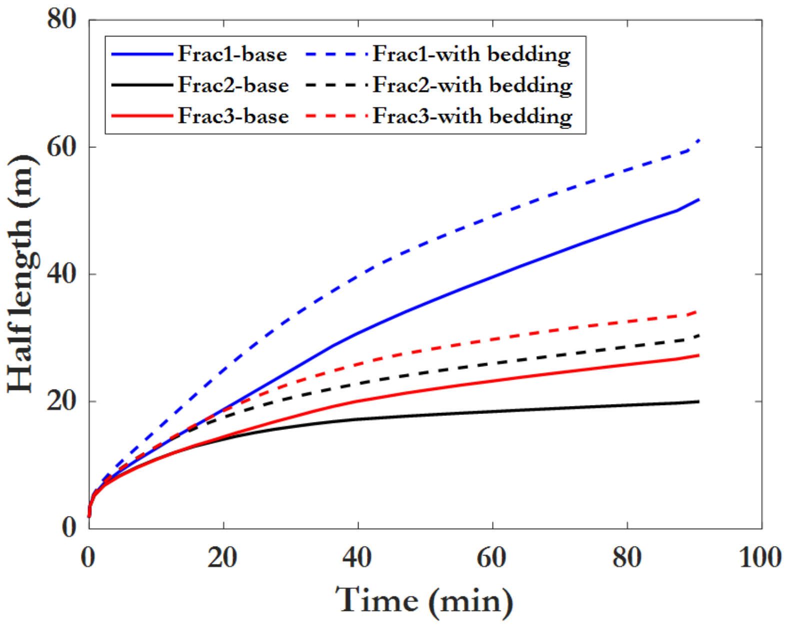

Figure 5.17 Hydraulic fracture half length growth versus injection time for outer fracture (fracture 1, blue), middle fracture (fracture 2, black), and innermost fracture (fracture 3, red) with (dash lines) and without (solid lines) the impact of weak interfaces. (Reprinted from Li and Wu 2022a)

Figure 5.16 presents the comparison of the hydraulic fracture half length growth versus the injection time between closer spacing (10 m) case and larger spacing (15 m) case for each individual fracture. By comparing the same fractures with different cluster spacings, we found that the half length of the outer fractures is decreased, while the half lengths of the inner fractures are increased when increasing the cluster spacing. Since the five fractures are propagating simultaneously and competing with each other, the inner fractures are hindered due to the stress shadow effects by the outer fracturs in closer-spacing case. An increase of the cluster spacing reduces the impact of the stress shadow, which results an increase of the inner fracture half length. When the fracture spacing is further increased, the stress shadow will be less influential, and the inner fractures will be more likely identical to the outer fractures. In such case, the rhythm of each individual fracture under the impact of the weak interfaces follows the same as previously discussed in the single fracture scenario.

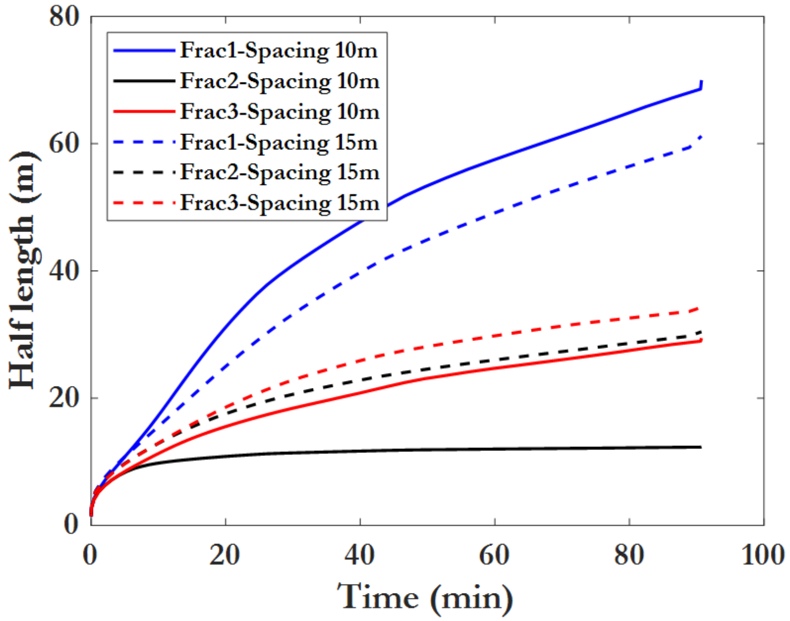

Figure 5.18 Hydraulic fracture half length growth versus injection time for outer fracture (fracture 1, blue), middle fracture (fracture 2, black), and innermost fracture (fracture 3, red) with (dash lines) and without (solid lines) the impact of weak interfaces. (fracture spacing = 15m) (Reprinted from Li and Wu 2022a)

5.7. Conclusions

To summarize, this work presents an efficient and comprehensive hydraulic fracture height growth model, which is incorporated in a pseudo-3D (P3D) hydraulic fracture simulator to investigate the impact of the weak interfaces on both the fracture height and the lateral propagation. The comprehensive hydraulic fracture height growth model considers not only the conventional impact factors that governs the fracture height, but also the influence of the horizontal weak interfaces. The interaction between the weak interfaces and the hydraulic fracture is modeled by an efficient 2D higher order displacement discontinuity method and the effectiveness on the hydraulic fracture height is quantified by correcting the stress intensity factors at the hydraulic fracture tips. This model is non-intrusive and is incorporated into an in-house cell-based P3D hydraulic fracture simulator, which uses plane strain deformation in each vertical cross-section coupled with a 2D fluid flow. Numerical examples are performed based on a Permian Basin field case to study the impact of the weak interfaces on the fracture propagation. Results show that the weak interfaces have considerable impact on the fracture height and overall fracture contact area. With the existence of the weak interfaces, the hydraulic fracture height is shortened vertically. Moreover, the hydraulic fracture height considering the effect of weak interfaces is decreasing slower along the lateral direction, generating a longer fracture lateral length. Sensitivity analysis shows that denser interfaces and larger interfacial shear toughness require more energy and higher net pressure to break through the vertical resistance, and result in shorter hydraulic fracture height but longer hydraulic fracture lateral length.

6. CONCLUSIONS

This chapter first summarizes the main contributions and conclusions that are obtained from this research dissertation. After that, some recommendations for the extending work are proposed for future research.

6.1. Outcomes of the research work

6.1.1. Joint-Element Higher Order Displacement Discontinuity Method

The joint element higher order displacement discontinuity method (JE-HDDM) is developed in this research. The JE-HDDM demonstrates high stability and accuracy, as well as efficiency in close-spacing fracture problems, while traditional CDDM fails to give physically reliable results in an efficient way. The major contribution of this new method compared to the conventional DDM is that it avoids the negative width in closely-spaced planar hydraulic fractures. Additionally, by using the quadratic interpolation on the three-element patch, the new method significantly improves the computational efficiency, which means that it requires a much smaller number of elements to achieve the same level of accuracy given by the conventional DDM.

General conclusions obtained from case studies are summarized as follows:

- In close-spacing fracture problems, CDDM loses accuracy and even stability when predicting the fracture behavior and stress responses due to the strong stress shadowing effect. To maintain the stability of close-spacing fracture problems, extremely fine grids must be used in the simulation to accurately capture the stress shadowing effect acting on the inner fractures. However, even with fine grids, the accuracy of CDDM is dropping fast when the fracture spacing becomes smaller. On the contrary, the developed JE-HDDM can always provide highly accurate and physically reliable results for close-spacing problems, even using coarse elements, by means of quadratic approximation of the displacement discontinuities on the computational elements. The efficiency of JE-HDDM is maintained through a patched-element pattern which allows quadratic interpolation without increasing computational points.

- Negative opening widths of inner fractures in close-spacing fracture cases are observed using CDDM, which are physically impossible. JE-HDDM successfully deals with this problem by introducing joint elements where different contact types of the elements are solved simultaneously. The mechanically closed and open parts of the fractures due to the combined influence of boundary conditions and stress shadowing effect are accurately modeled through stick and separation modes of the joint elements.
- JE-HDDM demonstrates high accuracy not only when predicting the displacement discontinuities, but also in the induced stress profiles in near fracture areas. Due to the assumption of constant distribution of displacement discontinuities, CDDM fails to accurately capture the stresses and displacements for field points closer than approximately one element length from the fracture. The quadratic interpolation as well as the square-root treatment on the tip elements allow HDDM to give accurate results in near fracture locations.

- Stress intensity factors calculated from the displacement discontinuities given by JE-HDDM is way more accurate than that of JE-CDDM. To obtain reliable results (relative error less than 10%), JE-CDDM must use extremely fine grids (ten times smaller than JE-HDDM), which dramatically increases computational time. The outperformance in accuracy of JE-HDDM over JE-CDDM is more obvious regarding the stress intensity factor of mode II. For shear slippage or shear dilation problems in weak interfaces, JE-HDDM is highly recommended to avoid intensive fine grids used in JE-CDDM

6.1.2. Hydraulically Induced Shear Slippage of Weak Bedding Interfaces

Two numerical models are developed to study the hydraulic fracture induced shear slippage and dilation of the weak bedding interfaces in the shale laminations.

The dynamic model couples the fluid flow and rock deformation during the shear slippage process and provides a better understanding the shear dilation mechanism. Several findings from the synthetic case studies are obtained:

- Although horizontal bedding planes may not mechanically open during hydraulic fracturing due to the large vertical stress boundary conditions, the bedding plane shear slippage affects the hydraulic fracturing by fluid leaking off and conductivity growth.
- Different from hydraulic fracturing, in the bedding plane shear sliding, shear slippage is initially behind the fluid front but will take over the fluid front afterwards. This is because that under in-situ stress conditions, the shear slippage

won’t happen naturally without any disturbance. However, the hydraulic fracturing induces the fluid leaking from the vertical fracture into the horizontal beddings, resulting in the elevation of the pore pressure, and the subsequent shear slippage.

- Fluid viscosity and the initial bedding layer width have great impact on the shear dilation process. Large fluid viscosity and/or small initial bedding interface hydraulic aperture put more resistance on the fluid leaking off and flow within the horizontal bedding plane.

The static model is based on the linear elastic fracture mechanics and applies the idea from the “FracT” model. The static model is much more efficient than the dynamic model, which provides a possible approach for incorporating the bedding plane mechanism into the fracture height model. The incorporation of the static model into the fracture model is introduced and applied in Chapter 3 and 4.

6.1.3. Hydraulic Fracture Height Growth Considering Effect of Weak Bedding Planes

A comprehensive and non-intrusive hydraulic fracture height growth model has developed considering the effect of the weak bedding layers. The interaction between the hydraulic fracture and the bedding layers and its impact on the hydraulic fracture height growth are modelled by an efficient higher order displacement discontinuity method. The effectiveness of the bedding layers on the fracture height is investigated and quantitively analyzed. Parametric studies are performed on the bedding layers properties, in-situ stress difference, and landing depth. Following conclusions are summarized from our numerical studies.

- The weak bedding layers in shale formations may slow down the vertical growth of the hydraulic fracture. Lateral shear slippage of the bedding layers affects the width of the hydraulic fractures around the intersection with the interfaces and reduces the effective stress intensity factors around the hydraulic fracture tips. More energy and larger net pressure are required to break the rock in the presence of weak bedding layers.
- The density and the shear fracture toughness of the bedding plane are two major factors that affect the fracture height growth. Denser bedding layers and larger shear fracture toughness result in shorter hydraulic fracture height with the same given net pressure and require higher net pressure to reach the same hydraulic fracture height. Larger shear fracture toughness results in larger maximum distance of shear slippage of the bedding layers and therefore causes larger energy loss.
- The effectiveness of the bedding layers is more obvious and significant in formations with low in-situ stress contrast than that of high in-situ stress contrast. This finding is consistent with the previous experimental results and the field observations. In formations with high in-situ stress contrast, the primary resistance on the vertical growth of the hydraulic fracture is the stress difference between layers, while in formations with low in-situ stress contrast, the primary resistance may come from the bedding layers shear slippage.

- The well landing depth has a significant impact on the hydraulic fracture height and the fracture tips growing profile. The net pressure required to penetrate the whole zone is smaller if the well is landed in a large-stress layer and vice versa. The fracture height growing upward and downward is most likely asymmetric, and the simulation helps us locate the appropriate landing depth that the given net pressure penetrates the target interval simultaneously at upper and lower bounds.

6.1.4. Hydraulic Fracture Propagation Considering the Effect of Weak Bedding Planes

In this part, we incorporate Chapter 2, Chapter 3, and Chapter 4 together and the impact of the horizontal weak interfaces in the laminated shale formations on the hydraulic fracture propagation and the final geometries is investigated. To capture the mechanism of the weak interfaces, a comprehensive and non-intrusive hydraulic fracture height growth model is developed and incorporated into a S3D DDM based hydraulic fracture propagation model. Several numerical cases based on the Permian Basin Wolfcamp Shale Formation are simulated including both single fracture scenario and multiple fractures scenario. Several conclusions are found through numerical studies:

- For a single hydraulic fracture in the laminated shale formations (or multiple fractures with large enough spacing that each individual fracture is identical), the impact of the horizontal weak interfaces tends to result in a reduction of the average hydraulic fracture height (the maximum height can also be reduced), an increase of the hydraulic fracture half length, and an overall decrease of the width values.

- The spacing (or the density) between the horizontal weak interfaces is one of the major factors that influences the effectiveness of the weak interfaces. The decrease of the spacing (increase of the density) between the weak interfaces tends to increase the impact on the hydraulic fracture geometries.
- The shear fracture toughness of the horizontal weak interfaces is another one of the major factors that matters. Under the equilibrium status, larger shear fracture toughness results in a larger shear slippage length in the horizontal interface, consequently a greater reduction of the effective stress intensity factor of the vertical hydraulic fracture. As a result, the average fracture height is reduced and the half length is increased.
- For multiple fracture propagation, the impact of the horizontal weak interfaces on the outer hydraulic fractures is similar regardless of the cluster spacing. The existence of the weak interface results in a reduction of the average fracture height while an increase of the fracture half length. Additionally, the fracture width values are reduced. The trends are similar as the single fracture scenario.
- For multiple fracture propagation, the impact of the horizontal weak interfaces on the inner fractures varies by cluster spacing. In closer spacing case, due to the reduction of the average heights of the outer hydraulic fractures, the stress shadow effects acting on the inner fractures is decreased. Therefore, the inner fractures experience increases not only in the average fracture height and half length, but

also in the overall width values. In larger spacing case, although the stress shadow effects are reduced from the decreased outer fracture heights, the average heights of the inner fractures are decreased. Meanwhile, the overall fracture width of the innermost fracture is decreased.

6.2. Recommendations for Future work

Fracture height containment/growth continues to be a central issue in modeling and evaluation of hydraulic fracturing treatments. Based on the results of this dissertation and the conclusions from the studies, several topics in this work could be extended. These topics include (1) development of three-dimensional joint element based higher order displacement discontinuity method for arbitrary fracture geometries, (2) extending the static shear slippage model by considering the offset, (3) considering natural fractures or the horizontal interfaces with an inclination.

- The joint element based higher order displacement discontinuity method developed in this work is only for 2D planar fractures. For non-planar fractures, the three-element patch can be curved, and the interpolation method would be slightly different. Accurate interpolation on the curved three-element patch might be sophisticated, yet by subdividing the elements and doing some extrapolations on the straight part might be able to solve this type of problem. Another improvement to be made is to expand the 2D equations to the three-dimensional ones. The rock deformation equations for the higher order 3D DDM are same as the ones for 2D. The higher order formulation based on patched elements follows similar rule as we have discussed in Chapter 2. The joint element types are the same and the criterion for the different contact types of the joint are also based on the linear elastic fracture mechanics.

- One limitation of our height model is that the offset of the hydraulic fracture upon approaching the horizontal weak interface cannot be solved in our process. Although the offset can be treated as similar as a reduction of the fracture height, it has a considerable impact on the hydraulic fracture geometry. A mechanical model is required to describe the re-initiation of an arrested hydraulic fracture by the horizontal interface to better understand the offset phenomenon.
- The natural fractures can be another group of factors that influence the hydraulic fracture geometries. For horizontal natural fracture, it can be modeled the same as the horizontal weak interfaces. For natural fractures that have dip angles or weak interfaces that have inclinations, our model should be modified based on the boundary conditions. The inclined fractures or interfaces also follow the linear elastic fracture mechanics. But the in-situ normal stress and shear stress acting on the interfaces are different, which might be a significant factor governing the shear slippage procedure and the ultimate shear sliding length.
- The model can also be extended to non-homogeneous rock formations since the boundary element model can be used for heterogeneous rock if each region has constant elastic moduli. Another modification required for non-homogeneous rock is the equilibrium height equation, which is originally developed based on the homogeneous rock.

REFERENCES

Abbas, S., Gordeliy, E., Peirce, A., Lecampion, B., Chuprakov, D. and Prioul, R., 2014, February. Limited height growth and reduced opening of hydraulic fractures due to fracture offsets: an XFEM application. In SPE hydraulic fracturing technology conference. OnePetro.

Adachi, J., Siebrits, E.M., Peirce, A. and Desroches, J., 2007. Computer simulation of hydraulic fractures. International Journal of Rock Mechanics and Mining Sciences, 44(5), pp.739-757.

Ahmed, U., 1984, May. A practical hydraulic fracturing model simulating necessary fracture geometry, fluid flow and leakoff, and proppant transport. In SPE Unconventional Gas Recovery Symposium. OnePetro.

Anderson, G. D., 1981, Effects of friction on hydraulic fracture growth near unbonded interfaces in rocks: SPE Journal, 21, 21–29, doi: 10.2118/8347-PA.

Anusarn, S., Li, J., Wu, K., Wang, Y., Shi, X., Yin, C. and Li, Y., 2019, August. Fracture Hits Analysis for Parent-Child Well Development. In 53rd US Rock Mechanics/Geomechanics Symposium. American Rock Mechanics Association.

Behnia, M., Goshtasbi, K., Marji, M.F. and Golshani, A., 2015. Numerical simulation of interaction between hydraulic and natural fractures in discontinuous media. Acta Geotechnica, 10(4), pp.533-546.

Bieniawski, Z.T., 1967, October. Mechanism of brittle fracture of rock: part I—theory of the fracture process. In International Journal of Rock Mechanics and Mining Sciences & Geomechanics Abstracts (Vol. 4, No. 4, pp. 395-406). Pergamon.

Burghardt, J., J. Desroches, B. Lecampion, S. Stanchits, A. Surdi, N. Whitney, and M. Houston, 2015, Laboratory study of the effect of well orientation, completion design, and rock fabric on near-wellbore hydraulic fracture geometry in shales: 13th ISRM International Congress of Rock Mechanics, ISRM-13 CONGRESS-2015-357.

Bunger, A., Kear, J., Jeffrey, R. et al. 2016. Laboratory investigation of hydraulic fracture growth through weak discontinuities with active ultrasound monitoring. CIM Journal, 7 (3). https://doi.org/10.15834/cimj.2016.17

Carter, R.D. 1957. Appendix to Optimum Fluid Characteristics for Fracture Extension. In Drill. and Prod. Prac., ed. G.C. Howard and C.R.Fast. API 267.

Chuprakov, D., Melchaeva, O. and Prioul, R., 2014. Injection-sensitive mechanics of hydraulic fracture interaction with discontinuities. Rock mechanics and rock engineering, 47(5), pp.1625-1640.

Chuprakov, D. and Prioul, R., 2015, February. Hydraulic fracture height containment by weak horizontal interfaces. In SPE hydraulic fracturing technology conference. OnePetro.

Cleary, M.P., 1978. Primary factors governing hydraulic fractures in heterogeneous stratified porous formations (No. UCRL-13884; CONF-781112-10). Massachusetts Inst. of Tech., Cambridge (USA).

Cooke, M.L. and Underwood, C.A., 2001. Fracture termination and step-over at bedding interfaces due to frictional slip and interface opening. Journal of structural geology, 23(2-3), pp.223-238.

Crawford, A.M. and Curran, J.H., 1982, June. Higher-order functional variation displacement discontinuity elements. In International Journal of Rock Mechanics and Mining Sciences & Geomechanics Abstracts (Vol. 19, No. 3, pp. 143-148). Pergamon.

Crouch, S.L., 1976. Solution of plane elasticity problems by the displacement discontinuity method. I. Infinite body solution. International Journal for Numerical Methods in Engineering, 10(2), pp.301-343.

Crouch, S.L., Starfield, A.M. and Rizzo, F.J., 1983. Boundary element methods in solid mechanics.

Daneshy, A.A., 1978. Hydraulic fracture propagation in layered formations. Society of Petroleum Engineers Journal, 18(01), pp.33-41.

Daneshy, A., Blümling, P., Marschall, P. and Zuidema, P., 2004, February. Interpretation of field experiments and observation of fracturing process. In SPE International Symposium and Exhibition on Formation Damage Control. OnePetro.

Daneshy, A.A. 2009. Factors controlling the vertical growth of hydraulic fractures. Presented at the SPE Hydraulic Fracturing Technology Conference held in The Woodlands, Texas, USA, 19-21 January. SPE-118789-MS. https://doi.org/10.2118/118789-MS.

Detournay, E. and Cheng, A.H.D., 1991. Plane strain analysis of a stationary hydraulic fracture in a poroelastic medium. International Journal of Solids and Structures, 27(13), pp.1645-1662.

Detournay, E., 2016. Mechanics of hydraulic fractures. Annual review of fluid mechanics, 48, pp.311-339.

Diaz, H.G., Desroches, J., Williams, R., Defeu, C., Martin, J. and Cannon, D., 2018, October. Rock fabric analysis based on borehole image logs: Applications to modeling fracture height growth. In SPE International Hydraulic Fracturing Technology Conference and Exhibition. OnePetro.

Dong, C.Y. and De Pater, C.J., 2001. Numerical implementation of displacement discontinuity method and its application in hydraulic fracturing. Computer methods in applied mechanics and engineering, 191(8-10), pp.745-760.

Elbel, J.L., Piggott, A.R., and Mack, M.G. 1992. Numerical Modeling of Multilayer Fracture Treatments. Presented at the SPE Permian Basin Oil and Gas Recovery Conference, Midland, Texas, 18–20 March. SPE-23982-MS. http://dx.doi.org/10.2118/23982-MS.

Evans, S., Halliburton, F., Siddiqui, S. and Magness, J., 2018. Impact of Cluster Spacing on Infill Completions in the Eagle Ford. In Unconventional Resources Technology Conference, Houston, Texas, 23-25 July 2018 (pp. 2777-2789). Society of Exploration Geophysicists, American Association of Petroleum Geologists, Society of Petroleum Engineers.

Fisher, K. and Warpinski, N., 2012. Hydraulic-fracture-height growth: Real data. SPE Production & Operations, 27(01), pp.8-19.

Fu, W., Morris, J., Fu, P et al. 2021. Developing upscaling approach for swarming hydraulic fractures observed at hydraulic fracturing test site through multiscale simulations. SPE Journal. SPE-199689-PA.

Fung, R.L., Vilayakumar, S. and Cormack, D.E., 1987. Calculation of vertical fracture containment in layered formations. SPE formation evaluation, 2(04), pp.518-522.

Gale, J.F. and Holder, J., 2008, June. Natural fractures in the Barnett Shale: Constraints on spatial organization and tensile strength with implications for hydraulic fracture treatment in shale-gas reservoirs. In The 42nd US Rock Mechanics Symposium (USRMS). OnePetro.

Gale, J.F., Reed, R.M. and Holder, J., 2007. Natural fractures in the Barnett Shale and their importance for hydraulic fracture treatments. AAPG bulletin, 91(4), pp.603-622.

Gamero Diaz, H., Desroches, J., Williams, R. et al. 2018. Rock fabric analysis based on borehole image logs: Applications to modeling fracture height growth. Presented at the SPE International Hydraulic Fracturing Technology Conference and Exhibition, Muscat, Oman, 16–18 October. https://doi.org/10.2118/191389-18IHFT-MS.

Ghassemi, A., 1997. Three-dimensional poroelastic hydraulic fracture simulation using the displacement discontinuity method.

Ghassemi, A. and Zhang, Q., 2006. Porothermoelastic analysis of the response of a stationary crack using the displacement discontinuity method. Journal of engineering mechanics, 132(1), pp.26-33.

Gu, H., 1987. A study of propagation of hydraulically induced fractures (Doctoral dissertation, The University of Texas at Austin).

Gu, H., Siebrits, E. and Sabourov, A., 2008, October. Hydraulic fracture modeling with bedding plane interfacial slip. In SPE Eastern Regional/AAPG Eastern Section Joint Meeting. OnePetro.

Gu, H. and Weng, X., 2010, June. Criterion for fractures crossing frictional interfaces at non-orthogonal angles. In 44th US rock mechanics symposium and 5th US-Canada rock mechanics symposium. OnePetro.

Hoek, E. and Bieniawski, Z.T., 1965. Brittle fracture propagation in rock under compression. International Journal of Fracture Mechanics, 1(3), pp.137-155.

Hu, L. and Ghassemi, A., 2021. Laboratory-Scale Investigation of the Slippage of a Natural Fracture Resulting from an Approaching Hydraulic Fracture. Rock Mechanics and Rock Engineering, 54(5), pp.2547-2558.

Hu, X., Wu, K., Li, G., Tang, J. and Shen, Z., 2018. Effect of proppant addition schedule on the proppant distribution in a straight fracture for slickwater treatment. Journal of Petroleum Science and Engineering, 167, pp.110-119.

Jeffrey, R.G., Vandamme, L. and Roegiers, J.C., 1987, May. Mechanical interactions in branched or subparallel hydraulic fractures. In SPE/DOE Joint Symposium on Low Permeability Reservoirs. OnePetro.

Jeffrey, R.G., Zhang, X. and Bunger, A.P., 2010, February. Hydraulic fracturing of naturally fractured reservoirs. In Thirty-Fifth Workshop on Geothermal Reservoir Engineering, Stanford University, Stanford, California (pp. 1-3).

Kachanov, M.L., Shafiro, B. and Tsukrov, I., 2003. Handbook of elasticity solutions. Springer Science & Business Media.

Khanna, A. and Kotousov, A., 2016. Controlling the height of multiple hydraulic fractures in layered media. SPE Journal, 21(01), pp.256-263.

Kear, J., Kasperczyk, D., Zhang, X. et al. 2017. 2D experimental and numerical results for hydraulic fractures interacting with orthogonal and inclined discontinuities. Presented at the 51st US Rock Mechanics Geomechanics Symposium, San Francisco, California, USA, 25–28 June. ARMA-2017-0404.

Kresse, O. and Weng, X., 2018. Numerical modeling of 3D hydraulic fractures interaction in complex naturally fractured formations. Rock Mechanics and Rock Engineering, 51(12), pp.3863-3881.

Kresse, O. and Weng, X., 2019, June. Effect of shear slippage of vertically crossed layer interface on hydraulic fracture height growth. In 53rd US Rock Mechanics/Geomechanics Symposium. OnePetro.

Lecampion, B., Bunger, A. and Zhang, X., 2018. Numerical methods for hydraulic fracture propagation: a review of recent trends. Journal of natural gas science and engineering, 49, pp.66-83.

Li, J., Li, Y. and Wu, K., 2021, June. An Efficient Higher Order Displacement Discontinuity Method with Joint Element for Hydraulic Fracture Modeling. In 55th US Rock Mechanics/Geomechanics Symposium. OnePetro.

Li, J., Liu, Y. and Wu, K., 2022. A New Higher Order Displacement Discontinuity Method Based on the Joint Element for Analysis of Close-Spacing Planar Fractures. SPE Journal, 27(02), pp.1123-1139.

Li, J. and Wu, K., 2022a. An Efficient Model for Hydraulic Fracture Height Growth Considering the Effect of Bedding Layers in Unconventional Shale Formations. SPE Journal, pp.1-17.

Li, J. and Wu, K., 2022b, June. Impact of horizontal weak interfaces on the hydraulic fracturing: from height growth to lateral propagation. In SPE/AAPG/SEG Unconventional Resources Technology Conference. OnePetro.

Li, Y., Long, M., Tang, J., et al., 2020. A hydraulic fracture height mathematical model considering the influence of plastic region at fracture tip. Petrol. Explor. Dev. 47 (1), 184–195.

Liu, S. and Valkó, P.P., 2018. A rigorous hydraulic-fracture equilibrium-height model for multilayer formations. SPE Production & Operations, 33(02), pp.214-234.

Liu, Y., Jin, G., Wu, K. and Moridis, G., 2021. Hydraulic-Fracture-Width Inversion Using Low-Frequency Distributed-Acoustic-Sensing Strain Data—Part I: Algorithm and Sensitivity Analysis. SPE Journal, 26(01), pp.359-371.

Liu, Y., Wu, K., Jin, G., Moridis, G., Kerr, E., Scofield, R. and Johnson, A., 2020. Fracture-Hit Detection Using LF-DAS Signals Measured during Multifracture Propagation in Unconventional Reservoirs. SPE Reservoir Evaluation & Engineering.

Llanos, E.M., Jeffrey, R.G., Hillis, R. and Zhang, X., 2017. Hydraulic fracture propagation through an orthogonal discontinuity: a laboratory, analytical and numerical study. Rock Mechanics and Rock Engineering, 50(8), pp.2101-2118.

Mack, M. G. and Warpinski, N. R. 2000. Mechanics of Hydraulic Fracturing. In Reservoir Stimulation, third edition, ed. M. J. Economides and K. G. Nolte, Chap. 6. West Sussex, UK: John Wiley & Sons.

Maxwell, S., 2014. Microseismic imaging of hydraulic fracturing: Improved engineering of unconventional shale reservoirs. Society of Exploration Geophysicists.

McClure, M.W., 2012. Modeling and characterization of hydraulic stimulation and induced seismicity in geothermal and shale gas reservoirs. Stanford, California: Stanford University.

Mehrabi, M., Pei, Y., Haddad, M., Javadpour, F. and Sepehrnoori, K., 2021, July. Quasi-Static Fracture Height Growth in Laminated Reservoirs: Impacts of Stress and Toughness Barriers, Horizontal Well Landing Depth, and Fracturing Fluid Density. In SPE/AAPG/SEG Unconventional Resources Technology Conference. OnePetro.

Olson, J.E. 2004. Predicting Fracture Swarms-The Influence of Subcritical Crack Growth and the Crack-Tip Process Zone on Joint Spacing in Rock. In The Initiation, Propagation, and Arrest of Joints and Other Fractures, ed. J.W. Cosgrove and T. Engelder, 73–87. Geological Society of London Special Publication 231.

Olson, J.E., 2008, January. Multi-fracture propagation modeling: Applications to hydraulic fracturing in shales and tight gas sands. In The 42nd US rock mechanics symposium (USRMS). American Rock Mechanics Association.

Peterson, R.E., Wolhart, S.L., Frohne, K.H., Branagan, P.T., Warpinski, N.R. and Wright, T.B., 1996, October. Fracture diagnostics research at the GRI/DOE Multi-Site project: overview of the concept and results. In SPE Annual Technical Conference and Exhibition. OnePetro.

Pine, R.J. and Batchelor, A.S., 1984. Downward migration of shearing in jointed rock during hydraulic injections. In International Journal of Rock Mechanics and Mining Sciences & Geomechanics Abstracts (Vol. 21, No. 5, pp. 249-263). Pergamon.

Prioul, R., Nolen-Hoeksema, R., Loan, M., Herron, M., Akkurt, R., Frydman, M., Reynolds, L., Sanchez, M., Graf, G., Karg, H. and Caniggia, J., 2018. Using cuttings to extract geomechanical properties along lateral wells in unconventional reservoirs. Geophysics, 83(3), pp.MR167-MR185.

Rafiee, M., Soliman, M.Y., Pirayesh, E. and Emami Meybodi, H., 2012, Geomechanical considerations in hydraulic fracturing designs. In SPE Canadian Unconventional Resources Conference.

Raterman, K.T., Farrell, H.E., Mora, O.S., et al. 2018. Sampling a Stimulated Rock Volume: An Eagle Ford Example. SPE Reservoir Evaluation & Engineering. 21(04): 927-941.Rho, S., Noynaert, S., Bunger, A.P. et al. 2017. Finite-element simulations of hydraulic fracture height growth on layered mudstones with weak interfaces. Presented at the 51st US Rock Mechanics/Geomechanics Symposium, San Francisco, California, USA, 25–28 June. ARMA-2017-0727.

Rice, J.R., 1968. Mathematical analysis in the mechanics of fracture. Fracture: an advanced treatise, 2, pp.191-311.

Rutledge, J., Weng, X., Yu, X. et al. 2016. Bedding-plane slip as a microseismic source during hydraulic fracturing. SEG Technical Program Expanded Abstracts 2016. https://doi.org/10.1190/segam2016-13966680.1

Rutledge*, J., Yu, X., Leaney, S., Bennett, L. and Maxwell, S., 2014. Microseismic shearing generated by fringe cracks and bedding-plane slip. In SEG Technical Program Expanded Abstracts 2014 (pp. 2267-2272). Society of Exploration Geophysicists.

Schlichting, H. 1968. Boundary-Layer Theory, sixth edition. New York: McGraw-Hill

Sesetty, V. and Ghassemi, A., 2013, May. Numerical simulation of sequential and simultaneous hydraulic fracturing. In ISRM International Conference for Effective and Sustainable Hydraulic Fracturing. OnePetro.

Sheibani, F., 2013. Solving three-dimensional problems in natural and hydraulic fracture development: insight from displacement discontinuity modeling. Dissertation.

Shrivastava, K. and Sharma, M.M., 2018a. Mechanisms for the formation of complex fracture networks in naturally fractured rocks. In SPE Hydraulic Fracturing Technology Conference and Exhibition. Society of Petroleum Engineers.

Shou, K.J., 1993. A higher order three-dimensional displacement discontinuity method with application to bonded half-space problems. Doctoral dissertation, University of Minnesota.

Shou, K.J. and Crouch, S.L., 1995, January. A higher order displacement discontinuity method for analysis of crack problems. In International journal of rock mechanics and mining sciences & geomechanics abstracts (Vol. 32, No. 1, pp. 49-55). Pergamon.

Shou, S.K.J., Siebrits, E. and Crouch, S.L., 1997, February. A higher order displacement discontinuity method for three-dimensional elastostatic problems. In International journal of rock mechanics and mining sciences & geomechanics abstracts (Vol. 34, No. 2, pp. 317-322). Elsevier BV.

Sierra, J., Kaura, J., Gualtieri, D., Glasbergen, G., Sarkar, D. and Johnson, D., 2008. DTS Monitoring Data of Hydraulic Fracturing: Experiences and Lessons Learned. Paper SPE 116182 presented at the SPE Annual Technical Conference and Exhibition, Denver, 21–24 September.

Simonson, E.R., Abou-Sayed, A.S. and Clifton, R.J., 1978. Containment of massive hydraulic fractures. Society of Petroleum Engineers Journal, 18(01), pp.27-32.

Siriwardane, H.J. and Layne, A.W. 1991. Improved Model for Predicting Multiple Hydraulic Fracture Propagation From a Horizontal Well. Presented at the SPE Eastern Regional Meeting, Lexington, Kentucky, 22–25 October. SPE-23448-MS. http://dx.doi.org/10.2118/23448-MS.

Smye, K.M., Ikonnikova, S., Yang, Q., McDaid, G. and Goodman, E., 2020. Geologic Variability and Well Productivity in US Oil Plays: The Efficiency of Completion Intensity and New Designs in Various Geologic Contexts. In Unconventional Resources Technology Conference, 20–22 July 2020 (pp. 1709-1718). Unconventional Resources Technology Conference (URTeC).

Srinivasan, K., Ajisafe, F., Alimahomed, F., Panjaitan, M., Makarychev-Mikhailov, S. and Mackay, B., 2018, September. Is there anything called too much proppant?. In SPE Liquids-Rich Basins Conference-North America. OnePetro.

Suarez-Rivera, R., Von Gonten, W. D., Graham, J. et al. 2016. Optimizing lateral landing depth for improved well production. Presented at the Unconventional Resources Technology Conference, San Antonio, Texas, USA, 1-3 August. https://doi.org/10.15530/URTEC-2016-2460515

Tan, Y., Wang, J., Rijken, P., Zhang, Z., Fang, Z., Wu, R., Ning, I.L.C. and Liu, X., 2021, December. Mechanism of Microseismic Generation During Hydraulic Fracturing–With Evidence From HFTS 2 Observations. In Unconventional Resources Technology Conference, 26–28 July 2021 (pp. 1146-1161). Unconventional Resources Technology Conference (URTeC).

Tang, J. and Wu, K., 2018a. A 3-D model for simulation of weak interface slippage for fracture height containment in shale reservoirs. International Journal of Solids and Structures, 144, pp.248-264.

Tang, J., Wu, K., Li, Y., Hu, X., Liu, Q. and Ehlig-Economides, C., 2018b. Numerical investigation of the interactions between hydraulic fracture and bedding planes with non-orthogonal approach angle. Engineering Fracture Mechanics, 200, pp.1-16.

Teufel, L.W. and Clark, J.A., 1984. Hydraulic fracture propagation in layered rock: experimental studies of fracture containment. Society of Petroleum Engineers Journal, 24(01), pp.19-32.

Thiercelin, M. and Makkhyu, E., 2007, May. Stress field in the vicinity of a natural fault activated by the propagation of an induced hydraulic fracture. In 1st Canada-US Rock Mechanics Symposium. OnePetro.

Valko, P. and Economides, M.J., 1993, October. Fracture Height Containment with Continuum Damage Mechanics. In SPE Annual Technical Conference and Exhibition. OnePetro.

Vandamme, L., Jeffrey, R.G. and Curran, J.H., 1988. Pressure distribution in three-dimensional hydraulic fractures. SPE production engineering, 3(02), pp.181-186.

Warpinski, N.R., 1985. Measurement of width and pressure in a propagating hydraulic fracture. Society of Petroleum Engineers Journal, 25(01), pp.46-54.

Warpinski, N.R., 2013, May. Understanding hydraulic fracture growth, effectiveness, and safety through microseismic monitoring. In ISRM International Conference for Effective and Sustainable Hydraulic Fracturing. OnePetro.

Warpinski, N.R., Clark, J.A., Schmidt, R.A. and Huddle, C.W., 1982. Laboratory investigation on the-effect of in-situ stresses on hydraulic fracture containment. Society of Petroleum Engineers Journal, 22(03), pp.333-340.

Warpinski, N.R., Northrop, D.A., Schmidt, R.A., Vollendorf, W.C. and Finley, S.J., 1981. Formation interface fracturing experiment: an in situ investigation of hydraulic fracture behavior near a material property interface. Final report (No. SAND-81-0938).

Warpinski, N.R. and Teufel, L.W., 1987. Influence of geologic discontinuities on hydraulic fracture propagation (includes associated papers 17011 and 17074). Journal of Petroleum Technology, 39(02), pp.209-220.

Weijermars, R., 2020. Optimization of Fracture Spacing and Well Spacing in Utica Shale Play Using Fast Analytical Flow-Cell Model (FCM) Calibrated with Numerical Reservoir Simulator. Energies, 13(24), p.6736.

Weng, X., 2015. Modeling of complex hydraulic fractures in naturally fractured formation. Journal of Unconventional Oil and Gas Resources, 9, pp.114-135.

Weng, X., Chuprakov, D., Kresse, O., Prioul, R. and Wang, H., 2018. Hydraulic fracture-height containment by permeable weak bedding interfaces. Geophysics, 83(3), pp.MR137-MR152.

Weng, X., Kresse, O., Cohen, C., Wu, R. and Gu, H., 2011. Modeling of hydraulic-fracture-network propagation in a naturally fractured formation. SPE Production & Operations, 26(04), pp.368-380.

Wu, K. and Olson, J.E., 2013, February. Investigation of critical in situ and injection factors in multi-frac treatments: guidelines for controlling fracture complexity. In SPE hydraulic fracturing technology conference. Society of Petroleum Engineers.

Wu, K. 2014. Numerical Modeling of Complex Hydraulic Fracture Development in Unconventional Reservoirs. Doctoral dissertation, University of Texas at Austin.

Wu, K. and Olson, J.E., 2015. Simultaneous multifracture treatments: fully coupled fluid flow and fracture mechanics for horizontal wells. SPE journal, 20(02), pp.337-346.

Wu, K. and Olson, J.E., 2016. Mechanisms of simultaneous hydraulic-fracture propagation from multiple perforation clusters in horizontal wells. SPE Journal, 21(03), pp.1-000.

Wu, K., Wu, B. and Yu, W., 2018. Mechanism analysis of well interference in unconventional reservoirs: insights from fracture-geometry simulation between two horizontal wells. SPE Production & Operations, 33(01), pp.12-20.

Wu, R., Kresse, O., Weng, X., Cohen, C.E. and Gu, H., 2012, February. Modeling of interaction of hydraulic fractures in complex fracture networks. In SPE Hydraulic Fracturing Technology Conference. OnePetro.

Wu, Y.S., 2018. Hydraulic fracture modeling. Gulf Professional Publishing.

Xing, P., Bunger, A.P., Yoshioka, K., Adachi, J. and El-Fayoumi, A., 2016, June. Experimental study of hydraulic fracture containment in layered reservoirs. In 50th US Rock Mechanics/Geomechanics Symposium. OnePetro.

Xiong, H., Liu, S., Feng, F., Liu, S. and Yue, K., 2019. Optimize Completion Design and Well Spacing with the Latest Complex Fracture Modeling & Reservoir Simulation Technologies–A Permian Basin Case Study with Seven Wells. In SPE Hydraulic Fracturing Technology Conference and Exhibition. Society of Petroleum Engineers.

Xiong, H., Wu, W. and Gao, S., 2018. Optimizing Well Completion Design and Well Spacing with Integration of Advanced Multi-Stage Fracture Modeling & Reservoir Simulation-A Permian Basin Case Study. In SPE Hydraulic Fracturing Technology Conference and Exhibition. Society of Petroleum Engineers.

Xu, W., Prioul, R., Berard, T., Weng, X. and Kresse, O., 2019, January. Barriers to hydraulic fracture height growth: A new model for sliding interfaces. In SPE Hydraulic Fracturing Technology Conference and Exhibition. OnePetro.

Ye, Z., Ghassemi, A. and Riley, S., 2016, August. Fracture properties characterization of shale rocks. In Unconventional Resources Technology Conference, San Antonio, Texas, 1-3 August 2016 (pp. 1083-1095). Society of Exploration Geophysicists, American Association of Petroleum Geologists, Society of Petroleum Engineers.

Yue, K., Olson, J.E. and Schultz, R.A., 2019. The effect of layered modulus on hydraulic-fracture modeling and fracture-height containment. SPE Drilling & Completion, 34(04), pp.356-371.

Zeng, Q. and Yao, J., 2016. Numerical simulation of fracture network generation in naturally fractured reservoirs. Journal of Natural Gas Science and Engineering, 30, pp.430-443.

Zeroug, S., Sinha, B.K., Lei, T. et al. 2018. Rock heterogeneity at the centimetric scale, proxies for interfacial weakness and rock strength-stress interplay from downhole ultrasonic measurements. Geophysics, 83: D83–D95. https://doi.org/10.1190/geo2017-0049.1.

Zheng, S., Manchanda, R. and Sharma, M.M., 2019. Development of a fully implicit 3-D geomechanical fracture simulator. Journal of Petroleum Science and Engineering, 179, pp.758-775.

Zhang, X. and Jeffrey, R.G., 2006. The role of friction and secondary flaws on deflection and re-initiation of hydraulic fractures at orthogonal pre-existing fractures. Geophysical Journal International, 166(3), pp.1454-1465.

Zhang, X., Jeffrey, R.G. and Thiercelin, M., 2007. Deflection and propagation of fluid-driven fractures at frictional bedding interfaces: a numerical investigation. Journal of Structural Geology, 29(3), pp.396-410.

Zhang, X. and Jeffrey, R.G., 2008. Reinitiation or termination of fluid‐driven fractures at frictional bedding interfaces. Journal of Geophysical Research: Solid Earth, 113(B8).

Zhang, Z., Fang, Z., Stefani, J. et al. 2020. Modeling of Fiber Optic Strain Responses to Hydraulic Fracturing. Geophysics 85(6): 1-22. https://doi.org/10.1190/geo2020-0083.1

Zou, Y., Zhang, S., Ma, X., Zhou, T. and Zeng, B., 2016. Numerical investigation of hydraulic fracture network propagation in naturally fractured shale formations. Journal of Structural Geology, 84, pp.1-13.

APPENDIX A

DERIVATIVES OF INTEGRAL KERNELS

The derivatives of the integral kernels Int^0, Int^1, Int^2 are given by:

$$\begin{aligned}
Int^0{}_{,x} &= -\ln(\frac{r_1}{r_2}) \\
Int^0{}_{,y} &= \theta_1 - \theta_2 \\
Int^0{}_{,xy} &= -(\frac{y}{r_1^{\ 2}} - \frac{y}{r_2^{\ 2}}) \\
Int^0{}_{,xx} &= -(\frac{(x-a)}{r_1^{\ 2}} - \frac{(x+a)}{r_2^{\ 2}}) \\
Int^0{}_{,xyy} &= -(\frac{((x-a)^2 - y^2)}{r_1^{\ 4}} - \frac{((x+a)^2 - y^2)}{r_2^{\ 4}}) \\
Int^0{}_{,yyy} &= -(\frac{2(x-a)y}{r_1^{\ 4}} - \frac{2(x+a)y}{r_2^{\ 4}})
\end{aligned} \tag{A.1}$$

$$\begin{aligned}
Int^1{}_{,x} &= y(\theta_1 - \theta_2) - x\ln(\frac{r_1}{r_2}) - 2a \\
Int^1{}_{,y} &= x(\theta_1 - \theta_2) + y\ln(\frac{r_1}{r_2}) \\
Int^1{}_{,xy} &= (\theta_1 - \theta_2) - ay(\frac{1}{r_1^{\ 2}} - \frac{1}{r_2^{\ 2}}) \\
Int^1{}_{,xx} &= -(\ln(\frac{r_1}{r_2}) + \frac{a(x-a)}{r_1^{\ 2}} + \frac{a(x+a)}{r_2^{\ 2}}) \\
Int^1{}_{,xyy} &= \frac{x}{r_1^{\ 2}} - \frac{x}{r_2^{\ 2}} - \frac{2a(x-a)^2}{r_1^{\ 4}} - \frac{2a(x+a)^2}{r_2^{\ 4}} \\
Int^1{}_{,yyy} &= \frac{y}{r_1^{\ 2}} - \frac{y}{r_2^{\ 2}} - \frac{2a(x-a)y}{r_1^{\ 4}} - \frac{2a(x+a)y}{r_2^{\ 4}}
\end{aligned} \tag{A.2}$$

$$
\begin{aligned}
Int^2{}_{,x} &= 2xy(\theta_1-\theta_2)+(y^2-x^2)\ln(\frac{r_1}{r_2})-2ax \\
Int^2{}_{,y} &= (x^2-y^2)(\theta_1-\theta_2)+2xy\ln(\frac{r_1}{r_2})+2ay \\
Int^2{}_{,xy} &= 2x(\theta_1-\theta_2)+2y\ln(\frac{r_1}{r_2})-a^2y\frac{1}{r_1{}^2}+a^2y\frac{1}{r_2{}^2} \\
Int^2{}_{,xx} &= 2y(\theta_1-\theta_2)-2x\ln(\frac{r_1}{r_2})-a^2(x-a)\frac{1}{r_1{}^2}+a^2(x+a)\frac{1}{r_2{}^2}-4a \\
Int^2{}_{,xyy} &= 2\ln(\frac{r_1}{r_2})+a(2x-a)\frac{1}{r_1{}^2}+a(2x+a)\frac{1}{r_2{}^2}-\frac{2a^2(x-a)^2}{r_1{}^4}+\frac{2a^2(x+a)^2}{r_2{}^4} \\
Int^2{}_{,yyy} &= -2(\theta_1-\theta_2)+2ay\frac{1}{r_1{}^2}+2ay\frac{1}{r_2{}^2}-\frac{2a^2(x-a)y}{r_1{}^4}+\frac{2a^2(x+a)y}{r_2{}^4}
\end{aligned}
\tag{A.3}
$$

where θ_1 and θ_2, r_1 and r_2 are given in Equation (2.11).

The derivatives of the integral kernels Int^c are given by:

$$
\begin{aligned}
Int^c{}_{,x} &= xA_1-A_2 \\
Int^c{}_{,y} &= yA_1 \\
Int^c{}_{,xy} &= -2yA_{22} \\
Int^c{}_{,xx} &= -A_1+2yA_{21} \\
Int^c{}_{,xyy} &= -2A_{22}+8y^2A_{32} \\
Int^c{}_{,yyy} &= -6A_{21}+8y^3A_{31}
\end{aligned}
\tag{A.4}
$$

where

$$
\begin{aligned}
A_1 &= \rho^{-1}[0.5(\cos(\varphi)-(\frac{x}{y})\sin(\varphi))\ln(\frac{(\xi-2\xi^{0.5}\rho\cos(\varphi)+\rho^2)}{(\xi+2\xi^{0.5}\rho\cos(\varphi)+\rho^2)}) \\
&+(\sin(\varphi)+(\frac{x}{y})\cos(\varphi))acr\tan(\frac{2\xi^{0.5}\rho\sin(\varphi)}{\rho^2-\xi})] \\
A_2 &= \rho[0.5(\cos(\varphi)+(\frac{x}{y})\sin(\varphi))\ln(\frac{(\xi-2\xi^{0.5}\rho\cos(\varphi)+\rho^2)}{(\xi+2\xi^{0.5}\rho\cos(\varphi)+\rho^2)}) \\
&+(-\sin(\varphi)+(\frac{x}{y})\cos(\varphi))acr\tan(\frac{2\xi^{0.5}\rho\sin(\varphi)}{\rho^2-\xi})]
\end{aligned}
\tag{A.5}
$$

with $\rho=(x^2+y^2)^{1/4}$ and $\varphi=0.5\arctan(\frac{y}{x})$, and

$$
\begin{aligned}
A_{21} &= \frac{0.5\rho^{3/2}(x\xi-x^2+y^2)}{y^2(x^2+y^2)((x-\xi)^2+y^2)}+\frac{0.25(-xA_2+(3x^2+y^2)A_1)}{y^2(x^2+y^2)} \\
A_{22} &= \frac{0.5\rho^{3/2}(2x-\xi)}{(x^2+y^2)((x-\xi)^2+y^2)}+\frac{0.25(A_2-2xA_1)}{(x^2+y^2)} \\
A_{31} &= \frac{0.25\rho^{3/2}(x\xi-x^2+y^2)}{y^2(x^2+y^2)((x-\xi)^2+y^2)^2}+\frac{0.125(-3xA_{22}+(6x^2+5y^2)A_{21})}{y^2(x^2+y^2)} \\
A_{32} &= \frac{0.25\rho^{3/2}(2x-\xi)}{y^2(x^2+y^2)((x-\xi)^2+y^2)^2}+\frac{0.125(3A_{22}-xA_{21})}{(x^2+y^2)}
\end{aligned}
\tag{A.6}
$$